Power Transmission Lines Transient Electromagnetic Fields—A Study of Scale Modeling and the Effects of Ground Loss

by

Pooya Taheri Gharagozloo

A Thesis submitted to the Faculty of Graduate Studies of
The University of Manitoba
in partial fulfillment of the requirements for the degree of

Master of Science

Department of Electrical and Computer Engineering
University of Manitoba

THE UNIVERSITY OF MANITOBA

FACULTY OF GRADUATE STUDIES

*****

COPYRIGHT PERMISSION

Power Transmission Lines Transient Electromagnetic Fields—A Study of Scale Modeling and the Effects of Ground Loss

By

Pooya Taheri Gharagozloo

A Thesis/Practicum submitted to the Faculty of Graduate Studies of The University of Manitoba in partial fulfillment of the requirement of the degree

Of

Master of Science

Acknowledgement

Accomplishment of this thesis is a milestone in my life; I owe my gratitude to those who have made this thesis viable.

First, I would like to thank my advisors, Dr. Behazd Kordi and Dr. Ani Golé, for providing me with an opportunity to work on this challenging project. I am especially thankful for their invaluable guidance and financial support throughout my program. This thesis could not have been presented in this form without their help.

I would like to direct my sincerest appreciation to the committee members, Dr. Greg Bridges and Dr. Fariborz Hashemian, who kindly accepted to be on my committee and took the time to go over my thesis.

I would also like to thank the Government of Manitoba for their partial financial support in the form of Manitoba Graduate Scholarship.

I must confess that during my Master's program, I learnt more about life and people than I did about science and engineering. I am greatly indebted to my dear friends, Alireza, Ehsan, Gelareh, Gol, Hamid, Maziar, Nadia, Reza, Sara, Sassan, and Sima, whom were the ones that brought me to this revelation. I am very privileged to have known them thus far and I wish to thank them for their friendship.

Most importantly, I would like to express my deepest thanks to my parents who have always stood by me. Though far away, but their support has always been with me. Words cannot convey the gratitude I owe them.

To My Beloved Parents

Abstract

In this thesis, the problem of calculating power transmission line induced or radiated electromagnetic fields is studied by decomposing the line into a large number of small segments, known as Hertzian dipoles. Since the presence of lossy ground makes the electromagnetic field distribution very different from that of the same dipole over perfectly conducting ground, different approaches should be followed for the lossy and lossless ground assumptions. The contribution of each dipole on the total electric and magnetic field is calculated using three analytical techniques. Two of these methods are frequency-domain solutions for the problem of dipole radiation above lossy ground, while the third method is a time-domain exact solution for the same problem based on the assumption of perfectly conducting ground. The theoretical background and extent of validity of each technique are reviewed in this thesis. The results derived by applying each method are compared with those obtained using a commercial software package.

The time-domain solution for the problem of power transmission line electromagnetic fields is obtained using Fourier and inverse Fourier transforms, which enables us to obtain the electromagnetic waveforms associated with power system transients. The effect of different parameters such as conductivity and relative permittivity of the ground, the line-to-observation point distance, height, and sag of the transmission line is studied. Further, the impact of downscaling of transmission line on different electromagnetic parameters is analyzed, and the appropriate scale factor for each parameter is derived.

Table of Contents

List of Figures

List of Tables

List of Abbreviations

ELF.....*Extremely-Low Frequency*

EM.....*Electromagnetics*

FDTD.....*Finite-Difference Time-Domain*

FFT.....*Fast Fourier Transform*

HED.....*Horizontal Electric Dipole*

HMD.....*Horizontal Magnetic Dipole*

IFFT.....*Inverse Fast Fourier Transform*

LTI.....*Linear Time-Invariant*

MFDTD.....*Modified Finite-Difference Time-Domain*

NEC.....*Numerical Electromagnetic Code*

PEC.....*Perfect Electric Conductor*

TE.....*Transverse Electric*

TM.....*Transverse Magnetic*

VED.....*Vertical Electric Dipole*

VMD.....*Vertical Magnetic Dipole*

Chapter 1

Introduction

1.1 Motivation

Due to their expansive physical dimensions, transmission line networks are the most critical components of a power system from an electromagnetic point of view. They act as huge transmitting antennas, radiating low- and high-frequency electromagnetic fields into the surrounding space. At the same time, they behave as receiving antennas, absorbing electromagnetic energy radiated by external sources, such as indirect lightning strikes, which is carried over long distances.

Radiated electromagnetic (EM) fields, which are of strong amplitudes, are produced during normal and transient operation of transmission lines. Transmission line radiation interference can cause major problems for electronic devices installed in the vicinity of transmission networks for measurement, protection, and control purposes. To ensure normal functioning of the electronic equipment present in this electromagnetic environment, the radiated transient electromagnetic fields must be accurately calculated.

Further, electromagnetic coupling is a strong source of interference. Mitigation of this interference requires an understanding of parameters which affect the coupling. Recently, there has been concern about possible health issues associated with exposure to the electric and magnetic fields in the vicinity of transmission lines. It is this issue which has brought considerable media attention to the power transmission line environment.

These issues underline the need for accurate evaluation of electromagnetic fields arising from exposure to power transmission lines. Since the measurement experiments have been proved to be quite expensive, electromagnetic radiation needs to be evaluated through numerical calculation.

1.2 Problem Definition

Radiation in the air above conductive homogeneous ground from a finite-length power transmission line has been considered by many researchers, initiated by Sommerfeld [1] and [2]. There is a massive body of literature describing the performance of wire conductors energized at low and high frequencies in the air and soil.

The goal of this thesis is to propose a generalized technique for calculating the radiated electromagnetic fields associated with a power transmission line, located above lossy ground. To achieve this goal, the huge amount of research on this topic is reviewed and some of the validated techniques introduced in the literature are implemented and merged together.

It is a well known fact that the presence of lossy ground makes the field radiated from a transmission line very different from that of the same line in an infinite homogeneous

region or above perfectly-conductive ground [3]. Therefore, in this research different approaches are considered towards the lossless and lossy ground assumptions.

According to the *Dipole Technique* [4]-[10], any radiating body may be regarded as being made up of a large number of short dipoles. Thus, the total radiated electromagnetic field is the sum of all the contributions from each constituent dipole. The dipole technique, also known as *Hertzian Dipole Technique* [5]-[7], requires only knowledge of the current density of the radiating body as a function of time and space.

In this work, for the case of perfectly-conductive ground, use is made of direct solution of Maxwell's equations. However, for the case of lossy ground, two main frequency-domain approaches towards this problem, *Complex Image Theory* [11]-[15] and King's formulation [16]-[19], are reviewed and implemented. Since the aforementioned techniques cannot provide an accurate value for the DC component of the electromagnetic fields, the equations derived by Olsen [20] and [21] are implemented to complete the formulation.

The validity of the results is verified using the numerical software package NEC [22], which is based on the *Method of Moments (MoM)*.

In the development of the mentioned methods, the calculation of the fields depends on the knowledge of the current along the transmission line. Therefore, to find the current distribution along the line, when excited by known current or voltage sources, the *Modified Finite Difference Time Domain (MFDTD)* technique [23] and [24] is used, which provides the required current information for each segment of the line.

Traditional electromagnetic field computation techniques assume that the current-carrying power transmission lines are straight horizontal wires. This assumption results in

a model whose electromagnetic fields are distorted from those produced in reality, especially when dealing with the transient fields. To overcome this deficiency, we take the sag of the line into account in the field calculation process by considering the exact shape of the catenary before decomposing the line into short dipoles [25] and [26].

One of the practical techniques in the study of power transmission networks is fabricating a scaled model of the system and performing compatibility and susceptibility tests under controlled conditions. The reduced-scale model should represent the full-scale equipment realistically for electric effect measurement purposes. Therefore, properly-chosen scale factors should be applied for physical and temporal parameters. The impact of geometrical scaling on electromagnetic parameters of a power transmission line is evaluated by making use of the similarity theory [27]-[29]. Accordingly, different scale factors for various transmission line parameters are calculated.

1.3 Thesis Outline

Chapter 2 of this thesis is devoted to calculation of the electromagnetic fields associated with a power transmission line located above Perfectly Electric Conducting (PEC) ground. In the first part of Chapter 2, the dipole technique is introduced. As it was briefly mentioned before, this technique is based on decomposing the line into many small segments and finding the total radiated electromagnetic field in the vicinity of the line as the summation of all the contributions from each dipole. The second part of Chapter 2 deals with the time-domain solution of Maxwell's equation for the problem of a dipole in free-space. This solution is combined with the image theory [3] to take the effect of the ground into account.

Chapter 3 reviews the massive volume of research done on the subject of dipole radiation above finitely-conductive ground. Next, two fundamental and experimentally validated methods towards this problem are introduced and the formulas for the electric and magnetic fields are reviewed in detail. The first method reviewed in this chapter is King's proposed frequency-domain solution to Maxwell's equations using a Fourier-like transformation [16]-[19]. The mathematical manipulations and all the approximations used in this method are discussed in detail. The second technique is the complex image theory proposed by Bannister [11]-[14]. This technique is mainly based on solving the integrals encountered in Sommerfeld's solution using mathematical approximations. The physical interpretation of such approximations and the validity of this method are discussed in detail.

In Chapter 4, a parametric study on the scaling of different quantities affecting the behaviour of a transmission line is done and an appropriate scale factor for each parameter is derived.

Chapter 5 presents the implementation details of different techniques introduced in this thesis. The results obtained by applying these methods for different geometries and different source excitation waveforms are shown and discussed.

Chapter 6 summarizes the work done in this research and discusses the possible future work to be accomplished.

The methods proposed by King and Bannister are based on complicated mathematical manipulations. Appendix A and B of this thesis present the computational work done by King and Bannister in detail.

To study the effect of the conductor sag on the power transmission line electromagnetic fields, the exact shape of the catenary is considered before decomposing the line into short dipoles. The modifications applied to make the calculations more accurate are discussed in Appendix C of this thesis.

Chapter 2

Electric and Magnetic Field Emission over PEC Ground

2.1 The Dipole Technique

One of the methods mainly used for calculating the emitted electric and magnetic fields from an energized body is the dipole technique [4]-[10]. In this technique, the source is assumed to be made up of a large number of short dipoles. The total radiated electromagnetic field in the vicinity of the radiating body can be found as the summation of all the contributions from each constituent dipole. All the constituent dipoles are required to be much smaller than the wavelength of the current and voltage signals. In antenna theory, such dipoles are called Hertzian, short, or infinitesimal dipoles [3]. Hertzian dipole is a radiating wire which is short enough so that the current passing through it can be considered to be constant along its whole length. Hertzian dipole is a theoretical concept and cannot physically exist [3]; however, a very short dipole antenna is a reasonable approximation.

Due to its usability, the dipole technique, also known as Hertzian dipole technique, has been used for finding the electric and magnetic fields from a transmission line [8]-[10]. In this application, the main idea is to decompose a transmission line into many small segments. Each segment can be considered as a small dipole antenna. The dipole technique requires only knowledge of the current density of the radiating body as a function of time and space. The configuration of a decomposed horizontal wire is shown in Figure 2.1 [9].

Hertzian dipole technique requires the segments to be very short comparing to the shortest wavelength of the transmission line current. Also the distance between the observation point and each of the constituent dipoles should be greater than the length of the segments. Consequently, the main drawback of the dipole technique is the considerable computation time of this approach for a valid implementation.

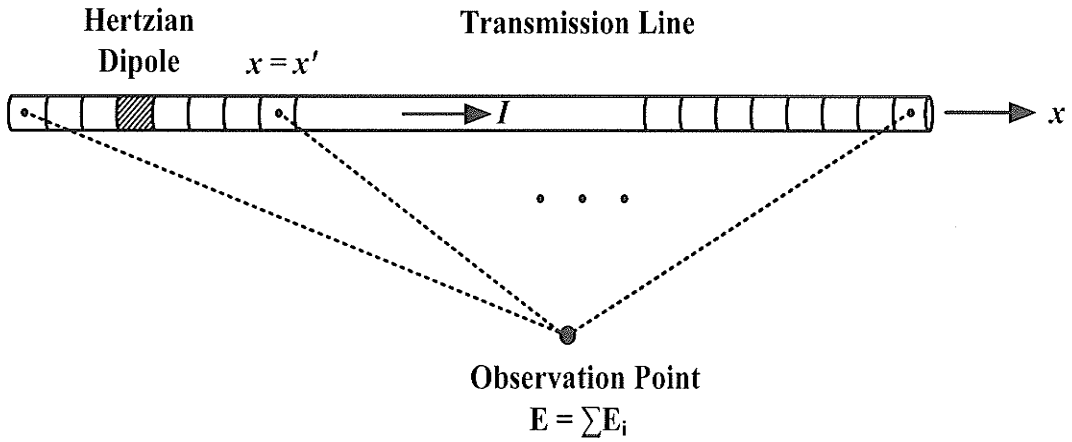

Figure 2.1. Configuration of a horizontal current-carrying wire, decomposed into small dipoles.

Two other techniques have been proposed to approach the problem of radiation from a transmission line. The first technique is the ramp method [30], in which the transient current waveform carried by the transmission line, is decomposed into a number of ramp functions. The total electromagnetic field is then obtained as the summation of the responses to all the ramp functions. The accuracy of this model is heavily dependent on the number of ramp functions used for the approximation [30]-[32]. This model's applicability is limited to simple radiating structures for which the ramp response of the system is already obtained [30]-[32]. The second method is an analytical approach to solve the Telegrapher's equations [31]-[33]. This analytical technique has been applied to both lossless [31] and [32], and lossy [33] power transmission lines. In this approach, the line is approximated as an infinitely long structure and the ground is assumed to be PEC.

Despite the expensive time-consumption of the dipole technique, due to its general form, it can be incorporated to find the electromagnetic fields in the vicinity of a lossy sagged power transmission line with a finite length, located above lossy ground. This is the main reason for choosing this approach in this thesis.

Ease of use and generality of the dipole technique have made it possible to apply this method for a wide range of applications in power system and electromagnetic interference problems. Some of the applications of this method which have been studied in the literature can be listed as power system switching transients [10], high-frequency radiation from interconnect cables [8], lightning return stroke modelling [1] and [7], transients due to power electronic converters [34], and electromagnetic radiation in high voltage substations [9].

It has been shown that as the dipole size approaches zero, the results of the dipole technique will be the same as those given by the exact analytical model (if such solution exists) [31] and [32].

2.2 Radiation from a Horizontal Dipole

As discussed in the previous section, in order to find the total electromagnetic field in the vicinity of a power transmission line, first we need to find the contribution of each constituent dipole on the electric and magnetic fields. In this section, we derive the time-domain electromagnetic field expressions associated with a finite-length dipole.

The conventional solution to find the EM radiation from a finite-length antenna starts with the time-domain Maxwell's equations for a single antenna in free-space [4]-[7],

$$\nabla . \mathbf{E} = \rho/\epsilon_0, \tag{2.1}$$

$$\nabla . \mathbf{B} = 0, \tag{2.2}$$

$$\nabla \times \mathbf{E} = -\partial \mathbf{B}/\partial t, \tag{2.3}$$

$$\nabla \times \mathbf{B} = \mu_0 \mathbf{J} + \left(\frac{1}{c^2}\right)\frac{\partial \mathbf{E}}{\partial t}, \tag{2.4}$$

where,

$$c^2 = 1/\mu_0\epsilon_0, \tag{2.5}$$

and ϵ_0 and μ_0 are the permittivity and permeability of the air, respectively.

The convenient way to solve these four fundamental equations is to write the electric and magnetic fields in terms of scalar and vector potentials and solve for the potential

quantities first. From the knowledge of scalar electric potential, ϕ, and vector magnetic potential, **A**, we can find the electric field, **E**, and magnetic field, **B**, vectors as,

$$\mathbf{E} = -\nabla\phi - \partial\mathbf{A}/\partial t, \tag{2.6}$$

and,

$$\mathbf{B} = \nabla \times \mathbf{A}, \tag{2.7}$$

where,

$$\phi(\mathbf{r}, t) = \frac{1}{4\pi\epsilon_0}\int_{V'}\frac{\rho(\mathbf{r}', t - R/c)}{R}dV', \tag{2.8}$$

$$\mathbf{A}(\mathbf{r}, t) = \frac{\mu_0}{4\pi}\int_{V'}\frac{\mathbf{J}(\mathbf{r}', t - R/c)}{R}dV', \tag{2.9}$$

and, we choose

$$\nabla.\mathbf{A} + \left(\frac{1}{c^2}\right)\frac{\partial\phi}{\partial t} = 0, \tag{2.10}$$

where R is the distance between the dipole and the observation point [4], [7].

Consider a horizontal small isolated dipole of length L, located at the point $\mathbf{r}'$ in free-space and carrying an arbitrary current $i(\mathbf{r}', t)$ [7]. The electric field intensity, **E**, and the magnetic flux density, **B**, at any arbitrary point, **r**, in the space may be derived in the time-domain, from Maxwell's equations in terms of the vector potential, $\mathbf{A}(\mathbf{r}, t)$:

$$\mathbf{E}(\mathbf{r}, t) = -\frac{\partial\mathbf{A}(\mathbf{r}, t)}{\partial t} + c^2\int_{-\infty}^{t}\nabla[\nabla.\mathbf{A}(\mathbf{r}, \tau)]d\tau, \tag{2.11}$$

where,

$$\mathbf{A}(\mathbf{r},t) = \frac{\mu_0 \mathbf{L}}{4\pi}\left[i\left(\mathbf{r}',t-\frac{|\mathbf{r}-\mathbf{r}'|}{c}\right)\right]\Big/|\mathbf{r}-\mathbf{r}'|. \tag{2.12}$$

I have used the usual notation of representing field points by unprimed coordinates and source points by primed coordinates. Figure 2.2 shows the configuration of the dipole and observation point in free-space [5].

Without loss of generality and just to make the calculations simpler, the dipole can be assumed to be located at the origin and extended along the x-axis. The procedure to be followed for finding the field expressions is the well-known method used by Uman [6] and [7], which is re-derived for the Cartesian coordinate system. Deriving the field expressions in the Cartesian coordinate system allows us to directly apply superposition to the contribution of each dipole.

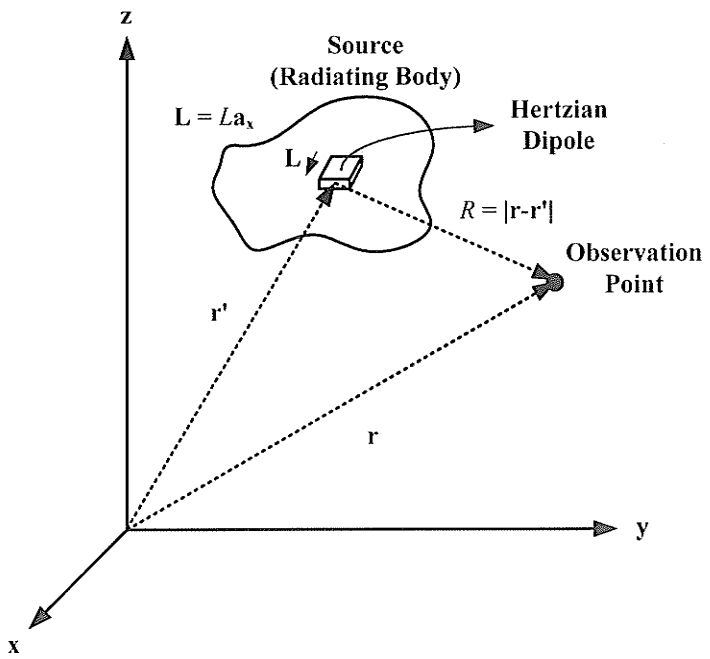

Figure 2.2. A horizontal dipole in free-space.

The vector potential associated with a horizontal dipole located at the origin of coordinate system, shown in Figure 2.3, is given as:

$$\mathbf{A} = A_x \hat{\mathbf{a}}_x = \left[\frac{\mu_0 L}{4\pi}\frac{i(t-R/c)}{R}\right]\hat{\mathbf{a}}_x. \tag{2.13}$$

From Equation (2.7) we find,

$$\mathbf{B} = \nabla \times \mathbf{A} = \frac{\mu_0 L}{4\pi}\begin{vmatrix} \hat{\mathbf{a}}_x & \hat{\mathbf{a}}_y & \hat{\mathbf{a}}_z \\ \frac{\partial}{\partial x} & \frac{\partial}{\partial y} & \frac{\partial}{\partial z} \\ \frac{i(t-R/c)}{R} & 0 & 0 \end{vmatrix}. \tag{2.14}$$

Thus,

$$\begin{aligned} \mathbf{B} &= \frac{\mu_0 L}{4\pi}\left\{\hat{\mathbf{a}}_y \frac{\partial}{\partial z}\left[\frac{i(t-R/c)}{R}\right] - \hat{\mathbf{a}}_z \frac{\partial}{\partial y}\left[\frac{i(t-R/c)}{R}\right]\right\} \\ &= \frac{\mu_0 L}{4\pi}\left\{\frac{\partial}{\partial z}\left(\frac{1}{R}\right) i(t-R/c) + \left(\frac{1}{R}\right)\frac{\partial i(t-R/c)}{\partial z}\right\}\hat{\mathbf{a}}_y \\ &\quad - \frac{\mu_0 L}{4\pi}\left\{\frac{\partial}{\partial y}\left(\frac{1}{R}\right) i(t-R/c) - \left(\frac{1}{R}\right)\frac{\partial i(t-R/c)}{\partial y}\right\}\hat{\mathbf{a}}_z. \end{aligned} \tag{2.15}$$

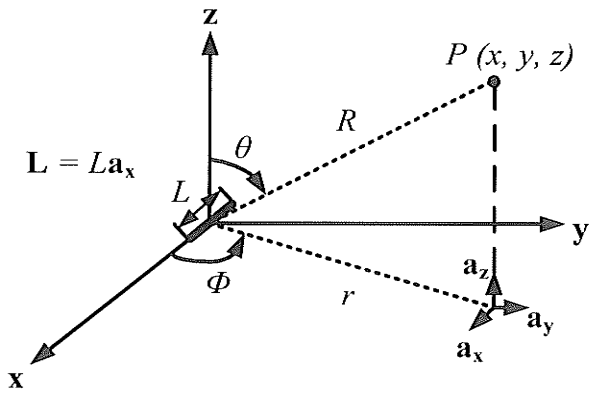

Figure 2.3. Geometry of an *x*-directed horizontal dipole, located at the origin in free-space.

Since,

$$R = (x^2 + y^2 + z^2)^{1/2}, \tag{2.16}$$

it follows that,

$$\frac{\partial}{\partial y}[i(t - R/c)] = -\frac{y}{cR} i'(t - R/c), \tag{2.17}$$

and,

$$\frac{\partial}{\partial t}[i(t - R/c)] = i'(t - R/c), \tag{2.18}$$

where primes indicate derivatives with respect to the whole argument, $(t - R/c)$ [7].

Using the above equations, we can find the relation between the time and space derivatives of the current as follows,

$$\frac{\partial i(t - R/c)}{\partial x} = -\left(\frac{x}{cR}\right)\frac{\partial i(t - R/c)}{\partial t}, \tag{2.19}$$

$$\frac{\partial i(t - R/c)}{\partial y} = -\left(\frac{y}{cR}\right)\frac{\partial i(t - R/c)}{\partial t}, \tag{2.20}$$

$$\frac{\partial i(t - R/c)}{\partial z} = -\left(\frac{z}{cR}\right)\frac{\partial i(t - R/c)}{\partial t}. \tag{2.21}$$

To simplify Equation (2.15), we will also need the following relations for the space derivatives,

$$\frac{\partial}{\partial x}\left(\frac{1}{R}\right) = -\frac{x}{R^3}, \tag{2.22}$$

$$\frac{\partial}{\partial y}\left(\frac{1}{R}\right) = -\frac{y}{R^3}, \tag{2.23}$$

$$\frac{\partial}{\partial z}\left(\frac{1}{R}\right) = -\frac{z}{R^3}. \tag{2.24}$$

Now, by substituting Equations (2.19)-(2.24) into Equation (2.15), we can write the whole expression for the magnetic flux density vector, **B**, as,

$$\begin{aligned}\mathbf{B} = \frac{-\mu_0 Lz}{4\pi}\left\{\left(\frac{1}{R^3}\right)i(t-R/c) + \left(\frac{1}{cR^2}\right)\frac{\partial i(t-R/c)}{\partial t}\right\}\hat{\mathbf{a}}_\mathbf{y} \\ + \frac{\mu_0 Ly}{4\pi}\left\{\left(\frac{1}{R^3}\right)i(t-R/c) + \left(\frac{1}{cR^2}\right)\frac{\partial i(t-R/c)}{\partial t}\right\}\hat{\mathbf{a}}_\mathbf{z}.\end{aligned} \tag{2.25}$$

To determine the expression for the electric field intensity, we need to make use of Equation (2.11) [7]. We begin by finding,

$$\begin{aligned}\nabla.\mathbf{A} = \frac{\partial A_x}{\partial x} &= \left(\frac{\mu_0 L}{4\pi}\right)\frac{\partial}{\partial x}\left[\frac{i(t-R/c)}{R}\right] \\ &= \frac{\mu_0 L}{4\pi}\left[\left(\frac{1}{R}\right)\frac{\partial i(t-R/c)}{\partial x} - \left(\frac{x}{R^3}\right)i(t-R/c)\right].\end{aligned} \tag{2.26}$$

The integrand in (2.11) is given by,

$$\begin{aligned}\nabla(\nabla.\mathbf{A}) = \frac{\mu_0 L}{4\pi}&\left\{\frac{\partial}{\partial x}\left[\left(\frac{1}{R}\right)\frac{\partial i(t-R/c)}{\partial x}\right] - \frac{\partial}{\partial x}\left[\left(\frac{x}{R^3}\right)i(t-R/c)\right]\right\}\hat{\mathbf{a}}_\mathbf{x} \\ &+ \frac{\mu_0 L}{4\pi}\left\{\frac{\partial}{\partial y}\left[\left(\frac{1}{R}\right)\frac{\partial i(t-R/c)}{\partial x}\right]\right. \\ &\left. - \frac{\partial}{\partial y}\left[\left(\frac{x}{R^3}\right)i(t-R/c)\right]\right\}\hat{\mathbf{a}}_\mathbf{y} \\ &+ \frac{\mu_0 L}{4\pi}\left\{\frac{\partial}{\partial z}\left[\left(\frac{1}{R}\right)\frac{\partial i(t-R/c)}{\partial x}\right]\right. \\ &\left. - \frac{\partial}{\partial z}\left[\left(\frac{x}{R^3}\right)i(t-R/c)\right]\right\}\hat{\mathbf{a}}_\mathbf{z}.\end{aligned} \tag{2.27}$$

By expanding Equation (2.27), we will have

$$\begin{aligned}\frac{\nabla(\nabla.\mathbf{A})}{\mu_0 L/4\pi} = &\left[\left(-\frac{x}{R^3}\right)\frac{\partial i(t-R/c)}{\partial z}+\left(\frac{1}{R}\right)\frac{\partial^2 i(t-R/c)}{\partial x\partial z}\right.\\ &\left.+\left(\frac{3xz}{R^5}\right)i(t-R/c)-\left(\frac{z}{R^3}\right)\frac{\partial i(t-R/c)}{\partial x}\right]\hat{\mathbf{a}}_{\mathbf{x}}\\ &+\left[\left(-\frac{y}{R^3}\right)\frac{\partial i(t-R/c)}{\partial z}+\left(\frac{1}{R}\right)\frac{\partial^2 i(t-R/c)}{\partial y\partial z}\right.\\ &\left.+\left(\frac{3yz}{R^5}\right)i(t-R/c)-\left(\frac{z}{R^3}\right)\frac{\partial i(t-R/c)}{\partial y}\right]\hat{\mathbf{a}}_{\mathbf{y}}\\ &+\left[\left(-\frac{z}{R^3}\right)\frac{\partial i(t-R/c)}{\partial z}+\left(\frac{1}{R}\right)\frac{\partial^2 i(t-R/c)}{\partial z^2}\right.\\ &-\left(\frac{1}{R^3}\right)i(t-R/c)+\left(\frac{3z^2}{R^5}\right)i(t-R/c)\\ &\left.-\left(\frac{z}{R^3}\right)\frac{\partial i(t-R/c)}{\partial z}\right]\hat{\mathbf{a}}_{\mathbf{z}}.\end{aligned} \tag{2.28}$$

By applying the relations between time and space derivatives found in Equations (2.19)-(2.21), it is shown that,

$$\begin{aligned}\frac{\partial^2 i(t-R/c)}{\partial y\partial x} &= \frac{\partial}{\partial y}\left[\left(\frac{-x}{cR}\right)\frac{\partial i(t-R/c)}{\partial t}\right]\\ &= -\left(\frac{x}{c}\right)\left[\left(\frac{-y}{R^3}\right)\frac{\partial i(t-R/c)}{\partial t}+\left(\frac{1}{R}\right)\left(\frac{-y}{cR}\right)\frac{\partial^2 i(t-R/c)}{\partial t^2}\right],\end{aligned} \tag{2.29}$$

$$\begin{aligned}\frac{\partial^2 i(t-R/c)}{\partial z\partial x} &= \frac{\partial}{\partial z}\left[\left(\frac{x}{cR}\right)\frac{\partial i(t-R/c)}{\partial t}\right]\\ &= -\left(\frac{x}{c}\right)\left[\left(\frac{-z}{R^3}\right)\frac{\partial i(t-R/c)}{\partial t}+\left(\frac{1}{R}\right)\left(\frac{-z}{cR}\right)\frac{\partial^2 i(t-R/c)}{\partial t^2}\right],\end{aligned} \tag{2.30}$$

$$\frac{\partial^2 i(t-R/c)}{\partial x^2} = \frac{\partial}{\partial x}\left[\left(\frac{-x}{cR}\right)\frac{\partial i(t-R/c)}{\partial t}\right]$$

$$= \left(-\frac{1}{cR}\right)\frac{\partial i(t-R/c)}{\partial t} + \left(\frac{x^2}{cR^3}\right)\frac{\partial i(t-R/c)}{\partial t} \tag{2.31}$$

$$+ \left(\frac{x^2}{c^2R^2}\right)\frac{\partial^2 i(t-R/c)}{\partial t^2}.$$

Also, from Equation (2.12) we have,

$$\frac{\partial \mathbf{A}}{\partial t} = \frac{L}{4\pi\epsilon_0 c^2}\left[\left(\frac{1}{R}\right)\frac{\partial i(t-R/c)}{\partial t}\right]\hat{\mathbf{a}}_\mathbf{x}. \tag{2.32}$$

Substituting (2.29)-(2.31) into Equation (2.28) yields,

$$\frac{\nabla(\nabla.\mathbf{A})}{\mu_0 L/4\pi} = \left\{\left(\frac{3x^2}{R^5}-\frac{1}{R^3}\right)i(t-R/c) + \left(\frac{3x^2}{cR^4}-\frac{1}{cR^2}\right)\frac{\partial i(t-R/c)}{\partial t}\right.$$

$$\left. + \left(\frac{x^2}{c^2R^3}\right)\frac{\partial^2 i(t-R/c)}{\partial t^2}\right\}\hat{\mathbf{a}}_\mathbf{x}$$

$$+ \left\{\left(\frac{3xy}{R^5}\right)i(t-R/c) + \left(\frac{3xy}{cR^4}\right)\frac{\partial i(t-R/c)}{\partial t}\right.$$

$$\left. + \left(\frac{xy}{c^2R^3}\right)\frac{\partial^2 i(t-R/c)}{\partial t^2}\right\}\hat{\mathbf{a}}_\mathbf{y} \tag{2.33}$$

$$+ \left\{\left(\frac{3xz}{R^5}\right)i(t-R/c) + \left(\frac{3xz}{cR^4}\right)\frac{\partial i(t-R/c)}{\partial t}\right.$$

$$\left. + \left(\frac{xz}{c^2R^3}\right)\frac{\partial^2 i(t-R/c)}{\partial t^2}\right\}\hat{\mathbf{a}}_\mathbf{z}.$$

Now we can write the second term on the right side of Equation (2.11) as,

$$
\begin{aligned}
c^2\int_{-\infty}^{t}\nabla(\nabla.\mathbf{A})d\tau \;=\; & \frac{L}{4\pi\epsilon_0}\left\{\left(\frac{3x^2}{R^5}-\frac{1}{R^3}\right)\int_0^t i(\tau-R/c)d\tau\right. \\
& +\left(\frac{3x^2}{cR^4}-\frac{1}{cR^2}\right)i(t-R/c)+\left.\left(\frac{x^2}{c^2R^3}\right)\frac{\partial i(t-R/c)}{\partial t}\right\}\hat{\mathbf{a}}_{\mathrm{x}} \\
& +\frac{L}{4\pi\epsilon_0}\left\{\left(\frac{3xy}{R^5}\right)\int_0^t i(\tau-R/c)d\tau+\left(\frac{3xy}{cR^4}\right)i(t-R/c)\right. \\
& \left.+\left(\frac{xy}{c^2R^3}\right)\frac{\partial i(t-R/c)}{\partial t}\right\}\hat{\mathbf{a}}_{\mathrm{y}} \\
& +\frac{L}{4\pi\epsilon_0}\left\{\left(\frac{3xz}{R^5}\right)\int_0^t i(\tau-R/c)d\tau+\left(\frac{3xz}{cR^4}\right)i(t-R/c)\right. \\
& \left.+\left(\frac{xz}{c^2R^3}\right)\frac{\partial i(t-R/c)}{\partial t}\right\}\hat{\mathbf{a}}_{\mathrm{z}}.
\end{aligned}
\tag{2.34}
$$

Thus, substituting (2.32) and (2.34) into (2.11) yields

$$
\begin{aligned}
\mathbf{E} \;=\; & \frac{L}{4\pi\epsilon_0}\left\{\left(\frac{3x^2}{R^5}-\frac{1}{R^3}\right)\int_0^t i(\tau-R/c)d\tau+\left(\frac{3x^2}{cR^4}-\frac{1}{cR^2}\right)i(t-R/c)\right. \\
& \left.+\left(\frac{x^2}{c^2R^3}-\frac{1}{c^2R}\right)\frac{\partial i(t-R/c)}{\partial t}\right\}\hat{\mathbf{a}}_{\mathrm{x}} \\
& +\frac{L}{4\pi\epsilon_0}\left\{\left(\frac{3xy}{R^5}\right)\int_0^t i(\tau-R/c)d\tau+\left(\frac{3xy}{cR^4}\right)i(t-R/c)\right. \\
& \left.+\left(\frac{xy}{c^2R^3}\right)\frac{\partial i(t-R/c)}{\partial t}\right\}\hat{\mathbf{a}}_{\mathrm{y}} \\
& +\frac{L}{4\pi\epsilon_0}\left\{\left(\frac{3xz}{R^5}\right)\int_0^t i(\tau-R/c)d\tau+\left(\frac{3xz}{cR^4}\right)i(t-R/c)\right. \\
& \left.+\left(\frac{xz}{c^2R^3}\right)\frac{\partial i(t-R/c)}{\partial t}\right\}\hat{\mathbf{a}}_{\mathrm{z}}.
\end{aligned}
\tag{2.35}
$$

In Equation (2.35), the terms proportional to the integral of the current are called the electrostatic fields. In Equations (2.25) and (2.35), the terms proportional to the current are called the induction fields, and the terms proportional to the derivative of the current are the radiation fields [4]-[5], [7].

It should be pointed out that the electrostatic, induction, and radiation terms will respectively be the dominant terms in the near, intermediate, and far distances.

Equations (2.25) and (2.35) represent the field equations when the dipole is located at the origin. If the dipole lies along the z-axis at an arbitrary coordinate z', the field may be obtained by substituting $(z - z')$ for z in Equations (2.25) and (2.35). Similarly, if we move the dipole to the point (x', y', z'), the total field can be found simply by substituting $(x - x')$ for x, $(y - y')$ for y, and $(z - z')$ for z in Equations (2.25) and (2.35) [7].

2.3 Radiation from a Vertical Dipole

In Chapter 4 and Appendix C, it will be shown that in order to take the effect of sag of the conductor into account, we can decompose each segment of the transmission line into horizontal and vertical vectors as shown in Figure 2.4. This technique provides a more accurate approximation for the fields radiated from a transmission line especially in the transient case.

Consequently, we need to determine the expressions for the electric and magnetic fields, associated with a vertical dipole. For the case of a dipole, located in free-space, this is simply achieved by applying a rotation of the coordinate system to the results of a horizontal dipole.

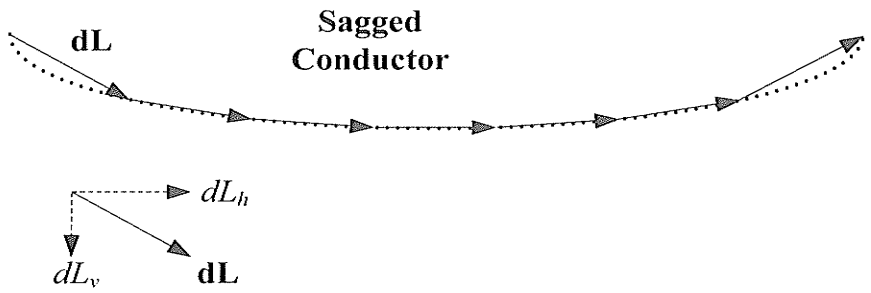

Figure 2.4. Configuration of an arbitrarily-oriented segment of a sagged conductor, decomposed into horizontal and vertical segments.

For a vertical dipole shown in Figure 2.5, the time-domain vector potential is given by,

$$\mathbf{A} = A_z\hat{\mathbf{a}}_z = \left[\left(\frac{\mu_0 L}{4\pi}\right)\frac{i(t - R/c)}{R}\right]\hat{\mathbf{a}}_z. \tag{2.36}$$

Following the same procedure used in the previous section, we can determine expressions for the magnetic flux density and the electric field intensity [4]-[7] as,

$$\mathbf{B} = B_x\hat{\mathbf{a}}_x + B_y\hat{\mathbf{a}}_y, \tag{2.37}$$

where,

$$B_x = \frac{-\mu_0 Ly}{4\pi}\left\{\left(\frac{1}{R^3}\right)i(t - R/c) + \left(\frac{1}{cR^2}\right)\frac{\partial i(t - R/c)}{\partial t}\right\}, \tag{2.38}$$

$$B_y = \frac{\mu_0 Lx}{4\pi}\left\{\left(\frac{1}{R^3}\right)i(t - R/c) + \left(\frac{1}{cR^2}\right)\frac{\partial i(t - R/c)}{\partial t}\right\}. \tag{2.39}$$

And,

$$\mathbf{E} = E_x\hat{\mathbf{a}}_x + E_y\hat{\mathbf{a}}_y + E_z\hat{\mathbf{a}}_z, \tag{2.40}$$

where,

$$E_x = \frac{L}{4\pi\epsilon_0}\left\{\left(\frac{3xz}{R^5}\right)\int_0^t i(\tau - R/c)d\tau + \left(\frac{3xz}{cR^4}\right)i(t - R/c) + \left(\frac{xz}{c^2R^3}\right)\frac{\partial i(t - R/c)}{\partial t}\right\}, \tag{2.41}$$

$$E_y = \frac{L}{4\pi\epsilon_0}\left\{\left(\frac{3yz}{R^5}\right)\int_0^t i(\tau - R/c)d\tau + \left(\frac{3yz}{cR^4}\right)i(t - R/c) + \left(\frac{yz}{c^2R^3}\right)\frac{\partial i(t - R/c)}{\partial t}\right\}, \tag{2.42}$$

$$E_z = \frac{L}{4\pi\epsilon_0}\left\{\left(\frac{3z^2}{R^5} - \frac{1}{R^3}\right)\int_0^t i(\tau - R/c)d\tau + \left(\frac{3z^2}{cR^4} - \frac{1}{cR^2}\right)i(t - R/c) + \left(\frac{z^2}{c^2R^3} - \frac{1}{c^2R}\right)\frac{\partial i(t - R/c)}{\partial t}\right\}. \tag{2.43}$$

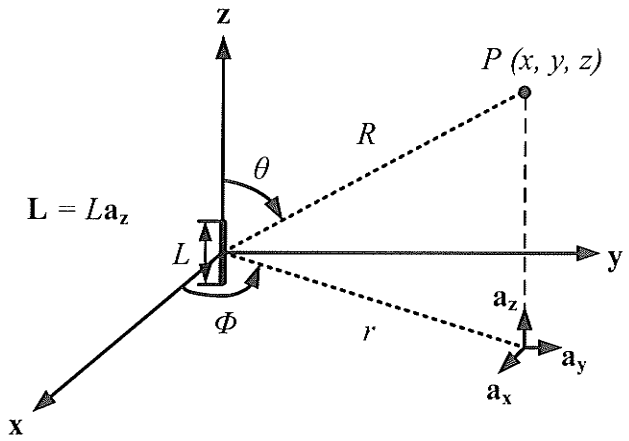

Figure 2.5. Geometry of a vertical dipole, located at the origin in free-space.

2.4 Extension of the Results to the Case of an Arbitrarily-Oriented Dipole

The electromagnetic field expressions of a vertical infinitesimal dipole, located on the z-axis were obtained in section 2.3. Now, consider the infinitesimal dipole shown in Figure 2.6, located at point $P'(x', y', z')$, with an arbitrary orientation defined by the unit vector: $\mathbf{n} = \cos\alpha\,\hat{\mathbf{a}}_x + \cos\beta\,\hat{\mathbf{a}}_y + \cos\gamma\,\hat{\mathbf{a}}_z$ [35].

In order to calculate the value of electromagnetic fields at a given point $P(x_0, y_0, z_0)$, we need to derive a generalized form of the equations derived in the previous section. The equation for line Γ is given as,

$$\frac{x_1 - x'}{\cos\alpha} = \frac{y_1 - y'}{\cos\beta} = \frac{z_1 - z'}{\cos\gamma} = k. \tag{2.44}$$

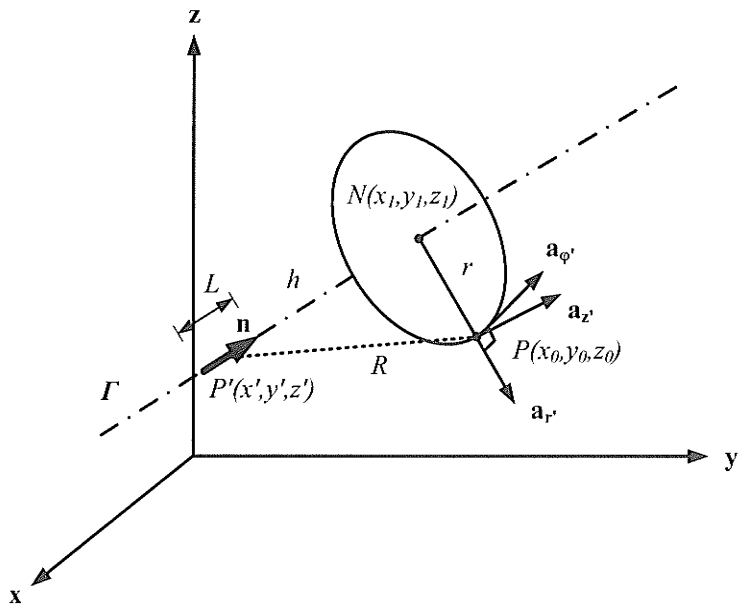

Figure 2.6. Configuration of an infinitesimal dipole with an arbitrary orientation in free-space.

The parametric form of the line equation can be derived as [35]:

$$\begin{cases} x_1 = k\cos\alpha + x' \\ y_1 = k\cos\beta + y'. \\ z_1 = k\cos\gamma + z' \end{cases} \tag{2.45}$$

Since **n** and **NP** vectors are perpendicular to each other, we have

$$\mathbf{n}.\mathbf{NP} = 0 \rightarrow [\cos\alpha \quad \cos\beta \quad \cos\gamma] \begin{bmatrix} x_0 - k\cos\alpha - x' \\ y_0 - k\cos\beta - y' \\ z_0 - k\cos\gamma - z' \end{bmatrix} = 0. \tag{2.46}$$

From (2.46), we conclude,

$$k = (x_0 - x')\cos\alpha + (y_0 - y')\cos\beta + (z_0 - z')\cos\gamma. \tag{2.47}$$

Further,

$$r = \sqrt{(x_1 - x_0)^2 + (y_1 - y_0)^2 + (z_1 - z_0)^2}, \tag{2.48}$$

and,

$$h = \sqrt{(x_1 - x')^2 + (y_1 - y')^2 + (z_1 - z')^2}\,\mathrm{sgn}(\mathbf{n}.\mathbf{P'N}), \tag{2.49}$$

where,

$$\mathrm{sgn}(x) = \begin{cases} 1 & x > 0 \\ 0 & x = 0. \\ -1 & x < 0 \end{cases} \tag{2.50}$$

As a result,

$$\mathbf{n}.\mathbf{P'N} = (x_1 - x')\cos\alpha + (y_1 - y')\cos\beta + (z_1 - z')\cos\gamma. \tag{2.51}$$

So the unit vectors in the new coordinate system can be mapped into Cartesian unit vectors as follows [35],

$$\hat{\mathbf{a}}_{z'} = \mathbf{n} = \cos\alpha\,\hat{\mathbf{a}}_x + \cos\beta\,\hat{\mathbf{a}}_y + \cos\gamma\,\hat{\mathbf{a}}_z, \tag{2.52}$$

$$\hat{\mathbf{a}}_{r'} = \frac{\mathbf{NP}}{|\mathbf{NP}|} = \frac{x_0 - x_1}{r}\hat{\mathbf{a}}_x + \frac{y_0 - y_1}{r}\hat{\mathbf{a}}_y + \frac{z_0 - z_1}{r}\hat{\mathbf{a}}_z, \tag{2.53}$$

$$\begin{aligned}\hat{\mathbf{a}}_{\phi'} = \hat{\mathbf{a}}_{z'} \times \hat{\mathbf{a}}_{r'} = &\left(\frac{z_0 - z_1}{r} - \frac{y_0 - y_1}{r}\right)\hat{\mathbf{a}}_x + \left(\frac{x_0 - x_1}{r} - \frac{z_0 - z_1}{r}\right)\hat{\mathbf{a}}_y \\ &+ \left(-\frac{x_0 - x_1}{r}\right)\hat{\mathbf{a}}_z.\end{aligned} \tag{2.54}$$

And the components of electric and magnetic field intensity vectors associated with a dipole oriented along line L, are given as [35]:

$$E_x(P,t) = \cos\alpha\, E_h(P,t) + \frac{x_0 - x_1}{r} E_v(P,t), \tag{2.55}$$

$$E_y(P,t) = \cos\beta\, E_h(P,t) + \frac{y_0 - y_1}{r} E_v(P,t), \tag{2.56}$$

$$E_z(P,t) = \cos\gamma\, E_h(P,t) + \frac{z_0 - z_1}{r} E_v(P,t). \tag{2.57}$$

$$H_x(P,t) = (\frac{z_0 - z_1}{r}\cos\beta - \frac{y_0 - y_1}{r}\cos\gamma)H_\phi(P,t), \tag{2.58}$$

$$H_y(P,t) = (\frac{x_0 - x}{r}\cos\gamma - \frac{z_0 - z_1}{r}\cos\alpha)H_\phi(P,t), \tag{2.59}$$

$$H_z(P,t) = (\frac{y_0 - y_1}{r}\cos\alpha - \frac{x_0 - x_1}{r}\cos\beta)H_\phi(P,t). \tag{2.60}$$

where $E_h(P,t)$ and $E_v(P,t)$ are the horizontal and vertical components of the electric field, and $H_\phi(P,t)$ is the angular component of the magnetic field in the local coordinate system at point P.

Thus, the total electromagnetic fields at point P caused by a current flowing in an arbitrarily-oriented wire can be calculated by dividing the wire into segments and adding up the contributions of all segments.

2.5 The Ground Effect and Image Theory

The presence of an obstacle, especially when it is near the radiating element, can significantly change the overall radiation properties of the radiating system. The most common obstacle that is always present is the ground. Any energy from the radiating element directed toward the ground undergoes a reflection. The amount of reflected energy and its direction are controlled by the intrinsic parameters of the ground [3].

To analyze the performance of an antenna near a perfectly-conductive surface, virtual sources (images) are introduced to account for reflections [3]. As the name implies, these are not real sources but imaginary ones, which when combined with the real sources, form an equivalent system. The orientation and direction of the image dipoles for the horizontal and vertical dipoles are shown in Figure 2.7 [3].

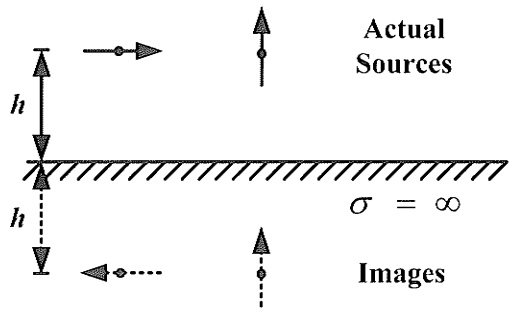

Figure 2.7. The image geometry of horizontal and vertical dipoles.

It will be shown in Chapter 3 that the concept of image theory can be modified in order to include the finite conductivity of the ground in the calculations.

Figure 2.8 shows the configuration of a line decomposed into small segments and its image below the surface of a PEC ground [9].

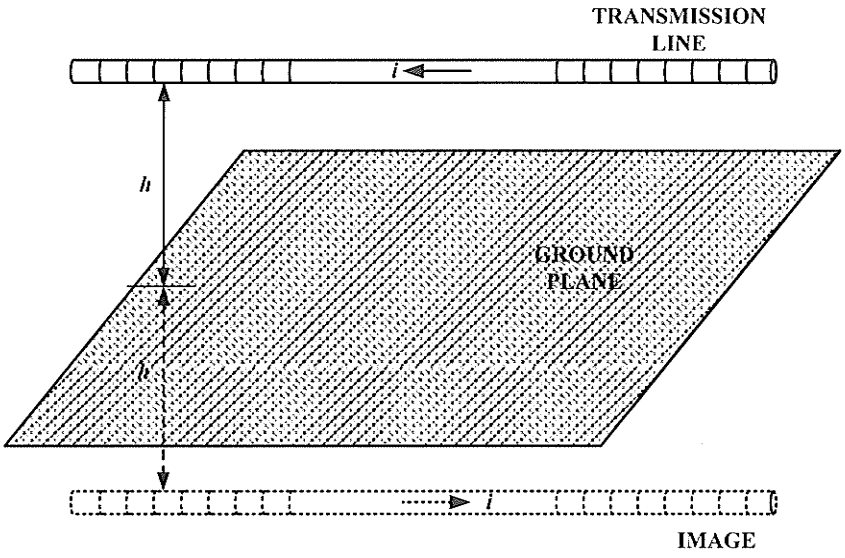

Figure 2.8. A decomposed transmission line and its image.

Chapter 3

Electric and Magnetic Field Emission over Lossy Ground

3.1 Introduction

The transient and steady-state currents and voltages present in power transmission lines produce strong electromagnetic fields with possibly unwanted effects. In the previous chapter, an analytical time-domain method was suggested to predict the magnitude of such electromagnetic fields when the line is located above hypothetical PEC ground.

In this chapter, we study the analytical methods for finding the electromagnetic fields within the vicinity of a power transmission line located above lossy ground. To implement these methods, first the dipole technique introduced in the previous chapter is used to decompose the line into a large number of small dipoles. Next, the electric and magnetic fields associated with each dipole are calculated when the dipole is placed over finitely-conductive ground. Finally, the total field is found as the summation of the fields emitted from each constituent segment.

The presence of a finitely-conductive boundary makes the electromagnetic field distribution very different from that of the same dipole in an infinite homogeneous region or over PEC ground [16]. This fact was first acknowledged more than 100 years ago by Arnold Sommerfeld [1] and [2], who derived the expressions for electromagnetic fields associated with an infinitesimal electric dipole located above a lossy half-space. Sommerfeld derived general complex integrals for the corresponding Hertz potential, from which the components of the electromagnetic fields can be determined by differentiation. The expressions for this traditional solution consist of integrals known as Sommerfeld-type that cannot be evaluated in closed form, and due to their highly oscillatory nature are difficult to calculate numerically [36].

Since then, this classic problem has received a significant amount of attention by many investigators who have tried to obtain more explicit and easily implementable expressions for the corresponding electromagnetic fields [16]. Consequently, sets of analytical approximate formulas have been derived in restricted ranges of parameters and variables [37]-[41]. These methods are mainly valid within a certain set of restrictive conditions on the distance between the source and the observation point. These ranges are mainly known as the quasi-static or near-field [42]-[44], the intermediate field [45], and the far-field or asymptotic field [46].

In this study, I have focused on the two of the main approaches applied towards this problem. In these solutions, electromagnetic integral expressions are transformed into a form that keeps the generality of the original formulation while improving the computational efficiency of the problem from a numerical implementation standpoint.

Formulas derived by King and Wu [16]-[19] provide a single continuous range over all distances from quite close distances to infinity at all useful frequencies. This set of formulas is obtained by solving the Maxwell's equations subject to a set of boundary conditions. The field expressions derived by King have been experimentally verified at f = 1-10 Hz in the exploration of the Earth's crust, at f = 25-100 Hz in the detection of submerged submarines, and at f = 0.9-1.8 GHz to determine the field in the human head due to a hand-held cellular transceiver [19].

The second method, studied and implemented in this thesis, is based on the work done by Peter Bannister [11]-[14]. As discussed in the previous chapter, basic antenna theory entails that the fields produced by a wire of any length, when placed over PEC ground, can be represented by the combined fields of the wire and its image [3]. A method known as complex image theory [12] suggests that if the reflection medium is not perfectly-conductive, the image of the source will be a line source in the complex space. Physically, the essence of complex image theory is to replace the finitely-conductive earth by a perfectly-conductive one located at the complex depth $d/2$, where $d = 2/\gamma_2$ and $\gamma_2 = [j\omega\mu_0(\sigma_2 + j\omega\epsilon_2)]^{1/2}$ is the propagation constant in the earth [11]-[14]. σ_2 and ϵ_2 are respectively the conductivity and relative permittivity of the ground.

During the past several years, complex image theory has proved to be quite useful in determining the fields of antennas located near the earth's surface for both single-layered and multi-layered ground [13]. The only restriction on the use of this technique is that it requires $|n|^2 \geq 10$, where $n = \gamma_2/\gamma_1$, and γ_1 and γ_2 are the propagation constants in the air and in the earth, respectively [14]. This condition is similar to the one required in King's formulation.

Unlike the analytical time-domain method reviewed in Chapter 2 for the case of perfectly-conductive ground, the two approaches reviewed in this chapter are frequency-domain techniques. Thus, for time-domain applications such as calculation of transient fields radiated from power transmission lines, we need to apply Fourier and inverse Fourier transforms to the current and field waveforms. In this chapter, a phasor notation is used to represent the electric and magnetic field intensity vectors.

3.2 King's Formulation

In the pioneering work of Sommerfeld [1] and [2], the electromagnetic fields associated with a horizontal electric dipole are expressed in terms of derivatives of general integrals of the Hertz potential. This formulation was also used by other investigators including, Wait [37]-[40], and [47] and Baños [41].

More recently, integrals for the components of the electromagnetic fields were derived directly from Maxwell's equation by King and Wu [16]-[19]. This last derivation is summarized here. Unlike earlier approximate formulas, the expressions derived by King provide a single continuous range over all distances from quite close to infinity at all useful frequencies. The near, intermediate, and asymptotic parts of the range join smoothly and continuously [16].

King and Wu deal directly and systematically with the field itself and not the Hertz vector [16]. Their set of formulas satisfies Maxwell's equations and the required boundary conditions consistently. The major limiting conditions on application of this method are $|k_2^2| \gg k_1^2$ and $|k_2\rho| > O(1)$, where ρ is the radial distance from the source [19]. In the sequence of approximation steps, the direct and the ideal-image fields are

separated. Some of the integrals are computed exactly by analytical means and large-argument approximation for the Bessel functions are only applied to some of the integrals [16].

3.2.1 Maxwell's Equations and Their Transformed Form

Consider the x-directed horizontal electric dipole shown in Figure 3.1, located at $z = d$ on the z-axis. The wave numbers of two regions are $k_i = \omega(\mu_0 \tilde{\epsilon}_i)^{1/2}$, where $\tilde{\epsilon}_i = \epsilon_i + j\sigma_i/\omega$ and $i = 1, 2$ [16]. It is assumed that both regions are nonmagnetic so that $\mu_1 = \mu_2 = \mu_0$. Maxwell's equations in the two regions are derived assuming $\exp(-j\omega t)$ time-dependence:

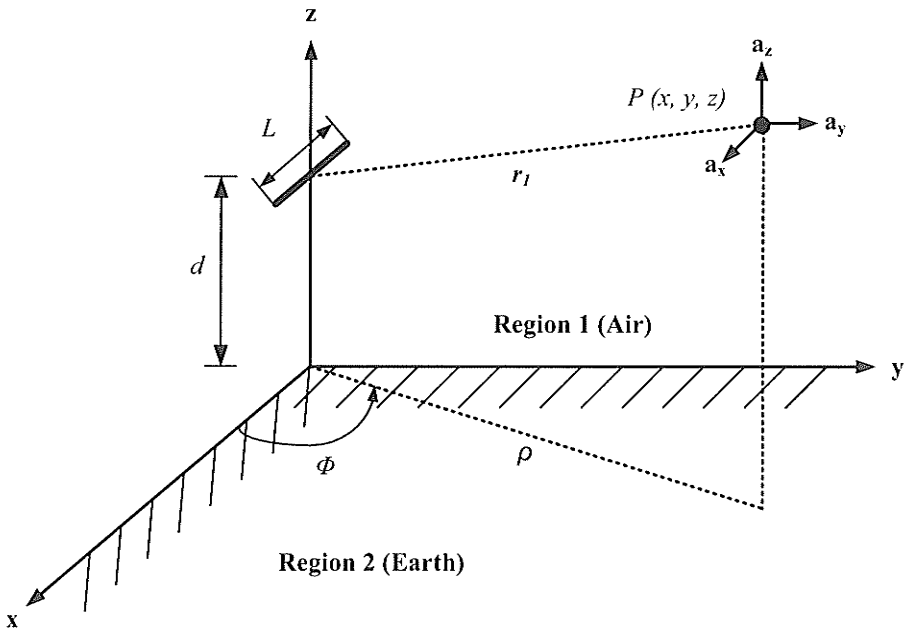

Figure 3.1. Geometry of an x-directed horizontal dipole, located on the z-axis above finitely-conductive ground.

$$\nabla \times \mathbf{E}_i = j\omega \mathbf{B}_i, \tag{3.1}$$

and,

$$\nabla \times \mathbf{B}_i = \mu_0(-j\omega\tilde{\epsilon}_i \mathbf{E}_i + \hat{\mathbf{x}} J_x), \tag{3.2}$$

where,

$$J_x = \delta(x)\delta(y)\delta(z-d). \tag{3.3}$$

is the normalized volume density of current in the dipole. Equations (3.1) and (3.2) are to be solved for $\mathbf{E}_i$ and $\mathbf{B}_i$, subject to the following boundary conditions [16],

$$E_{1x}(x,y,0) = E_{2x}(x,y,0), \tag{3.4}$$

$$E_{1y}(x,y,0) = E_{2y}(x,y,0), \tag{3.5}$$

$$k_1 E_{1z}(x,y,0) = k_2 E_{2z}(x,y,0), \tag{3.6}$$

$$\mathbf{B_1}(x,y,0) = \mathbf{B_2}(x,y,0). \tag{3.7}$$

The translational invariance of the boundary in the x- and y-directions suggests the use of the transform,

$$\mathbf{E}(x,y,z) = \frac{1}{(2\pi)^2}\int_{-\infty}^{\infty}\int_{-\infty}^{\infty} e^{j(\xi x+\eta y)}\bar{\mathbf{E}}(\xi,\eta,z)d\eta\, d\xi, \tag{3.8}$$

and a similar one for $\mathbf{B}(x,y,z)$ [16].

The transformed form of $J_x(x,y,z)$ is

$$\bar{J}_x(\xi,\eta,z) = \delta(z-d). \tag{3.9}$$

Following a massive amount of mathematical manipulations reviewed in Appendix A, the integrals present in the transformed form of Maxwell's equations can be evaluated

approximately subject to the condition $|k_2/k_1|^2 \gg 1$ [16]-[19]. The components of the electromagnetic fields at any point (ρ, ϕ, z) in the air are then obtained as below,

$$\begin{aligned} E_{1\rho}(\rho,\phi,z) = \frac{\omega\mu_0}{4\pi k_1}\cos\phi\Bigg\{ & e^{jk_1r_1}\left[\frac{2}{r_1^2}+\frac{2j}{k_1r_1^3}\right. \\ & \left.+\left(\frac{z-d}{r_1}\right)^2\left(\frac{jk_1}{r_1}-\frac{3}{r_1^2}-\frac{3j}{k_1r_1^3}\right)\right] \\ & -e^{jk_1r_2}\left[\frac{2}{r_2^2}+\frac{2j}{k_1r_2^3}+\left(\frac{z+d}{r_2}\right)^2\left(\frac{jk_1}{r_2}-\frac{3}{r_2^2}-\frac{3j}{k_1r_2^3}\right)\right. \\ & -\frac{2k_1}{k_2}\left(\frac{z+d}{r_2}\right)\left(\frac{jk_1}{r_2}-\frac{1}{r_2^2}\right) \\ & +\frac{2k_1^2}{k_2^2}\left\{\frac{jk_1}{r_2}-\frac{1}{r_2^2}-\frac{j}{k_1r_2^3}\right. \\ & \left.\left.\left.-\frac{k_1^3}{k_2}\left(\frac{r_2}{\rho}\right)\left(\frac{\pi}{k_1r_2}\right)^{1/2}e^{-jP}F(P)\right\}\right]\Bigg\}, \end{aligned} \tag{3.10}$$

$$\begin{aligned} E_{1\phi}(\rho,\phi,z) = -\frac{\omega\mu_0}{4\pi k_1}\sin\phi\Bigg(& e^{jk_1r_1}\left(\frac{jk_1}{r_1}-\frac{1}{r_1^2}-\frac{j}{k_1r_1^3}\right) \\ & -e^{ik_1r_2}\left(\frac{jk_1}{r_2}-\frac{1}{r_2^2}-\frac{j}{k_1r_2^3}\right) \\ & -e^{jk_1r_2}\left\{-\frac{2k_1}{k_2}\left(\frac{z+d}{r_2}\right)\left(\frac{jk_1}{r_2}-\frac{1}{r_2^2}\right)\right. \\ & +\frac{2k_1^2}{k_2^2}\left[\frac{2}{r_2^2}+\frac{2j}{k_1r_2^3}+\left(\frac{z+d}{r_2}\right)^2\left(\frac{jk_1}{r_2}-\frac{3}{r_2^2}-\frac{3j}{k_1r_2^3}\right)\right. \\ & \left.\left.\left.+\frac{2jk_1^4}{k_2^3\rho}\left(\frac{r_2}{\rho}\right)^2\left(\frac{\pi}{k_1r_2}\right)^{1/2}e^{-jP}F(P)\right]\right\}\Bigg), \end{aligned} \tag{3.11}$$

$$E_{1z}(\rho,\phi,z) = \frac{\omega\mu_0}{4\pi k_1}\cos\phi\left\{-e^{jk_1r_1}\left(\frac{\rho}{r_1}\right)\left(\frac{z-d}{r_1}\right)\left(\frac{jk_1}{r_1}-\frac{3}{r_1^2}-\frac{3j}{k_1r_1^3}\right)\right.$$
$$+e^{jk_1r_2}\left(\frac{\rho}{r_2}\right)\left(\frac{z+d}{r_2}\right)\left(\frac{jk_1}{r_2}-\frac{3}{r_2^2}-\frac{3j}{k_1r_2^3}\right)$$
$$-\frac{2k_1}{k_2}e^{jk_1r_2}\left[\left(\frac{\rho}{r_2}\right)\left(\frac{jk_1}{r_2}-\frac{1}{r_2^2}\right)\right.$$
$$\left.\left.-\frac{k_1^3}{k_2}\left(\frac{\pi}{k_1r_2}\right)^{1/2}e^{-jP}F(P)\right]\right\}, \tag{3.12}$$

$$B_{1\rho}(\rho,\phi,z) = \frac{\mu_0}{4\pi}\sin\phi\left\{e^{jk_1r_1}\left(\frac{z-d}{r_1}\right)\left(\frac{jk_1}{r_1}-\frac{1}{r_1^2}\right)\right.$$
$$-e^{jk_1r_2}\left(\frac{z+d}{r_2}\right)\left(\frac{jk_1}{r_2}-\frac{1}{r_2^2}\right)$$
$$+\frac{2k_1}{k_2}e^{jk_1r_2}\left[\frac{2}{r_2^2}+\frac{2j}{k_1r_2^3}+\left(\frac{z+d}{r_2}\right)^2\left(\frac{jk_1}{r_2}-\frac{3}{r_2^2}-\frac{3j}{k_1r_2^3}\right)\right.$$
$$\left.\left.+\frac{jk_1^2}{k_2\rho}\left(\frac{r_2}{\rho}\right)^2\left(\frac{\pi}{k_1r_2}\right)^{1/2}e^{-jP}F(P)\right]\right\}, \tag{3.13}$$

$$B_{1\phi}(\rho,\phi,z) = \frac{\mu_0}{4\pi}\cos\phi\left\{e^{jk_1r_1}\left(\frac{z-d}{r_1}\right)\left(\frac{jk_1}{r_1}-\frac{1}{r_1^2}\right)\right.$$
$$-e^{jk_1r_2}\left(\frac{z+d}{r_2}\right)\left(\frac{jk_1}{r_2}-\frac{1}{r_2^2}\right)$$
$$+\frac{2k_1}{k_2}e^{jk_1r_2}\left[\frac{jk_1}{r_2}-\frac{1}{r_2^2}-\frac{j}{k_1r_2^3}\right.$$
$$\left.\left.-\frac{k_1^3}{k_2}\left(\frac{r_2}{\rho}\right)\left(\frac{\pi}{k_1r_2}\right)^{1/2}e^{-jP}F(P)\right]\right\}, \tag{3.14}$$

$$
\begin{aligned}
B_{1z}(\rho,\phi,z) \;=\; & -\frac{\mu_0}{4\pi}\sin\phi\left(e^{jk_1r_1}\left(\frac{\rho}{r_1}\right)\left(\frac{jk_1}{r_1}-\frac{1}{r_1^2}\right)\right. \\
& -e^{jk_1r_2}\left(\frac{\rho}{r_2}\right)\left(\frac{jk_1}{r_2}-\frac{1}{r_2^2}\right) \\
& +2e^{jk_1r_2}\left(\frac{\rho}{r_2}\right)\left\{\frac{k_1}{k_2}\left(\frac{z+d}{r_2}\right)\left(\frac{jk_1}{r_2}-\frac{3}{r_2^2}-\frac{3j}{k_1r_2^3}\right)\right. \\
& -\frac{k_1^2}{k_2^2}\left[\frac{1}{r_2^2}+\frac{3j}{k_1r_2^3}-\frac{3}{k_1^2r_2^4}\right. \\
& \left.\left.\left.+\left(\frac{z+d}{r_2}\right)^2\left(\frac{jk_1}{r_2}-\frac{6}{r_2^2}-\frac{15j}{k_1r_2^3}\right)\right]\right\}\right),
\end{aligned}
\tag{3.15}
$$

where

$$
P \;=\; S\left(\frac{S+Z+D}{R}\right)^2, \tag{3.16}
$$

with

$$
S \;=\; \frac{k_1^3r_2}{2k_2^2}; \qquad R \;=\; \frac{k_1^3\rho}{2k_2^2}; \qquad Z \;=\; \frac{k_1^2z}{2k_2}; \qquad D \;=\; \frac{k_1^2d}{2k_2}. \tag{3.17}
$$

And,

$$
F(P) \;=\; \frac{1}{2}(1+j)-\int_0^P \frac{e^{jt}}{(2\pi t)^{1/2}}\,dt, \tag{3.18}
$$

where the integral in the right hand side of Equation (3.18) is the *Fresnel integral* [48].

r_1 and r_2 are respectively the distances from the element of current and the perfect-image element to the point of observation; that is:

$$
r_1 \;=\; [(x-x')^2+(y-y')^2+(z-z')^2]^{1/2}, \tag{3.19}
$$

$$r_2 = [(x-x')^2 + (y-y')^2 + (z+z')^2]^{1/2}. \quad (3.20)$$

The accuracy of representation increases as the value of $|k_2/k_1|$ grows larger. The derived equations give the complete electric and magnetic fields subject to the inequality $|k_2/k_1| \gg 1$ or $|k_2| \geq 3k_1$ [17]-[19].

3.3 Complex Image Theory

As mentioned earlier, the expressions of the traditional solution to the classic problem of field computation for an infinitesimal dipole radiating above a finitely-conductive plane, consist of integrals of the Sommerfeld-type [2]. These expressions cannot be evaluated in closed form, and due to their highly oscillatory nature are difficult to evaluate numerically [36]. A method known as complex image theory [12]-[15] is used to derive explicit electromagnetic field expressions for dipoles of arbitrary orientation above lossy surfaces. It has been shown that the formulation for a horizontal dipole contains an image in the complex plane resulting in a diverging exponential term which is contribution of the image [15]. Comparison of numerical results from complex image theory and the original Sommerefld-type expressions shows good agreement as well as a speedup in computation time of many orders of magnitude [45].

The total field in the half-space of the original source can be calculated as the sum of the fields from the original and image sources in the homogeneous space. Image theory is best known for the case of a perfectly electrically conducting plane, in which the image of a dipole is another dipole [3]. However, if the reflection medium is not a perfectly-conductive surface, the image of a point source will be a line source in the complex plane. The form of the line source is given by the complex image theory [12].

The physical basis of complex image theory is to replace the finitely-conductive earth by a perfectly-conductive plane located at the complex depth $d/2$, where $d = 2/\gamma_2$ and $\gamma_2 = [j\omega\mu_0(\sigma_2 + j\omega\epsilon_2)]^{1/2}$ is the propagation constant in the earth. Analytically, this corresponds to replacing the *Fresnel reflection coefficient*, $(u_2 - \lambda)/(u_2 + \lambda)$, encountered in Sommerfeld integrals, by $\exp(-\lambda d)$, where λ is the variable of integration [11].

For low frequencies and measurement distances much less than a free-space wavelength, it is permissible to neglect the displacement currents both in the air and in the ground. The displacement current in the ground becomes more important at higher frequencies [12] and [45].

The major disadvantage of the complex image theory is that it has mainly been applied in the quasi-static range [15], [43], and [49]. More recently, it has been shown that the use of complex image theory can be extended to any range to obtain new formulas for the electric and magnetic fields produced by the four elementary dipole antennas, Horizontal Electric Dipole (HED), Horizontal Magnetic Dipole (HMD), Vertical Electric Dipole (VED), and Vertical Magnetic Dipole (VMD), for the air-air, air-surface, surface-air, and surface-surface propagation cases [11]-[14], and [45]. The only restriction on the use of this technique is that it requires $|n^2| \geq 10$, where $n = \gamma_2/\gamma_1$ [13].

The main reason for using the concept of an image is that it provides a simple picture that enables one to write the total field above a conductor immediately without resorting to the necessity of solving the appropriate differential equations. In addition, in contrast to the integral terms resulting from full analytical solution, the expressions obtained using the image method are relatively simple.

3.3.1 Finding the Finitely-conductive Earth Image Depth

Several methods are available for deriving the depth of a perfectly-conductive plane that can be used to replace the finitely-conductive ground. The most general method is equating the wave impedance, Z, at the surface ($z = 0$) for the two cases shown in Figure 3.2 [12] and [13].

For case A, in transverse electric (TE) propagation,

$$Z_A = \frac{\eta_2}{\sqrt{1-\gamma_1^2/\gamma_2^2}}, \tag{3.21}$$

where $\gamma_1^2 = -\omega^2\mu_0\epsilon_0$, $\gamma_2^2 = j\omega\mu_0(\sigma_2 + j\omega\epsilon_2)$, and $\eta_2 = \left(\frac{j\omega\mu_0}{\sigma_2+j\omega\epsilon_2}\right)^{1/2}$ [12] and [13].

For case B, we can write

$$Z_B \approx \eta_1 \tanh(\gamma_0 z_1), \tag{3.22}$$

where $\eta_1 = \sqrt{\mu_0/\epsilon_0} \approx 120\pi$ [12] and [13].

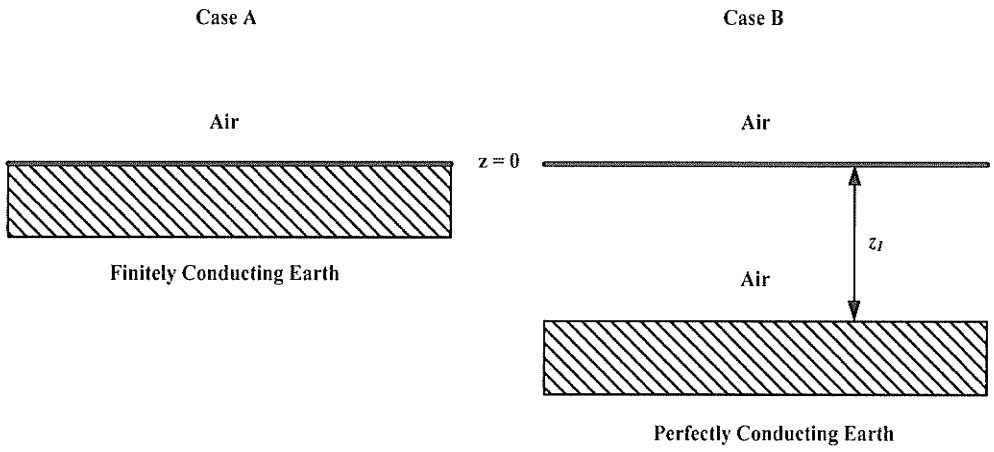

Figure 3.2. Replacing the finitely-conductive ground with PEC ground, located at the complex depth z_1.

For small values of $\gamma_1 z_1$, $\tanh(\gamma_1 z_1) \approx \gamma_1 z_1$, and

$$Z_B \approx \eta_1 \gamma_1 z_1 = j\omega\mu_0 z_1. \tag{3.23}$$

Equating the two impedances results in

$$z_1 \approx \frac{1}{\gamma_2\sqrt{1-\gamma_1^2/\gamma_2^2}} = \frac{1}{\sqrt{\gamma_2^2-\gamma_1^2}}. \tag{3.24}$$

Since the image depth is equal to $2z_1$, for TE propagation, the image depth d_{TE} for a wire on the surface of a finitely-conductive earth can be expressed as [12] and [13],

$$d_{TE} \approx \frac{2}{\sqrt{\gamma_2^2-\gamma_1^2}} = \frac{2/\gamma_2}{\sqrt{1-1/n^2}}, \tag{3.25}$$

subject to the condition that $\left|\sqrt{n^2-1}\right| \geq 2$.

Similarly, for transverse magnetic (TM) propagation, since

$$Z_A = \eta_1\sqrt{1-\gamma_1^2/\gamma_2^2}, \tag{3.26}$$

then,

$$d_{TM} \approx \frac{2}{\gamma_2}\sqrt{1-\gamma_1^2/\gamma_2^2} = \frac{2}{\gamma_2}\sqrt{1-1/n^2}, \tag{3.27}$$

subject to the condition that $\left|\sqrt{n^2-1}\right| \geq 2$ [12] and [13].

If $|n^2| > 10$, Equations (3.25) and (3.27) reduce to

$$d \approx d_{TE} \approx d_{TM} \approx 2/\gamma_2. \tag{3.28}$$

Another way to determine the image depth is to compare the results obtained from the image theory with the known analytical results. For $z = h = 0$, the HED Hertz vector is exactly equal to

$$\Pi_x = \frac{2IL}{4\pi\rho^3(j\omega\epsilon_0)(\gamma_2^2-\gamma_1^2)}[(1+\gamma_1\rho)e^{-\gamma_1\rho}-(1+\gamma_2\rho)e^{-\gamma_2\rho}], \tag{3.29}$$

while the image-theory result is [12] and [13],

$$\Pi_x \approx \frac{IL}{4\pi(j\omega\epsilon_0)}\left[\frac{e^{-\gamma_1\rho}}{\rho}-\frac{e^{-\gamma_1\rho_i}}{\rho_i}\right], \tag{3.30}$$

where $\rho_i = (\rho^2+d_{TE}^2)^{1/2}$.

When $\mathrm{Re}(\gamma_1\rho) \gg 1$, Equation (3.29) reduces to

$$\Pi_x \approx \frac{IL}{4\pi(j\omega\epsilon_0)}\left(\frac{2}{\gamma_2^2-\gamma_1^2}\right)(1+\gamma_1\rho)e^{-\gamma_1\rho}, \tag{3.31}$$

while Equation (3.30) becomes,

$$\Pi_x \approx \frac{IL}{4\pi(j\omega\epsilon_0)\rho^3}\left(\frac{d_{TE}^2}{2}\right)(1+\gamma_1\rho)e^{-\gamma_1\rho}. \tag{3.32}$$

Equating (3.31) and (3.32) results in

$$d_{TE} \approx \frac{2}{\sqrt{\gamma_2^2-\gamma_1^2}}, \tag{3.33}$$

which is identical to Equation (3.25) [12] and [13].

Solution proposed by Wait and Spies [47] suggests that another way to determine the image depth is to expand the function $f(u_1) = e^{u_1 d}\left(\frac{u_2-u_1}{u_1+u_2}\right)$ in a Taylor series about $u_1 = 0$, resulting in

$$\frac{u_2-u_1}{u_1+u_2} \approx e^{-u_1 d}\left[1+\frac{1}{3}\left(\frac{u_1 d}{2}\right)^3+\cdots\right], \tag{3.34}$$

where d is given by Equation (3.28) [12] and [13].

Introduction of the Taylor series in the exact equation yields an image at a distance $h + d$ from the ground plane [12], [13], and [47]. Higher order terms represent multi-poles at the same distance [50] and [51]. Usually the effect of such terms may be neglected due to their small values. It should also be pointed out that a high accuracy is unwarrantable for many applications due to the uncertain value of the earth's conductivity [13] and [50].

Detailed schematic of the horizontal dipole, the ideal and complex image, the complex depth, and the observation point are presented in Figure 3.3 [11]-[14].

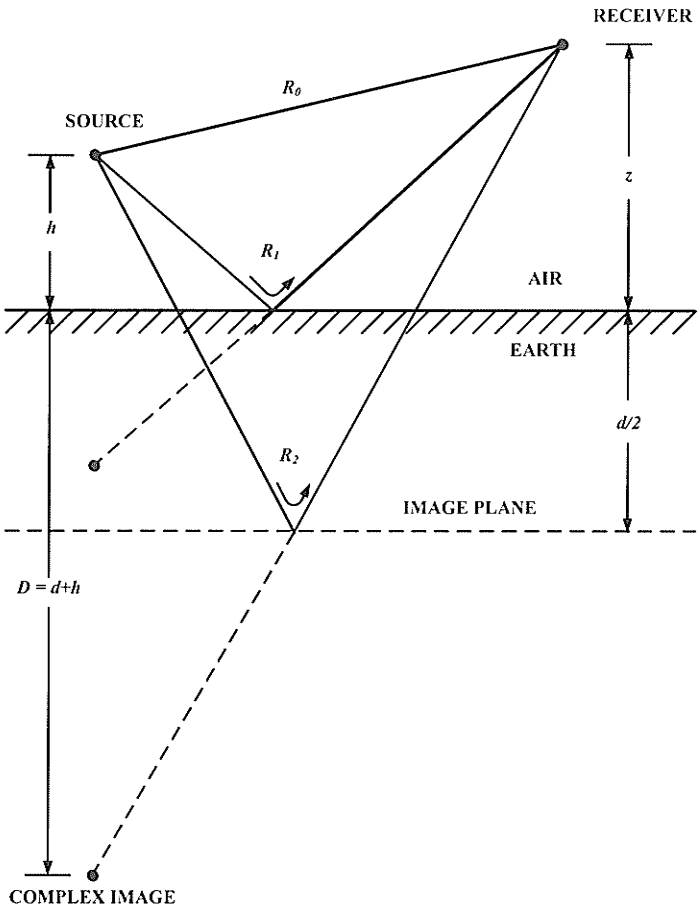

Figure 3.3. Geometry of the complex image theory for an infinitesimal dipole.

3.3.2 Solving Sommerfeld's Integrals Using Complex Image Theory

Complex image theory was employed because the integrals encountered in the exact solution could not be generally expressed conveniently in closed form [15].

For the semi-infinite conducting medium situation where both the source and receiving antenna are located above the earth's surface, the Sommerfeld integrals to be evaluated are of the type

$$I = \int_0^\infty \left(\frac{u_2 - \lambda}{u_2 + \lambda}\right) e^{-\lambda(z+h)} J_0(\lambda\rho) d\lambda, \tag{3.35}$$

where,

$$\gamma_1 = j\omega(\mu_0\epsilon_0)^{1/2}, \tag{3.36}$$

$$\gamma_2 = [j\omega\mu_0(\sigma_2 + j\omega\epsilon_2)]^{1/2}, \tag{3.37}$$

$$u_2 = (\lambda^2 + \gamma_2^2)^{1/2}, \tag{3.38}$$

and $J_0(\lambda\rho)$ is the Bessel function of the first kind, order zero, and argument $\lambda\rho$ [15].

Complex image theory is based upon approximating the Fresnel reflection coefficient, $(u_2 - \lambda)/(u_2 + \lambda)$, by a suitable exponential function [11]-[15], and [47]. For an HED source, when h and z are ≥ 0, the Sommerfeld integral expressions for the HED Hertz vector [11] are,

$$\Pi_x = \frac{IL}{4\pi(j\omega\epsilon_0)}\left[\frac{e^{-\gamma_1 R_0}}{R_0} - \frac{e^{-\gamma_1 R_1}}{R_1} + 2\int_0^\infty \frac{e^{-u_1(z+h)}}{u_1 + u_2} J_0(\lambda\rho)\lambda d\lambda\right], \tag{3.39}$$

and,

$$\Pi_z = \left(\frac{IL\cos\phi}{4\pi j\omega\epsilon_0}\right)\frac{\partial}{\partial\rho}\int_0^\infty \frac{2(u_2-u_1)}{\gamma_2^2 u_1+\gamma_1^2 u_2}e^{-u_1(z+h)}J_0(\lambda\rho)\lambda d\lambda, \tag{3.40}$$

where,

$$R_0 = [\rho^2+(z-h)^2]^{1/2}, \tag{3.41}$$

$$R_1 = [\rho^2+(z+h)^2]^{1/2}, \tag{3.42}$$

$$u_1 = (\lambda^2+\gamma_1^2)^{1/2}. \tag{3.43}$$

The real part of u_1, u_2, and γ_2 are all positive and a time harmonic dependence of $\exp(j\omega t)$ is assumed.

From Equations (3.39) and (3.40) and utilizing the identity $(u_2-u_1)(u_2+u_1) = \gamma_2^2-\gamma_1^2$ [11] and [14], we have

$$\begin{aligned}\nabla.\boldsymbol{\Pi} \approx \left(\frac{IL\cos\phi}{4\pi j\omega\epsilon_0}\right)\frac{\partial}{\partial\rho}\Bigg[&\frac{e^{-\gamma_1 R_0}}{R_0}-\frac{e^{-\gamma_1 R_1}}{R_1}\\ &+\int_0^\infty \frac{2\gamma_1^2 e^{-u_1(z+h)}}{\gamma_2^2 u_1+\gamma_1^2 u_2}J_0(\lambda\rho)\lambda d\lambda\Bigg].\end{aligned} \tag{3.44}$$

Following the procedure thoroughly reviewed in Appendix B, the approximate expressions for the components of Hertz potential vector are derived as [11],

$$\Pi_x \approx \frac{IL}{4\pi(j\omega\epsilon_0)}\left(\frac{e^{-\gamma_1 R_0}}{R_0}-\frac{e^{-\gamma_1 R_2}}{R_2}\right), \tag{3.45}$$

$$\begin{aligned}\Pi_z \approx -\frac{IL\cos\phi}{4\pi(j\omega\epsilon_0)\rho}\,[&\sin\psi_2\, e^{-\gamma_1 R_2}-\sin\psi_1\, e^{-\gamma_1 R_1}\\ &+\gamma_1 d e^{-\gamma_1 R_1}(\sin^2\psi_1+A\cos^2\psi_1)],\end{aligned} \tag{3.46}$$

$$\nabla.\boldsymbol{\Pi} \approx -\frac{IL\cos\phi}{4\pi(j\omega\epsilon_0)}\left[(1+\gamma_1 R_0)\cos\psi_0\frac{e^{-\gamma_1 R_0}}{R_0^2}\right.$$
$$-(1+\gamma_1 R_1)\cos\psi_1\frac{e^{-\gamma_1 R_1}}{R_1^2} \quad (3.47)$$
$$\left.+\frac{2\cos\psi_1\, e^{-\gamma_1 R_1}}{n^2 R_1^2}(1+\gamma_1 R_1 A)\right],$$

After deriving the expressions for the HED Hertz vector, the electric and magnetic fields in the air can be obtained from

$$\mathbf{E} = -\gamma_1^2\boldsymbol{\Pi} + \nabla(\nabla.\boldsymbol{\Pi}), \quad (3.48)$$

and,

$$\mathbf{H} = j\omega\epsilon_0(\nabla\times\boldsymbol{\Pi}), \quad (3.49)$$

as [11],

$$E_\rho = \frac{IL\cos\phi}{4\pi(j\omega\epsilon_0)}\left[\{(3\cos^2\psi_0-1)(1+\gamma_1 R_0)-\gamma_1^2 R_0^2\sin^2\psi_0\}\frac{e^{-\gamma_1 R_0}}{R_0^3}\right.$$
$$-\{(3\cos^2\psi_1-1)(1+\gamma_1 R_1)-\Gamma_{||}\gamma_1^2 R_1^2\sin^2\psi_1\}\frac{e^{-\gamma_1 R_1}}{R_1^2}$$
$$+\frac{2\,e^{-\gamma_1 R_1}}{n^2 R_1^3}\left\{[(3\cos^2\psi_1-1)(1+\gamma_1 R_1)] \quad (3.50)\right.$$
$$-\frac{2R_1^2}{d^2}\left[1-\frac{R_1}{R_2}\,e^{-\gamma_1(R_2-R_1)}\right]$$
$$\left.\left.+\,n^2\gamma_1^2 R_1^2\left[\sin\psi_1+\left(\frac{1-\Gamma_{||}}{2}\right)F(w)\Delta\right]\right\}\right],$$

$$E_\phi = \frac{IL\sin\phi}{4\pi(j\omega\epsilon_0)}\left[(1+\gamma_1 R_0+\gamma_1^2 R_0^2)\frac{e^{-\gamma_1 R_0}}{R_0^3}\right.$$
$$-(1+\gamma_1 R_1+\gamma_1^2 R_1^2)\frac{e^{-\gamma_1 R_1}}{R_1^3} \tag{3.51}$$
$$\left.+\frac{2e^{-\gamma_1 R_1}}{n^2 R_1^3}\left\{(1+\gamma_1 R_1 A)+\frac{2R_1^2}{d^2}\left[1-\frac{R_1}{R_2}e^{-\gamma_1(R_2-R_1)}\right]\right\}\right],$$

$$E_z = \frac{IL\cos\phi}{4\pi(j\omega\epsilon_0)}\left\{(3+3\gamma_1 R_0+\gamma_1^2 R_0^2)\sin\psi_0\cos\psi_0\frac{e^{-\gamma_1 R_0}}{R_0^3}\right.$$
$$-\left(3+3\,\gamma_1 R_1+\Gamma_{||}\gamma_1^2 R_1^2\right)\sin\psi_1\cos\psi_1\frac{e^{-\gamma_1 R_1}}{R_1^3}$$
$$+\frac{2}{n^2}(3+3\gamma_1 R_1+\gamma_1^2 R_1^2)\sin\psi_1\cos\psi_1\frac{e^{-\gamma_1 R_1}}{R_1^3} \tag{3.52}$$
$$-\gamma_1^2\left[\frac{\cos\psi_2\, e^{-\gamma_1 R_2}}{R_2+d+z+h}-\frac{\cos\psi_1\, e^{-\gamma_1 R_1}}{R_1+z+h}(1+\gamma_1 d)\right]$$
$$\left.-2\Delta\left[1-\left(\frac{1-\Gamma_{||}}{2}\right)F(w)\right]\cos\psi_1\,(\gamma_1^2 R_1^2)\frac{e^{-\gamma_1 R_1}}{R_1^3}\right\};$$

$$H_\rho = \frac{IL\sin\phi}{4\pi}\left[(1+\gamma_1 R_2)\sin\psi_2\frac{e^{-\gamma_1 R_2}}{R_2^2}-(1+\gamma_1 R_0)\sin\psi_0\frac{e^{-\gamma_1 R_0}}{R_0^2}\right.$$
$$\left.-\frac{e^{-\gamma_1 R_2}}{R_2(R_2+d+z+h)}+\frac{(1+\gamma_1 dA)e^{-\gamma_1 R_1}}{R_1(R_1+z+h)}\right], \tag{3.53}$$

$$H_\phi = -\frac{IL\cos\phi}{4\pi}\left[(1+\gamma_1 R_0)\sin\psi_0\frac{e^{-\gamma_1 R_0}}{R_0^2}\right.$$
$$-\left(1+\Gamma_{||}\,\gamma_1 R_1\right)\sin\psi_1\frac{e^{-\gamma_1 R_1}}{R_1^2}$$
$$+\frac{\gamma_1^2 d}{R_1}\left(\frac{1-\Gamma_{||}}{2}\right)F(w)e^{-\gamma_1 R_1}-\frac{e^{-\gamma_1 R_2}}{R_2(R_2+d+z+h)}$$
$$\left.+\frac{(1+\gamma_1\,d)e^{-\gamma_1 R_1}}{R_1(R_1+z+h)}\right], \tag{3.54}$$

$$H_z = \frac{IL\sin\phi}{4\pi}\left[(1+\gamma_1 R_0)\cos\psi_0\frac{e^{-\gamma_1 R_0}}{R_0^2}-(1+\gamma_1 R_2)\cos\psi_2\frac{e^{-\gamma_1 R_2}}{R_2^2}\right], \tag{3.55}$$

where,

$$R_2 = [\rho^2+(d+z+h)^2]^{1/2}, \tag{3.56}$$

$$\begin{cases}\sin\psi_0 = (z-h)/R_0\\ \cos\psi_0 = \rho/R_0\end{cases}, \tag{3.57}$$

$$\begin{cases}\sin\psi_1 = (z+h)/R_1\\ \cos\psi_1 = \rho/R_1\end{cases}, \tag{3.58}$$

$$\begin{cases}\sin\psi_2 = (d+z+h)/R_2\\ \cos\psi_2 = \rho/R_2\end{cases}, \tag{3.59}$$

$$\Delta = 1/n, \tag{3.60}$$

$$\Gamma_{||} = \frac{\sin\psi_1-\Delta}{\sin\psi_1+\Delta}, \tag{3.61}$$

$$w = -\frac{\gamma_0 R_1}{2}(\sin\psi_1+\Delta)^2, \tag{3.62}$$

$$F(w) = 1 - j(\pi w)^{1/2} e^{-w} \operatorname{erfc}\left(jw^{1/2}\right), \tag{3.63}$$

$$A = 1 - \left(\frac{1 - \Gamma_{\parallel}}{2}\right)[1 - F(w)]. \tag{3.64}$$

The results can easily be extended to the case of a multilayered earth, simply by letting $d = (2/\gamma_2)Q$, where Q is the *plane-wave correction factor* employed to account for the presence of stratification in the earth [11], [13], and [15]. The obtained expressions are valid from the quasi-static to far-field ranges as long as $|n^2| > 10$. The quasi-static and quasi-near ranges are those for which $|\gamma_1 \rho| \ll 1$ and $|\gamma_1 \rho| \ll 1 \ll |\gamma_2 \rho|$ [49].

It should be noted that when the ratio of σ_1 to $\omega\epsilon_1$ is of the order of (or less than) unity, the image theory results start to deviate from the exact Sommerfeld integration results [12] and [45]. In that case, the image solution is an asymptotic solution in the sense that it requires a source-receiver separation large enough that the ignored fields are negligible. One way to improve the accuracy is to add the first correction term, correspondent to the multi-pole image located at the same depth as the single image [50] and [51]. However, in applications regarding power system transients, the restricting condition for validity of complex image theory is always satisfied.

The obtained formulas can be used to determine the effects of the ground loss on the ground wave field intensity in the neighbourhood of a dipole. These formulas may also be used to show the influence of the dipole location on the attenuation of different ranges of frequencies. Equations derived in this section, are valid for infinitesimal dipoles; however, they are also true for finite dipoles if the length of the dipole is much less than a free-space wavelength and the measurement distance [11].

It should be noted that the two media can be inverted and the air may be replaced by the earth's crust (of conductivity σ_2 and dielectric constant ϵ_2) [13]. The same equations can be utilized as long as $|n_2^2| = |\gamma_1^2/\gamma_2^2| \geq 10$ simply by replacing $j\omega\epsilon_0$ by $\sigma_2 + j\omega\epsilon_2$.

Although displacement currents were ignored in most of these analyses, they can be included simply by replacing σ_1 with $\sigma_1 + j\omega\epsilon_1$ (as long as $|n|^2 \gg 1$) [13].

3.4 Fields Generated by a Vertical Dipole over Finitely-Conducive Earth

As mentioned in Chapter 2, to take the effect of the conductor sag into account, we can decompose each segment of the transmission line into horizontal and vertical vectors. Therefore, to obtain the total EM radiation from a sagged conductor, we need to determine the fields associated with a vertical electric dipole.

Many approximate expressions are available for the electromagnetic fields generated by vertical dipoles over the finitely-conductive ground [11], [16], [39]-[41], [43], [46], and [49]. In this section, we consider the solution proposed by Bannsiter based on complex image theory [11], [12], and [45]. The obtained expressions have been compared with the exact integrations of Sommerfeld integral by Zeddam [52]. The results show that the equations derived by applying complex image theory can be used to calculate the EM fields with an accuracy of higher than 95%.

Let us consider the geometry shown in Figure 3.4. The dipole is at height h from the ground level and the current in the dipole is directed in the direction of z-axis. Following the same procedure described in section 3.3.2, the electromagnetic field components at point P are given by [11],

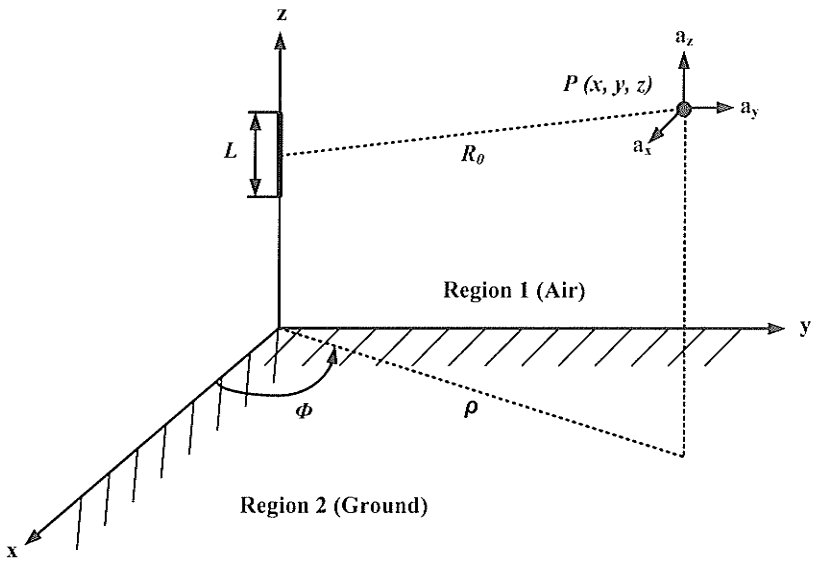

Figure 3.4. Geometry of a vertical dipole, located on the z-axis above finitely-conductive ground.

$$
\begin{aligned}
E_\rho \;=\; & \frac{IL\cos\phi}{4\pi(j\omega\epsilon_0)}\Bigg\{(3+3\gamma_1R_0+\gamma_1^2R_0^2)\sin\psi_0\cos\psi_0\frac{e^{-\gamma_1R_0}}{R_0^3} \\
& +\left(3+3\gamma_1R_1+\Gamma_{||}\gamma_1^2R_1^2\right)\sin\psi_1\cos\psi_1\frac{e^{-\gamma_1R_1}}{R_1^3} \\
& -\frac{2}{n^2}(3+3\gamma_1R_1+\gamma_1^2R_1^2)\sin\psi_1\cos\psi_1\frac{e^{-\gamma_1R_1}}{R_1^3} \\
& +\gamma_1^2\left[\frac{\cos\psi_2\,e^{-\gamma_1R_2}}{R_2+d+z+h}-\frac{\cos\psi_1\,e^{-\gamma_1R_1}}{R_1+z+h}(1+\gamma_1 d)\right] \\
& -2\Delta\left[1-\left(\frac{1-\Gamma_{||}}{2}\right)F(w)\right]\cos\psi_1\,(\gamma_1^2R_1^2)\frac{e^{-\gamma_1R_1}}{R_1^3}\Bigg\},
\end{aligned}
\tag{3.65}
$$

$$
E_\phi \;=\; 0, \tag{3.66}
$$

$$E_z = -\frac{IL\cos\phi}{4\pi(j\omega\epsilon_0)}\Bigg[\{(1-3\sin^2\psi_0)\,(1+\gamma_1 R_0) + \gamma_1^2 R_0^2\cos^2\psi_0\}\frac{e^{-\gamma_1 R_0}}{R_0^3} + \{(1-3\sin^2\psi_1)(1+\gamma_1 R_1) + \Gamma_{||}\gamma_1^2 R_1^2\cos^2\psi_1\}\frac{e^{-\gamma_1 R_1}}{R_1^3} + (1-\Gamma_{||})F(w)\cos^2\psi_1\,(\gamma_1^2 R_1^2)\frac{e^{-\gamma_1 R_1}}{R_1^3}\Bigg]; \tag{3.67}$$

$$H_\rho = 0, \tag{3.68}$$

$$H_\phi = \frac{IL}{4\pi}\Bigg[(1+\gamma_1 R_0)\cos\psi_0\frac{e^{-\gamma_1 R_0}}{R_0^2} + \left(1+\Gamma_{||}\gamma_1 R_1\right)\cos\psi_1\frac{e^{-\gamma_1 R_1}}{R_1^2} + \left(1-\Gamma_{||}\right)F(w)\cos\psi_1\,(\gamma_1 R_1)\frac{e^{-\gamma_1 R_1}}{R_1^2}\Bigg], \tag{3.69}$$

$$H_z = 0. \tag{3.70}$$

3.5 DC Component of the Electric and Magnetic Fields

Neither of the two frequency-domain methods reviewed in this chapter provides an accurate value for the DC component of the electric and magnetic fields. Since the power transient waveforms carry a zero-frequency component, we have to come up with an analytical approach to deal with this problem.

In this thesis, to overcome this problem, use is made of the approximate formulas suggested by Olsen [20] and [21]. Olsen has employed the image theory in the quasi-static ranges to find the expressions for the extremely-low frequency (ELF) electric and magnetic fields, including the zero-frequency field component. The obtained formulas are

valid when the distance from the observation point is much less than the wavelength. The components of the DC electric and magnetic fields at any point (x, y, z) due to a line extended along the x-axis, are obtained using Equations (3.71)-(3.74). The line is located at $(y, z) = (0, h)$, with the schematic shown in Figure 3.5 [20] and [21].

$$E_y = -\frac{V}{\ln(2h/a)}\left[\frac{y}{(z+h)^2+y^2} - \frac{y}{(z-h)^2+y^2}\right], \tag{3.71}$$

$$E_z = -\frac{V}{\ln(2h/a)}\left[\frac{z+h}{(z+h)^2+y^2} - \frac{z-h}{(z-h)^2+y^2}\right], \tag{3.72}$$

$$B_y = -2I\left[\frac{z-h}{(z-h)^2+y^2}\right], \tag{3.73}$$

$$B_z = 2I\left[\frac{y}{(z-h)^2+y^2}\right], \tag{3.74}$$

where V and I are the voltage and current on the wire, and a is the radius of the wire.

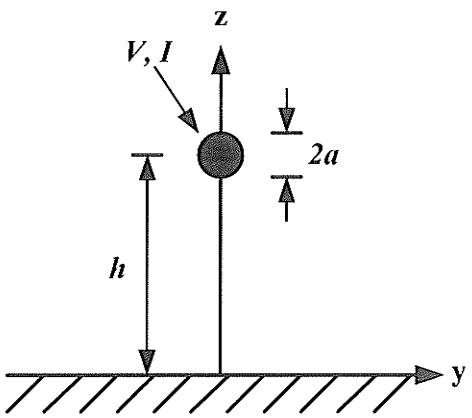

Figure 3.5. Cross-sectional view of an overhead transmission line.

Chapter 4

Reduced-Scale Modeling

4.1 Introduction

Scale modeling of power system equipment has been a popular tool to analyze the behaviour of the system in the steady-state or transient modes. Downscaled models have been employed in studies concerning transmission lines [53] and [54], electric fields in substations and distribution networks [29], corona effects [55]-[59], and lightning transients [28], and [60]-[62]. Recently, numerical techniques and software packages have replaced the role of scale modeling. Nevertheless, the limitations on applicability of such numerical codes and numerous parameters affecting the system's response make it impossible to fully trust the results derived using any software package. Thus, scale modeling still maintains a certain validity to verify the theoretical and numerical studies [29].

Some of the advantages of the reduced-scale modeling are [58] and [59]:

- It is cheaper and easier to do measurements on the reduced-scale systems.
- It collects a large amount of test data in a short period of time.

- Analytical formulas can be examined easily.
- Geometric and operating conditions can easily be tested.
- The effect of different quantities on the behaviour of the system can be independently studied.
- Scale modeling enforces us to work with higher frequencies in which calibrated equipment are cheaper and more common than equipment calibrated for low frequencies.

The objective of this chapter is to show how the measurements from a scaled model can offer a preview on the behaviour of the full-scale system.

4.2 Similarity Theory

The basic concept of reduced-scale modeling is that an energized current-carrying conductor produces an electromagnetic field, the magnitude and extent of which depend on the geometry of the energized conductors and surrounding ground potential objects [58] and [59]. The reduced-scale model should represent the full-scale system realistically for the electromagnetic field measurement purposes.

In any recued-scale model, one or more physical quantities have to be reduced in order to carry out the experiment. For the experimental results to be of use in determining the condition in a real situation, some scaling factors for all the parameters need to be applied in order that the results derived from the model are physically similar to those in the full-scale system. Further, an appropriate transformation algorithm shall be used to convert the model results into the original case [27].

Similarity theory [27] suggests that a geometric similarity between two bodies exists if all of their homologous lengths are in the same relation to each other. In another word, for two systems to be geometrically similar, the following relation must be fulfilled:

$$\frac{l_O}{l_M} = f_l \tag{4.1}$$

The length in the original system is l_O, and l_M is the corresponding length in the model. f_l is the geometrical similarity constant [27]. The common expression *scale factor* is used in this thesis for the similarity constant.

According to the similarity theory, the response of the system to an excitation input may be found by scaling the response of a geometrically similar system to an appropriately scaled input, without any need to solve the governing differential equations [27]-[29], [60], and [61].

4.3 Electromagnetic Differential Equations for the Downscaled Model

As mentioned earlier, the similarity theory allows the derivation of scale laws from the differential equations describing a physical process, without having to solve them. Due to the linearity of Maxwell's equations, scale laws for different parameters encountered in these differential equations can be obtained using the similarity theory.

Considering Maxwell's equations,

$$\nabla \times \mathbf{H} = \sigma \mathbf{E} + \epsilon \frac{\partial \mathbf{E}}{\partial t}, \tag{4.2}$$

and,

$$\nabla \times \mathbf{E} = -\mu \frac{\partial \mathbf{H}}{\partial t}, \tag{4.3}$$

in a given medium with conductivity (σ), permittivity (ϵ), and permeability (μ), the scale factors for length (p), time (γ), electric field (α), and magnetic field (β) can be defined as [29],

$$p = \frac{x_m}{x} = \frac{y_m}{y} = \frac{z_m}{z}, \tag{4.4}$$

$$\gamma = \frac{t_m}{t}, \tag{4.5}$$

$$\alpha = \frac{E_m}{E}, \tag{4.6}$$

$$\beta = \frac{H_m}{H}. \tag{4.7}$$

where x, y, and z refer to the coordinate system, t represents the time, and subscript m refers to the scale model variables. In the scaled model, the fields are described by

$$\nabla_{\mathbf{m}} \times \mathbf{H}_{\mathbf{m}} = \sigma_m \mathbf{E}_{\mathbf{m}} + \epsilon_m \frac{\partial \mathbf{E}_{\mathbf{m}}}{\partial t_m}, \tag{4.8}$$

and,

$$\nabla_{\mathbf{m}} \times \mathbf{E}_{\mathbf{m}} = -\mu_m \frac{\partial \mathbf{H}_{\mathbf{m}}}{\partial t}, \tag{4.9}$$

with σ_m, ϵ_m, and μ_m representing the characteristics of the scaled model medium [29].

In the above equations, the symbol $\nabla_{\mathbf{m}}$ stands for differentiation with respect to the model coordinates. It can be shown that the scale factor for the curl operator is $1/p$ [29]; thus,

$$\nabla_{\mathbf{m}} \times \mathbf{H}_{\mathbf{m}} = \frac{1}{p}\nabla \times \mathbf{H}_{\mathbf{m}} = \frac{\beta}{p}\nabla \times \mathbf{H}, \tag{4.10}$$

and,

$$\nabla_{\mathbf{m}} \times \mathbf{E}_{\mathbf{m}} = \frac{\alpha}{p}\nabla \times \mathbf{E}. \tag{4.11}$$

Differentiating $\mathbf{E}_{\mathbf{m}}$ and $\mathbf{H}_{\mathbf{m}}$ with respect to time leads to,

$$\frac{\partial \mathbf{E}_{\mathbf{m}}}{\partial t_m} = \frac{\alpha}{\gamma}\frac{\partial \mathbf{E}}{\partial t}, \tag{4.12}$$

and,

$$\frac{\partial \mathbf{H}_{\mathbf{m}}}{\partial t_m} = \frac{\beta}{\gamma}\frac{\partial \mathbf{H}}{\partial t}. \tag{4.13}$$

Substituting (4.10)–(4.13) into (4.8) and (4.9) results in,

$$\frac{\beta}{p}\nabla \times \mathbf{H} = \sigma_m \alpha \mathbf{E} + \frac{\alpha}{\gamma}\epsilon_m \frac{\partial \mathbf{E}}{\partial t}, \tag{4.14}$$

and,

$$\frac{\alpha}{p}\nabla \times \mathbf{E} = -\mu_m \frac{\beta}{\gamma}\frac{\partial \mathbf{H}}{\partial t}. \tag{4.15}$$

In order to represent the real system by the scaled model correctly, (4.14), (4.15) and (4.2), (4.3) must be equivalent. Therefore [29],

$$\epsilon_m = \frac{\gamma\beta}{p\alpha}\epsilon, \tag{4.16}$$

$$\mu_m = \frac{\alpha\gamma}{p\beta}\mu, \tag{4.17}$$

$$\sigma_m = \frac{\beta}{p\alpha}\sigma. \tag{4.18}$$

From the above definitions, the scale factor of any electromagnetic quantity can be determined. If air is the medium in both systems, the following conditions must exist [29]:

$$\epsilon_m = \epsilon \quad \Rightarrow \quad \frac{\gamma\beta}{p\alpha} = 1, \tag{4.19}$$

$$\mu_m = \mu \quad \Rightarrow \quad \frac{\alpha\gamma}{p\beta} = 1. \tag{4.20}$$

Then,

$$\alpha = \beta, \tag{4.21}$$

$$\gamma = p, \tag{4.22}$$

$$\sigma_m = \sigma/p. \tag{4.23}$$

That is, the scale factor for conductivity must be the inverse of that for length. Clearly, this condition is not satisfied if the same medium is used for both real-size and scaled

systems. However, considering that air is a good insulator, the error resulting in not taking into account its conductivity can be neglected [29].

4.4 Scale Factors for Different Electromagnetic Parameters

To obtain a complete list of the scale factors for all the parameters that we come across in different EM problems, we consider following integral equations:

$$I = \oint_C \mathbf{H}.\,\boldsymbol{dl}, \tag{4.24}$$

and,

$$V = \int \mathbf{E}.\,\boldsymbol{dl}. \tag{4.25}$$

In the scaled model, current and voltage are described by,

$$I_m = \oint_C \mathbf{H_m}.\,\boldsymbol{dl_m} = \oint_C (\alpha\mathbf{H}).\,(p\boldsymbol{dl}) = (\alpha.p)\oint_C \mathbf{H}.\,\boldsymbol{dl} = (\alpha.p)I, \tag{4.26}$$

and,

$$V_m = \int \mathbf{E_m}.\,\boldsymbol{dl_m} = \int (\alpha\mathbf{E}).\,(p\boldsymbol{dl}) = (\alpha.p)\int \mathbf{E}.\,\boldsymbol{dl} = (\alpha.p)V. \tag{4.27}$$

According to the transmission line theory,

$$\frac{\partial}{\partial x}V(x,t) = -RI(x,t) - L\frac{\partial}{\partial t}I(x,t), \tag{4.28}$$

and,

$$\frac{\partial}{\partial x} I(x,t) = -GV(x,t) - C\frac{\partial}{\partial t} V(x,t), \tag{4.29}$$

where R, L, G, and C are the per unit length (p.u.l.) parameters of the line [63].

Equations (4.28) and (4.29) in the scaled model turn into:

$$\frac{\partial}{\partial x_m} V_m(x_m,t_m) = -R_m I_m(x_m,t_m) - L_m \frac{\partial}{\partial t_m} I_m(x_m,t_m), \tag{4.30}$$

and,

$$\frac{\partial}{\partial x_m} I_m(x_m,t_m) = -G_m V_m(x_m,t_m) - C_m \frac{\partial}{\partial t_m} V_m(x_m,t_m). \tag{4.31}$$

Substituting (4.26) and (4.27) into (4.30) and (4.31), yields

$$\left(\frac{\alpha.p}{p}\right)\frac{\partial}{\partial x} V(x,t) = -(\alpha.p)R_m I(x,t) - \left(\frac{\alpha.p}{p}\right) L_m \frac{\partial}{\partial t} I(x,t), \tag{4.32}$$

and,

$$\left(\frac{\alpha.p}{p}\right)\frac{\partial}{\partial x} I(x,t) = -(\alpha.p)G_m V(x,t) - \left(\frac{\alpha.p}{p}\right) C_m \frac{\partial}{\partial t} V(x,t). \tag{4.33}$$

In order to have a valid downscaled model, (4.32), (4.33) and (4.28), (4.29) must be equivalent. Therefore,

$$R_m = \frac{1}{p} R, \tag{4.34}$$

$$L_m = L, \tag{4.35}$$

$$G_m = \frac{1}{p} G, \tag{4.36}$$

$$C_m = C. \tag{4.37}$$

where R_m, L_m, G_m, and C_m are the per unit length (p.u.l.) parameters of the scaled line.

To obtain the effect of scaling on the EM response of any electrical system, the relationship between the parameters should be known. A brief list of familiar equations in the transient electromagnetic problems is given below [27]:

- Ampere's Law:

$$\oint_C \mathbf{H}.\boldsymbol{dl} = I + \frac{d}{dt}\int_A \mathbf{D}.\boldsymbol{dA}. \tag{4.38}$$

- Faraday's Law:

$$\oint_C \mathbf{E}.\boldsymbol{dl} = -\frac{d}{dt}\int_A \mathbf{B}.\boldsymbol{dA}. \tag{4.39}$$

- Current:

$$\int_A \mathbf{J_s}.\boldsymbol{dA} = I. \tag{4.40}$$

- Electric (Displacement) Flux:

$$\int_A \mathbf{D}.\boldsymbol{dA} = \psi. \tag{4.41}$$

- Magnetic (Induction) Flux:

$$\int_A \mathbf{B}.\boldsymbol{dA} = \phi. \tag{4.42}$$

- Current Density:

$$\mathbf{J_s} = \sigma \mathbf{E}. \tag{4.43}$$

- Electric Flux Density:

$$\mathbf{D} = \epsilon \mathbf{E}. \tag{4.44}$$

- Magnetic Flux Density:

$$\mathbf{B} = \mu \mathbf{H}. \tag{4.45}$$

- Ohm's Law:

$$V = RI. \tag{4.46}$$

- Voltage (Capacitive):

$$V = \frac{1}{C}\int Idt. \tag{4.47}$$

- Voltage (Inductive):

$$V = L\frac{dI}{dt}. \tag{4.48}$$

- Charge:

$$Q = CV. \tag{4.49}$$

- Magnetic Flux:

$$\phi = \frac{V}{R_m}. \tag{4.50}$$

- Intrinsic Parameters:

$$R = \frac{l}{\sigma A}, \tag{4.51}$$

$$C = \frac{\epsilon A}{l}, \tag{4.52}$$

$$R_m = \frac{l}{\mu A}. \tag{4.53}$$

Using Equations (4.21)-(4.23), (4.26), (4.27), and (4.34)-(4.53), and the choice of scale factors (p) for the geometrical dimensions and (α) for the field intensity magnitude, the scale factors for quantities of interest are derived and reported in Table 4.1 [27]-[29], [60], and [61].

The choice of geometrical scale factor, p, depends on the available area for the installation and also on the generation and measurement systems features. A very low scale factor allows for the simulation of longer lines and stroke channels in small laboratories. This procedure, however, implies the need of measuring systems with higher frequency bandwidths. On the other hand, the scale factor for the electric and magnetic field intensity, α, is defined considering the operational range of available field measurement equipment [29].

Table 4.1. Scale factors for electric and magnetic parameters.

Parameter	Scale Factor
Length (l)	p
Time (t)	p
Electric Field (E)	α
Magnetic Field (H)	α
Resistance (R)	1
Capacitance (C)	p
Inductance (L)	p
Impedance (Z)	1
Propagation Velocity (v)	1
Frequency (f)	$1/p$
Conductivity (σ)	$1/p$
Voltage (V)	$\alpha.p$
Current (I)	$\alpha.p$
Current Derivative (dI/dt)	α
Magnetic Field Derivative (dH/dt)	α
Current Density (J_s)	α/p
Electric Charge (Q)	$\alpha.p^2$
Electric Flux (ψ)	$\alpha.p^2$
Magnetic Flux (ϕ)	$\alpha.p^2$
Magnetic Resistance (R_m)	$1/p$

From the results of Table 4.1, we note that if p and α are known, the scale factors for all quantities of interest can be determined easily [29].

It can be observed that increasing the frequency demands the size of the system to be reduced by the same factor. It could however be hard to scale the conductivity of the material with the same factor since we have to find another material for the conductors and ground potential objects. Thus the attenuation of the current along the line can be hard to simulate in a realistic way [29].

Chapter 5

Results

5.1 Introduction

In Chapter 2, antenna theory was employed to analyze the electromagnetic fields associated with a transmission line when the line is located above PEC ground. In the proposed technique, the line was decomposed into a large number of small dipoles and exact analytical formulas associated with a horizontal Hertzian dipole were presented. The effect of the PEC ground was taken into consideration using the image theory.

To take the finite conductivity of the ground into account, two analytical approaches were reviewed in Chapter 3. The first approach, presented by King [16]-[19], solves the transformed form of Maxwell's equations under certain simplifying assumptions while the second method, proposed by Bannister [11]-[14], applies the complex image theory to the case of a horizontal electric dipole. In the latter approach, the well known Sommerfeld integrals [2] are solved using simplifying conditions, valid for a wide range of the frequency spectrum.

In this chapter, the simulation results of the three methods reviewed in Chapters 2 and 3 are presented and analyzed. A commercial simulation software package is used to verify the validity of the reviewed set of formulas. Afterwards, the relation between the electromagnetic field waveforms and the source-to-observation point distance is studied.

As stated earlier, the main drawback of the so-called dipole technique is the high time-consumption [31]-[33]. This is due to the fact that each constituent dipole should be small enough so that the current passing through it can be considered constant at any time. Further, for closeby observation points, we need a very short dipole so that the variation in the distance between different points along the dipole and the observation point is negligible. To analyze the effect of length of the dipoles on the final results, different dipole lengths are chosen. Variation of the results and the calculation time are then studied for different cases.

An algorithm for finding the radiation from a sagged conductor is proposed and the effect of sag on the electromagnetic radiation from the line is studied. Finally, the code implemented for finding the electromagnetic fields is merged with an FDTD code [23] and [24], which provides the current distribution along a transmission line excited by a known current or voltage waveforms. Using this combination, the electric and magnetic fields associated with an overhead power transmission line can be found with a very good precision as long as the excitation waveform is known.

5.2 Verification of the Results Using the Numerical Electromagnetic Code (NEC)

The idea of numerically calculating the electromagnetic fields associated with transients is not new. However, it has not been recognized as a popular practical method, partly because the verification of the accuracy of the results has been difficult [64]. In this chapter, a commercial numerical code is used as a comparison tool to verify the validity of the methods reviewed in Chapters 2 and 3.

Numerical Electromagnetic Code (NEC) [22] is a commercial computer program for analyzing the electromagnetic response of wire structures such as antennas and transmission lines. NEC is a frequency-domain computer code; therefore, to obtain the time-domain response of any system using NEC, Fourier and inverse Fourier transforms should be employed [64]-[66]. Time-domain excitation waveform needs to be transformed into the frequency-domain by FFT. The transformed input waveform multiplied by the NEC results is finally transformed back into the time-domain using inverse FFT. The flow of the solution is shown in Figure 5.1 [64] and [67].

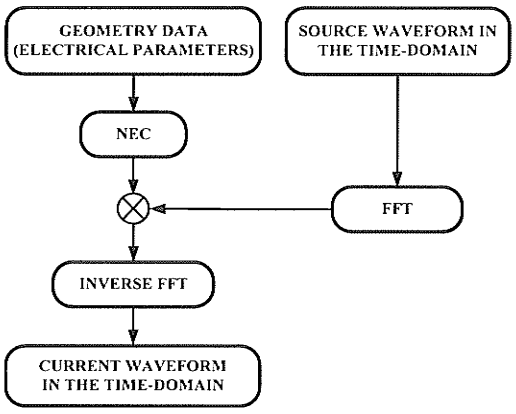

Figure 5.1. Tuning NEC for time-domain applications.

Careful considerations should be taken in determining the time step, Δt, and the duration of analysis, T, (or the highest and the lowest frequency in the analysis) in the Fourier transform of the input waveform. Therefore, frequencies of the frequency-domain excitation waveform are coincided with the frequencies analyzed by NEC [64].

In this chapter, numerical electromagnetic code is used as a verification tool for the applied methodology towards finding the radiation of an overhead transmission line. In the first step, the value of the electric field intensity is calculated for three distinct frequencies using King's formulation and complex image theory. The obtained results are compared with those derived from NEC. It can be seen that a very good agreement is observed among the three calculation methods [68] and [69]. However, as frequency increases, the results derived from NEC tend to deviate from those obtained from the two analytical methods.

The simulated line in this case is a 100-m-long overhead line extended along the x-axis with the height of 15 m, shown in Figure 5.2. The origin of the coordinate system is located in the middle of the line and the line is divided into 400 segments, each with the length of 25 cm. The radius of the conductor is set at 5 cm. Both ends of the line are left open-circuited and a uniform voltage source with the magnitude of 150 V is placed at the first segment. The magnitude of the electric field is calculated at ten different observation points (x = -10 m, -8 m, -6 m, -4 m, 0, 2 m, 4 m, 6 m, 8 m, y = 10 m, and z = 0) and for three distinct frequencies (f = 60 Hz, f = 1 kHz, and f = 1 MHz).

The magnitude of the electric and magnetic field intensity vectors at the selected observation points are calculated using King's formulation, complex image theory, and

NEC. Three distinct excitation frequencies are chosen such that the results of the aforementioned methods can be compared in the low-, intermediate-, and high-frequencies. The results are shown in Figures 5.3-5.5.

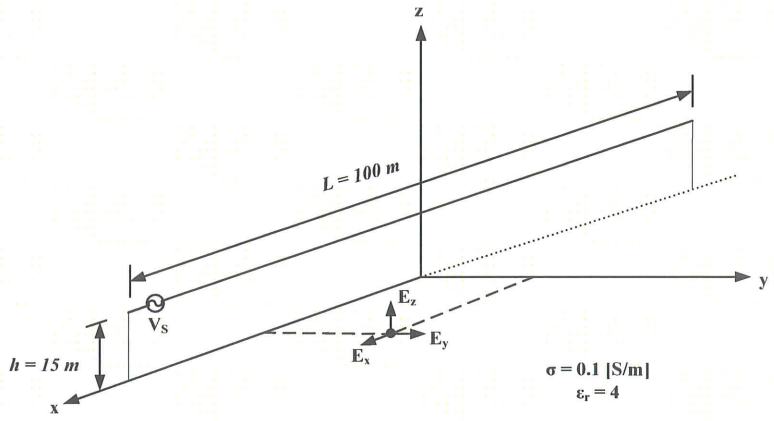

Figure 5.2. The geometry of a transmission line extended along the *x*-axis, located above finitely-conductive ground.

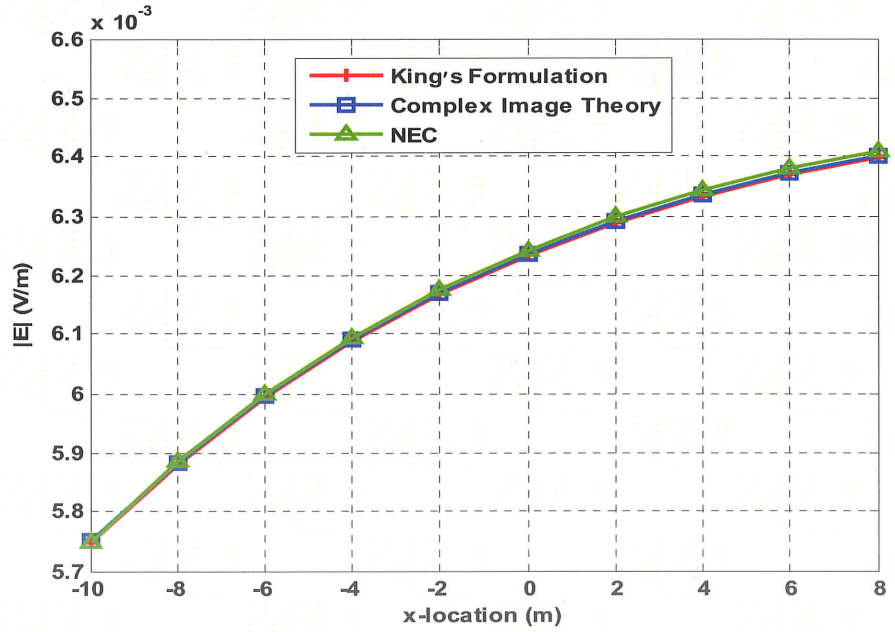

Figure 5.3. The magnitude of the electric field intensity at different observation points located on the ground, calculated at $f = 60$ Hz.

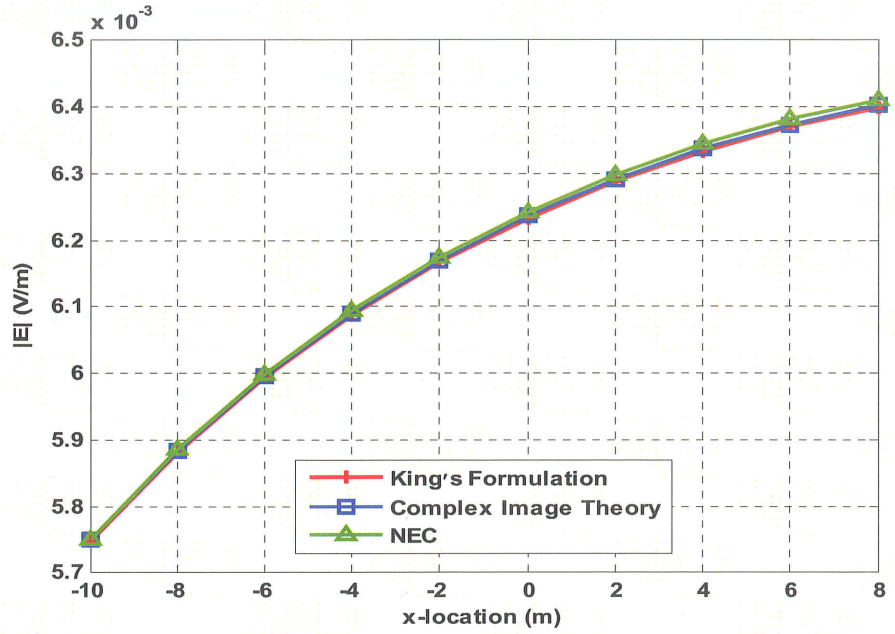

Figure 5.4. The magnitude of the electric field intensity at different observation points located on the ground, calculated at $f = 1$ kHz.

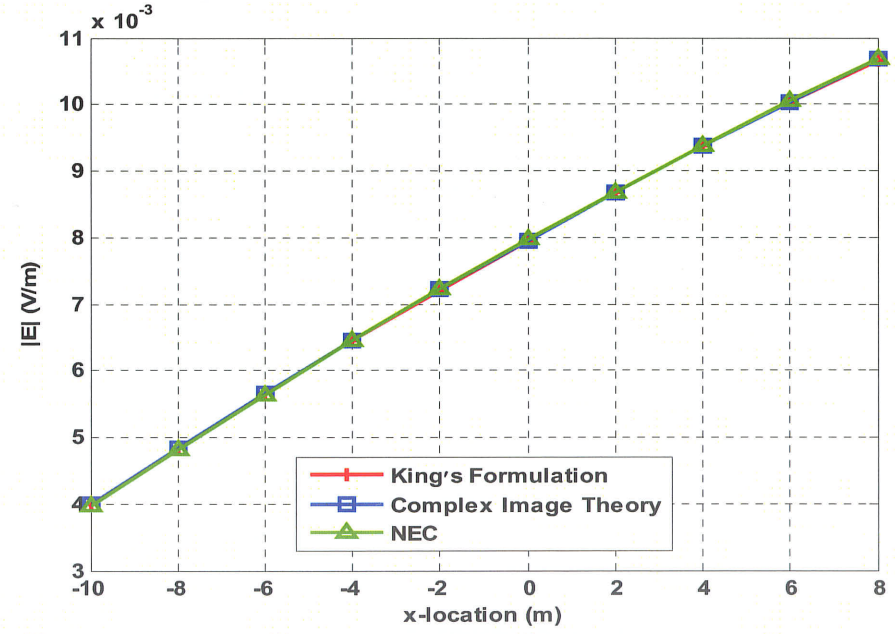

Figure 5.5. The magnitude of the electric field intensity at different observation points located on the ground, calculated at $f = 1$ MHz.

As it is seen in Figures 5.3-5.5, the results derived from NEC agree with those obtained from King's and Bannister's formulations. It should be mentioned that the current distribution along the transmission line used for King's formulation and complex image theory has been extracted from NEC.

The main electrical consideration for using NEC is on the segment length, ΔL, relative to the wavelength, λ. Generally, ΔL should be less than about 0.1λ at the desired frequency [22] and [64]. As the frequency increases, the wavelength of the signal gets smaller; thus, to have valid simulation results at higher frequencies, a smaller length should be selected for each segment, which will result in higher computation time.

Such limitations on applicability of numerical software packages along with their high time-consumption encourage us to employ a general technique to deal with the problem of radiation from power transmission lines.

5.2.1 Time-Domain Application of NEC

In the next step, a time-domain problem is simulated using NEC. The transformation between the frequency- and time-domain has become possible using FFT.

To compare the results derived from NEC with those obtained analytically, the current distribution along the line, when a uniform voltage source is applied, is extracted from NEC. This data corresponds to the impulse response of a linear time-invariant (LTI) system with the excitation voltage as the input and the current distribution along the line as the output. This frequency-domain spectrum is then multiplied by the Fourier transform of the time-domain excitation waveform to find the frequency-domain current

distribution data along the line. This data is employed by the MATLAB code written based on King's formulation and complex image theory to calculate the frequency-domain electric and magnetic fields. Finally, inverse Fourier transform is applied to find the time-domain waveform of the electric and magnetic fields.

Time-domain electric and magnetic fields derived by applying King's formulation and complex image theory are compared with the time-domain NEC results obtained by applying inverse Fourier transform. The flow of this process is shown in Figure 5.6.

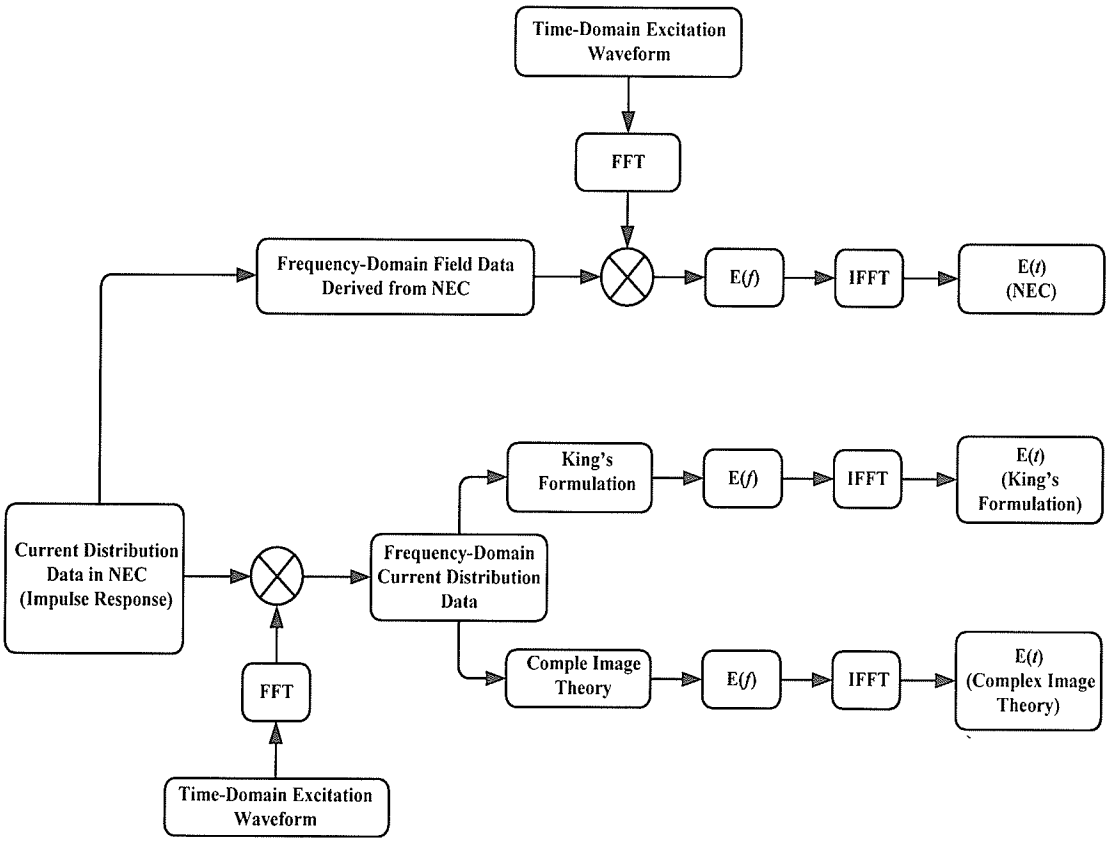

Figure 5.6. The process of calculating time-domain field waveforms using NEC, King's formulation, and complex image theory.

The excitation voltage signal in this problem is a Gaussian waveform given by $V_s(t) = 150 \times e^{-\frac{(t-10^{-6})^2}{2\times10^{-14}}}$. The time- and frequency-steps are respectively selected as 50 ns and 9.77 kHz and the simulation is run for 1025 time and frequency samples. A plot of $V_s(t)$ and its Fourier transform are shown in Figure 5.7. The length and height of the line are respectively selected as 1 km and 20 m. The line is horizontally oriented along the x-axis, starting at x = -500 m, ending at x = 500 m, and divided into 1000 segments. The radius of the conductor is set at 5 cm. The permittivity and conductivity of the ground are chosen as ϵ_r = 4 and σ = 0.1 [S/m]. The frequency spectrum of 0 to 5 MHz is covered by the excitation waveform.

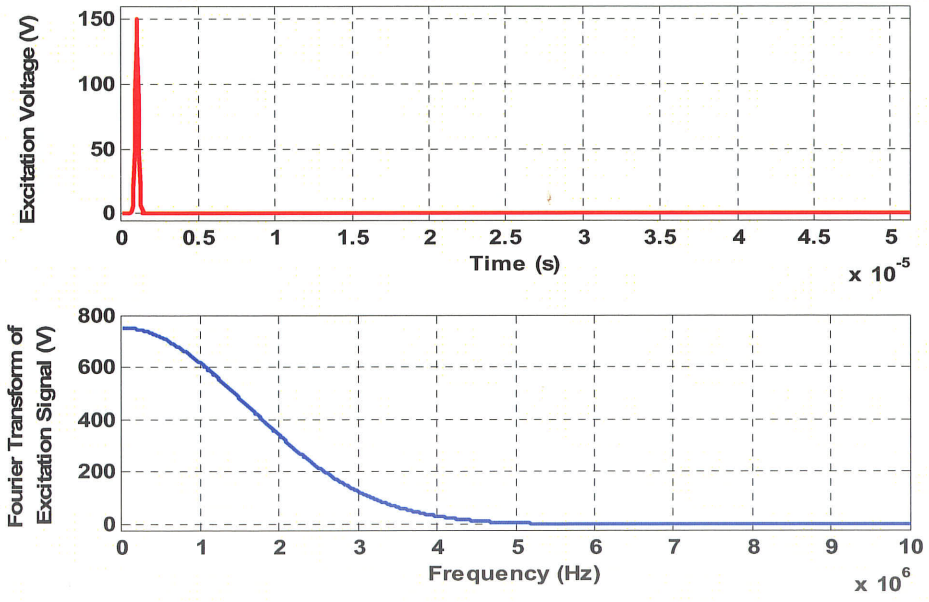

Figure 5.7. Time-domain waveform of Gaussian waveform and its Fourier transform.

As shown in Figure 5.7, the excitation waveform carries a very large DC component. Three components of the electric field vector in the Cartesian coordinate system are calculated using NEC, King's formulation, and complex image theory. The transmission line is excited by the voltage source at its first segment and is left open-circuited at the last segment. The current distribution along the transmission line is found using NEC, which takes the ending reflections into account. The current distribution data is then used by King's formulation and complex image theory to find the electric and magnetic fields in the vicinity of the transmission line. Figure 5.8 shows the time-domain current waveform passing through the first, middle, and the last segment of the line. Figures 5.9-5.11 show the *xyz* components of the electric field intensity vector calculated at (x = 10 m, y =10 m, z = 1 m).

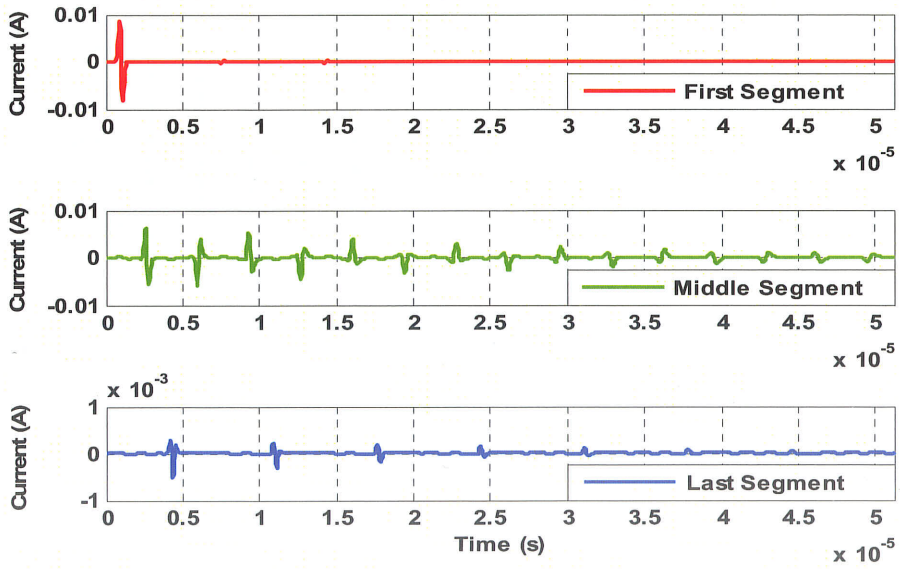

Figure 5.8. Time-domain current waveform passing through the first, middle, and the last segment of the excited transmission line.

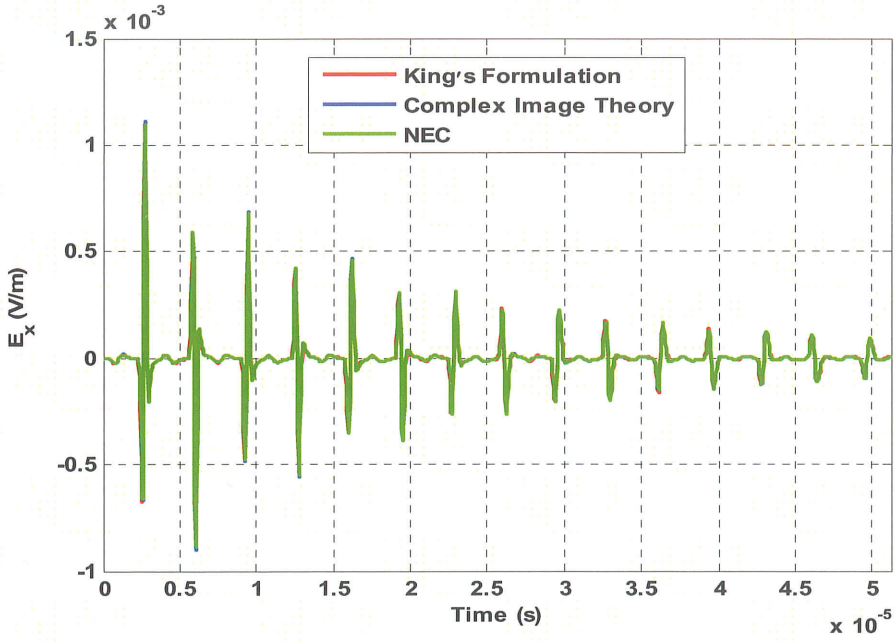

Figure 5.9. The *x*-component of the electric field intensity, calculated at (x = 10 m, y = 10 m, z = 1 m).

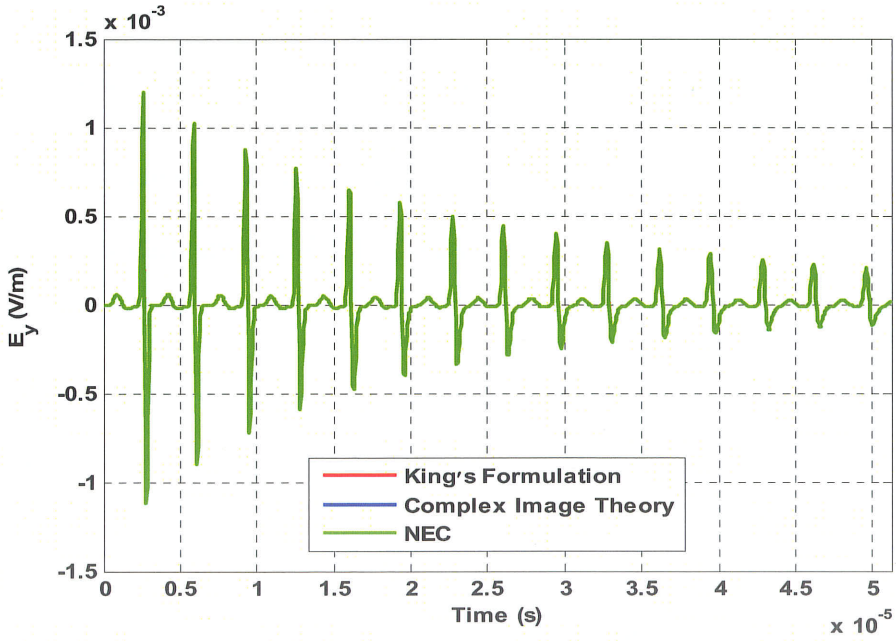

Figure 5.10. The *y*-component of the electric field intensity, calculated at (x = 10 m, y = 10 m, z = 1 m).

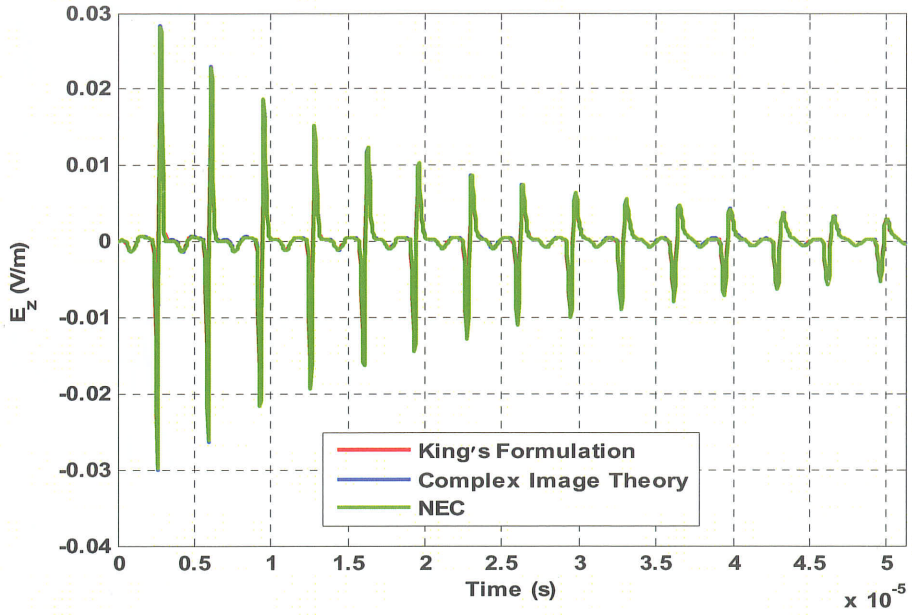

Figure 5.11. The z-component of the electric field intensity, calculated at (x = 10 m, y = 10 m, z = 1 m).

As seen in Figures 5.9-5.11, all the three components of the electric field vector, derived from the three studied approaches, are in a very good agreement with each other.

The same example is simulated with a different excitation source. The second waveform is the derivative of Heidler function [70], with the formula given by

$$V_s(t) = \frac{V_0}{\eta}\frac{(t/\tau_1)^n}{(t/\tau_1)^n + 1}\exp\left(-\frac{t}{\tau_2}\right), \tag{5.1}$$

where $V_0 = 13.1 \times 10^3$ V, $\tau_1 = 2.2 \times 10^{-6}$ s, $\tau_2 = 10^{-6}$ s, $\eta = 0.93$, and $n = 2$.

The excitation waveform and its Fourier transform are shown in Figure 5.12. Time-domain current waveform passing through the first, middle, and the last segment are shown in Figure 5.13. The components of the electric field intensity vector at (x = 10 m, y =10 m, z = 1 m) are presented in Figures 5.14-5.16.

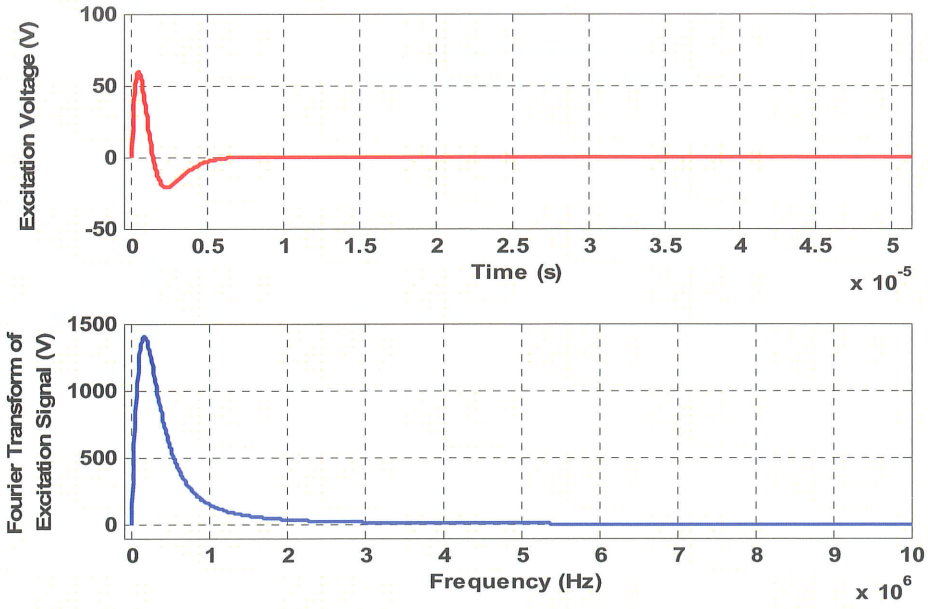

Figure 5.12. Time-domain waveform of the derivative of Heidler function and its Fourier transform.

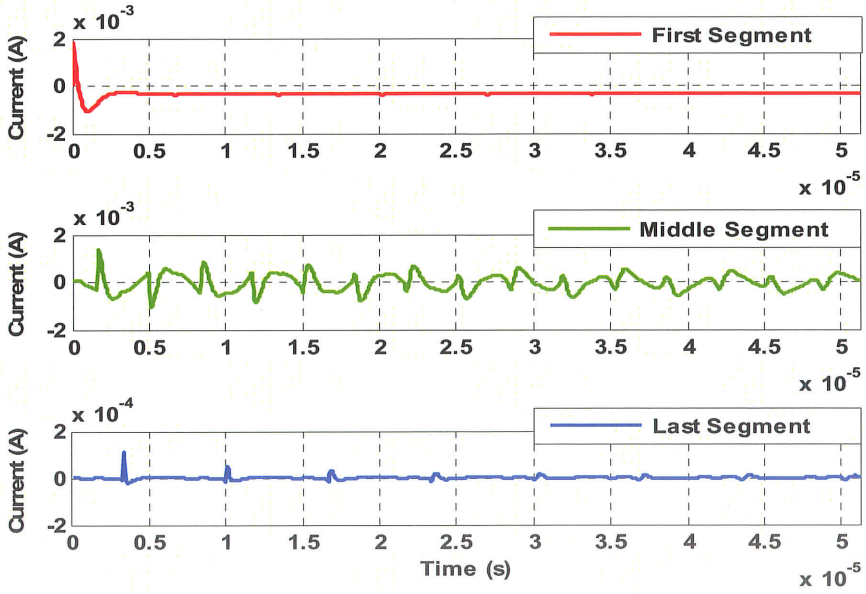

Figure 5.13. Time-domain current waveform passing through the first, middle, and the last segment of the excited transmission line.

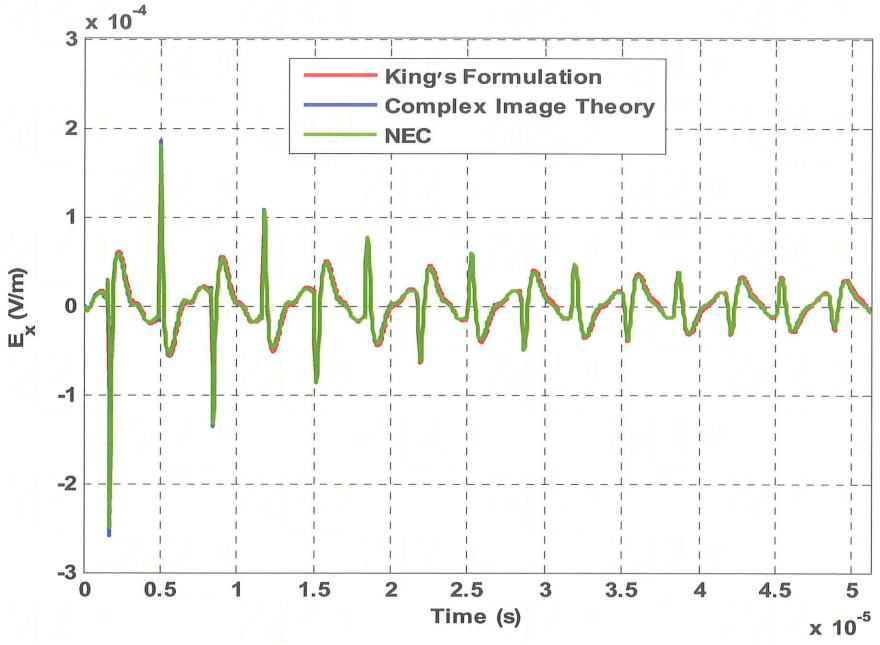

Figure 5.14. The *x*-component of the electric field intensity, calculated at (x = 10 m, y = 10 m, z = 1 m).

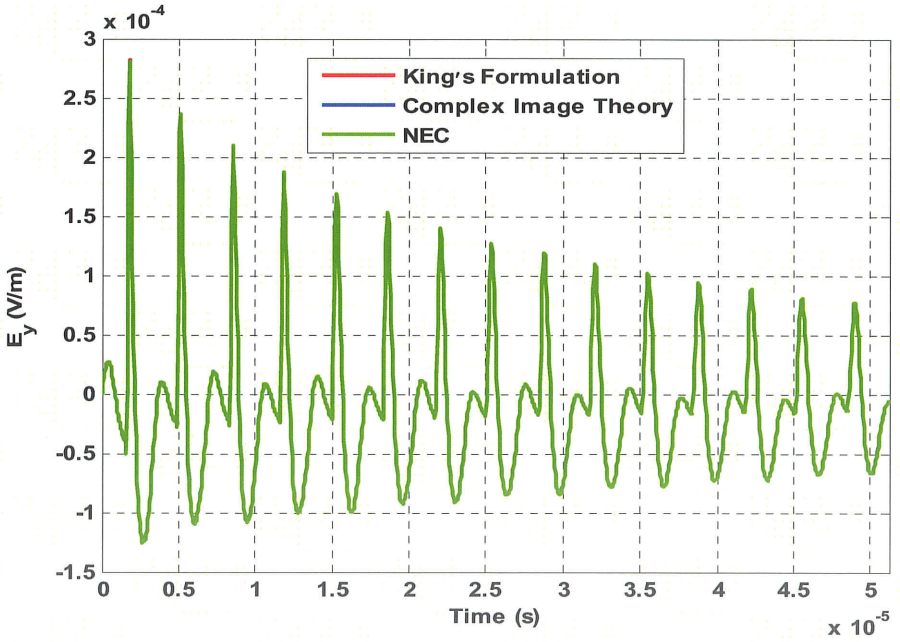

Figure 5.15. The *y*-component of the electric field intensity, calculated at (x = 10 m, y = 10 m, z = 1 m).

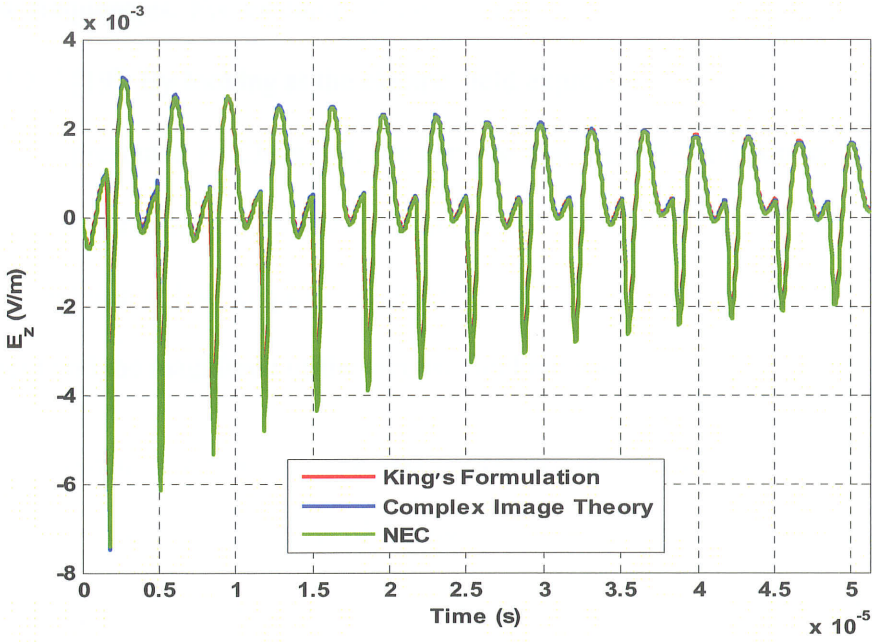

Figure 5.16. The z-component of the electric field intensity, calculated at (x = 10 m, y = 10 m, z = 1 m).

All the three components of the electric field vector, calculated using the three studied approaches, are in very good agreement with each other. The lowest nonzero frequency in this simulation is 9.77 KHz and the simulation is run for 1025 time and frequency samples. If a lower frequency step had been chosen for the simulation, an inaccuracy in the value of x-component of the electric field vector, calculated using King's formulation, would have been observed. In the evaluation of integrals encountered in King's approach, the assumption that the distance between the source and the observation point is not too short is implicit [19]. Specifically, if $k_2 \approx (j\omega\mu_0\sigma_1)^{1/2}$ is the wave-number of the earth and ρ is the radial distance between the source and the observation point, to approximate the integrals with the closed expressions given in (3.10)-(3.15), the condition that $|k_2\rho| > 1$ should be satisfied at all frequencies [19]. This condition is not satisfied for

very low frequencies. For example, at 60 Hz and distance of interest of 15 m, $|k_2\rho| \approx 6.53 \times 10^{-2}$ [19]. By looking at the electric field expressions derived by applying King's formulation, presented in Chapter 3, we can see that the only component of the electric field that is determined entirely by the magnitude of $k_2\rho$ is E_x [19]. Violation of the required condition at low frequencies affects the accuracy of the results derived for the x-component and the magnitude of the electric field intensity.

As observed in Figures 5.9-5.11 and 5.14-5.16, the complex image theory can be employed to predict the magnitude of the electromagnetic fields in the vicinity of a power transmission line. The obtained results are in a good agreement with those obtained from NEC. However, NEC's simulation-time to run this example was in the order of 5 hours, comparing to the 30 min time-consumption using complex image theory. The only condition for applying complex image theory is $|n|^2 \gg 1$.

5.3 The Validity Range of King's Formulation and Complex Image Theory

The only restriction on applying complex image theory is $|k_2/k_1|^2 \gg 1$. The same condition should be satisfied for applying King's set of formulas. To determine the range of frequency for which this condition is satisfied, the value of $|k_2/k_1|^2$ for a wide range of frequency is calculated and shown in Figures 5.17 and 5.18. The value of ground's conductivity is once chosen as 0.001 [S/m] and once as 0.1 [S/m], which are typical values for dry and wet soils. Relative permittivity of the ground takes three different values of 1, 5, and 10.

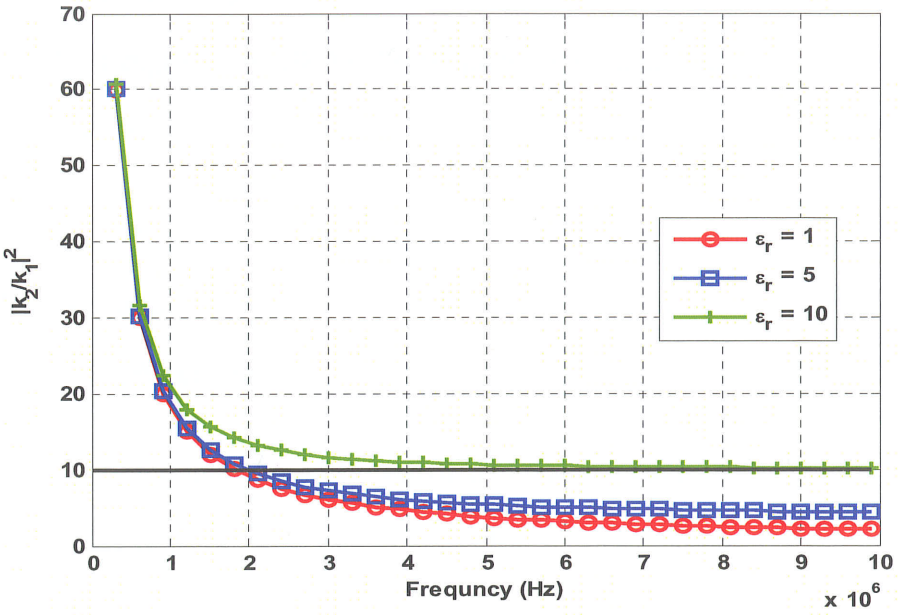

Figure 5.17. The value of $|k_2/k_1|^2$, calculated for three different values of ground's relative permittivity and for the ground's conductivity of σ = 0.001 [S/m].

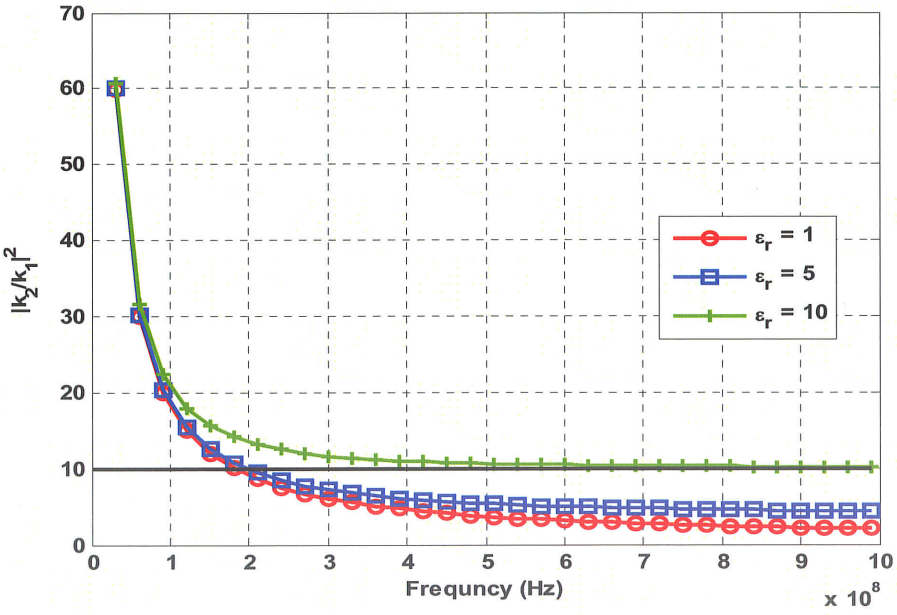

Figure 5.18. The value of $|k_2/k_1|^2$, calculated for three different values of ground's relative permittivity and for the ground's conductivity of σ = 0.1 [S/m].

As it is seen in Figure 5.17 for $\sigma = 0.001$ [S/m] and $\epsilon_r = 1$ or 5, the value of $|n|^2 = |k_2/k_1|^2$ is bigger than 10 for the frequencies smaller than 2 MHz. However, for the same value of σ and $\epsilon_r = 10$, the range of valid frequencies gets as wide as 0-10 MHz.

Figure 5.18 shows that for a typical wet soil with the conductivity of $\sigma = 0.1$ [S/m] and $\epsilon_r = 1$ or 5, $|k_2/k_1|^2 \geq 10$ is satisfied for frequencies in the range of 0-200 MHz. For $\epsilon_r = 10$, the valid frequency range gets wider and becomes as wide as 0-1 GHz.

Another condition should be satisfied for application of King's formulation, which demands the value of $|k_2\rho|$ to be bigger than 1. This restriction puts a limit on the valid frequency range and source-to-observation point distance. Figures 5.19 and 5.20 show the value of $|k_2\rho|$ for a wide range of frequency and three radial distances of 10 m, 50 m, and 100 m. The ground's parameters are fixed at $\epsilon_r = 5$ and $\sigma = 0.001$ and 0.1 [S/m].

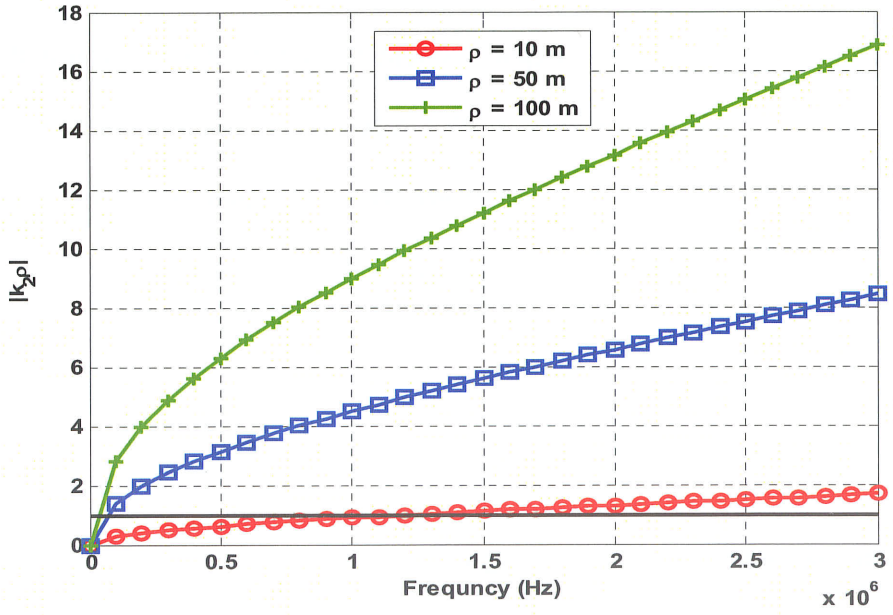

Figure 5.19. The value of $|k_2\rho|$ calculated for three different observation points and the ground's conductivity of $\sigma = 0.001$ [S/m].

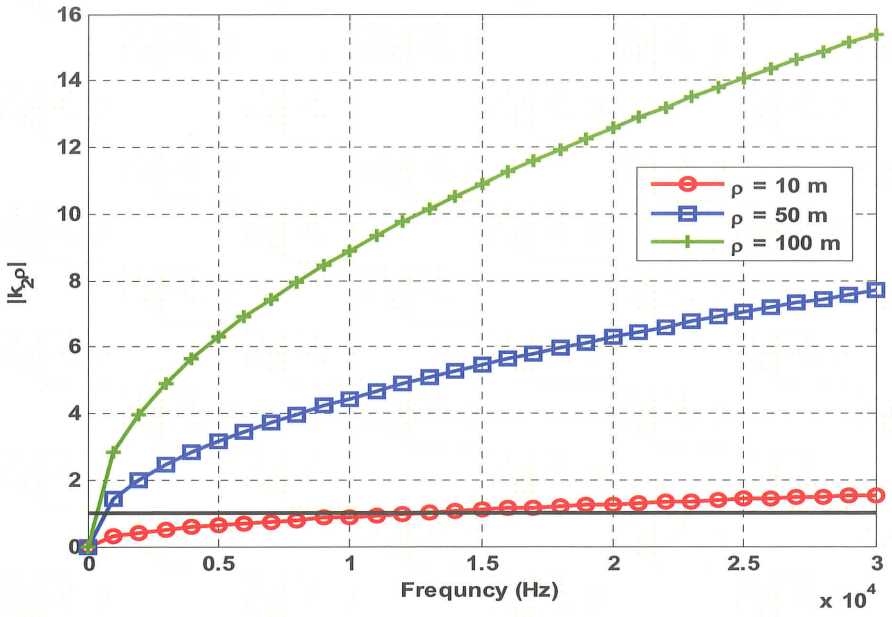

Figure 5.20. The value of $|k_2\rho|$ calculated for three different observation points and the ground's conductivity of σ = 0.1 [S/m].

As seen in Figures 5.19 and 5.20, the second condition for applying King's formulation is not satisfied for low-frequency ranges especially for dry soil. According to Figure 5.19, for $\sigma = 0.001$ [S/m] and ρ = 10 m, the value of $|k_2\rho|$ is smaller than 1 for the frequencies smaller than 1 MHz. However, for $\sigma = 0.1$ [S/m] and ρ = 10 m, the value of $|k_2\rho|$ gets bigger than 1 for frequencies bigger than 10 kHz. Therefore, for very close observation points the validity of King's formulation is questionable at low frequencies.

5.4 Electrostatic, Induction, and Radiation Field Waveforms

In Chapter 2, it was stated that the electromagnetic field expressions associated with an energized element are comprised of three components: electrostatic, induction, and radiation [5]-[7]. The field at any point consists of all the three terms; however,

depending on the distance between the source and the observation point, one or two of these terms will have the main contribution on the total field. The electrostatic field is at its highest value when the observation point is in the near-field range. As we get far from the source, the contribution of the induction and radiation terms becomes more significant. The induction term has a major contribution in the intermediate ranges while the contribution of the radiation term becomes significant at far-field [7]. The definition of the near-, intermediate-, and far-field ranges depends on the excitation frequency [3]. Nonetheless, for time-domain applications, where a wide range of frequency exists, there is no explicit definition for the range of each term.

By looking into the Equation (2.35), it is observed that the induction term has a direct relationship with the current waveform, while the electrostatic and radiation fields vary with the integral and derivative of the excitation waveform, respectively.

In this section, the transition of the field waveforms for different observation points and distinct excitation signals are studied. The simulated line is a 500-m-long overhead line, extended along the *x*-axis with symmetry with respect to the *yz*-plane and located at the height of 20 m over the ground. The line is decomposed into 5000 segments, each with the length of 10 cm. The ground is assumed to be lossless which makes it possible to make use of Equations (2.25) and (2.35). The observation points for this example are located along the *y*-axis where the *x* and *z* coordinates are fixed at -250 m and 0, and *y* takes distinct values of 0, 100 m, and 5000 m. A currents source is placed at the first segment of the line while both ends of the line are open-circuited. The excitation current is a Gaussian waveform with the equation of $i_s(t) = 150 \times e^{-\frac{(t-3\times10^{-7})^2}{10^{-14}}}$. The current is

assumed to propagate along the line with the speed of light and without any attenuation in its amplitude. The effect of reflection from the two open ends of the line is not considered. The input current waveform, its derivative, and its integral over time are shown in Figure 5.21. The time-step is set to 50 ns and the simulation is run for 500 time samples.

The contribution of each of the electrostatic, induction, and radiation terms on the total magnitude of the electromagnetic fields is shown in Figures 5.22-5.27 for three different observation points, located at (x = -250 m, y = 0, z = 0), (x = -250 m, y = 100 m, z = 0), (x = -250 m, y = 5000 m, z = 0).

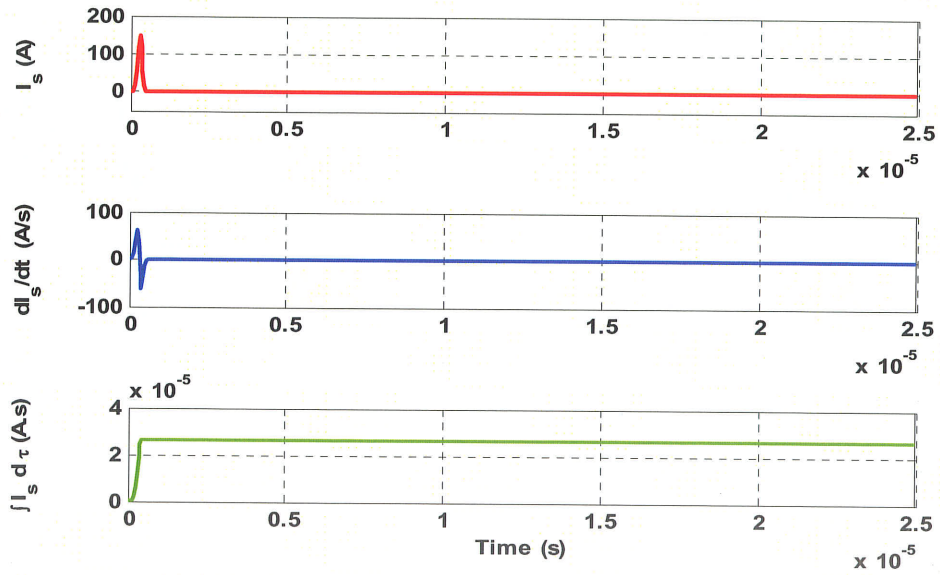

Figure 5.21. A Gaussian waveform, its derivative, and its integral.

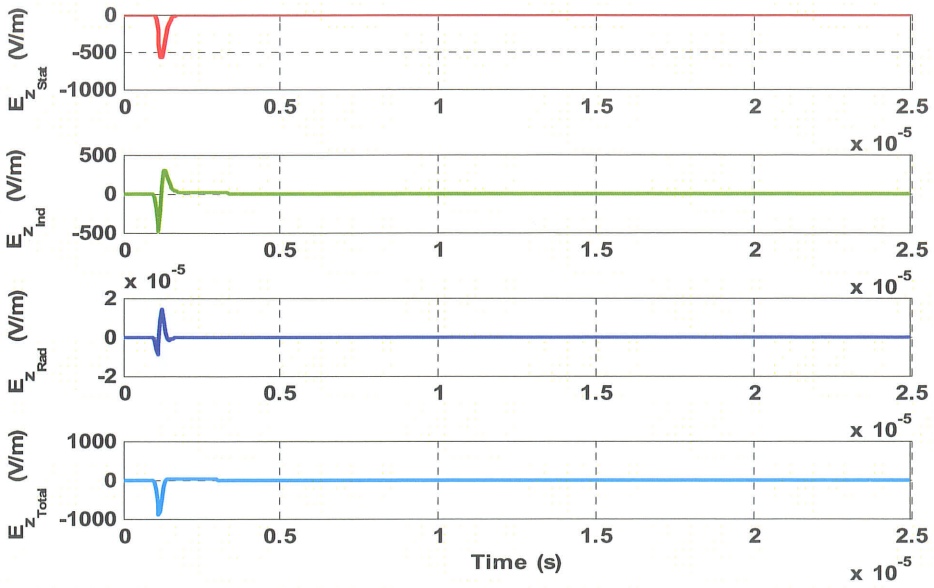

Figure 5.22. Electrostatic, induction, radiation, and total electric field waveforms at (x = -250 m, y = 0, z = 0).

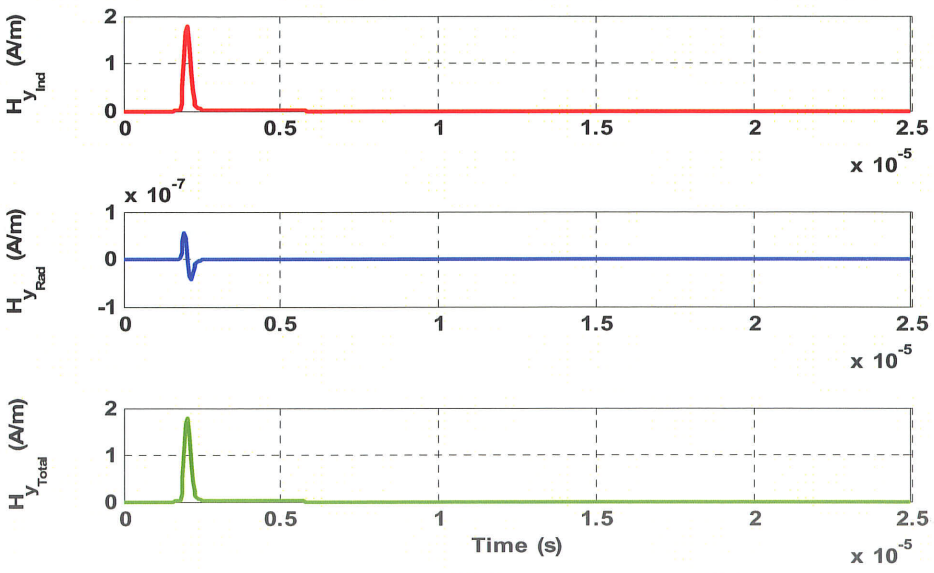

Figure 5.23. Induction, radiation, and total magnetic field waveforms at (x = -250 m, y = 0, z = 0).

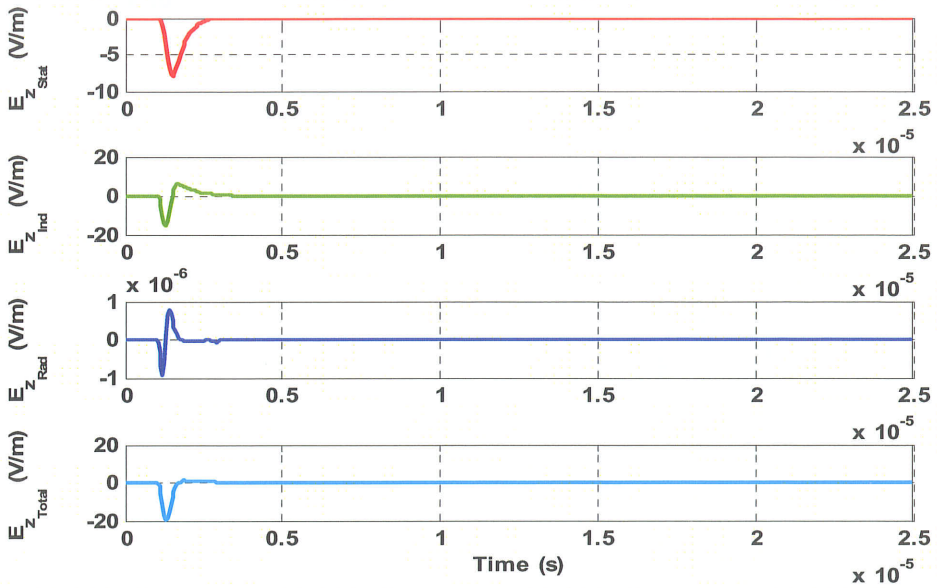

Figure 5.24. Electrostatic, induction, radiation, and total electric field waveforms at (x = -250 m, y = 100 m, z = 0).

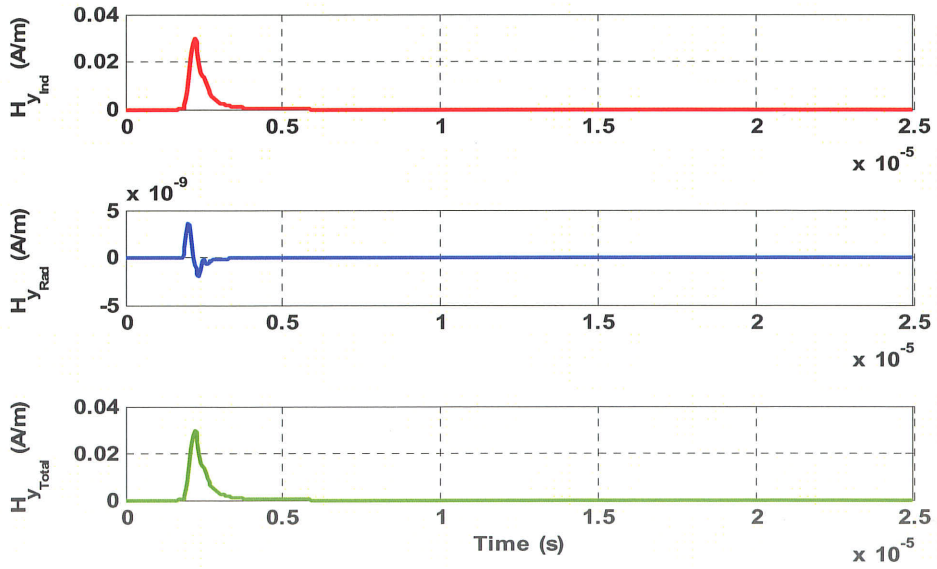

Figure 5.25. Induction, radiation, and total magnetic field waveforms at (x = -250 m, y = 100 m, z = 0).

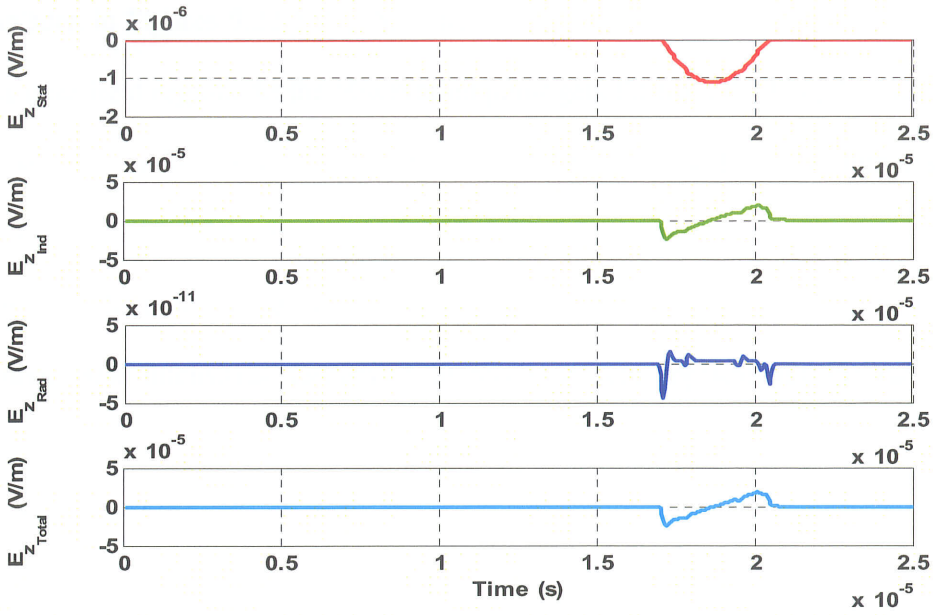

Figure 5.26. Electrostatic, induction, radiation, and total electric field waveforms at (x = -250 m, y = 5000 m, z = 0).

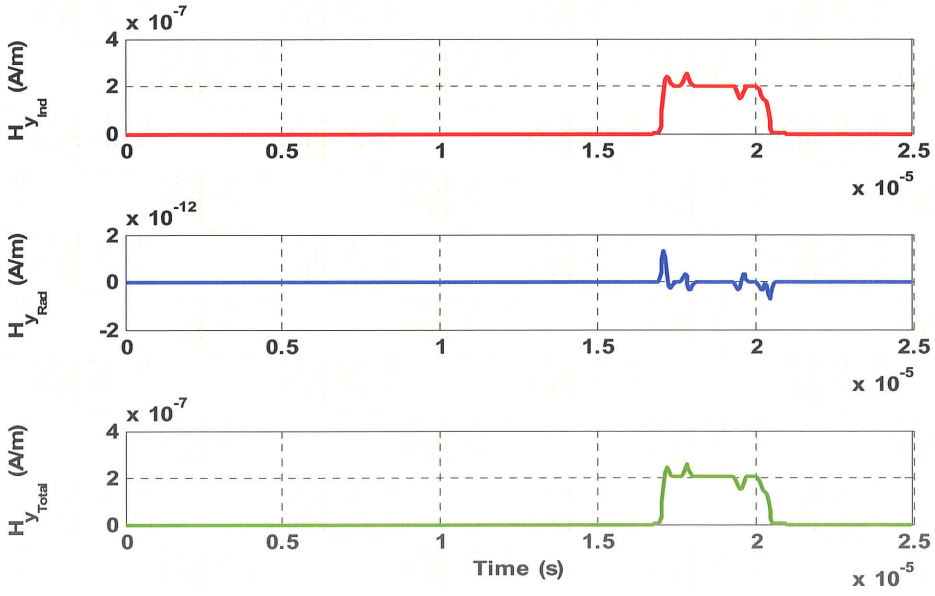

Figure 5.27. Induction, radiation, and total magnetic field waveforms at (x = -250 m, y = 5000 m, z = 0).

As seen in Figures 5.22-5.27, the contribution of electrostatic term is at its maximum in the near-field region. As the observation point gets far from the line, the induction term will have the main contribution on the total electromagnetic fields. In this example and with the chosen excitation signal, the source-to-observation point distance is not large enough for the radiation term to have a significant contribution on the total electric and magnetic field intensities. Generally, in power system applications, the radiation term plays a minor role in the electric and magnetic emission from the line, compared to the electrostatic and induction terms.

5.5 The Accuracy of the Dipole Technique

The main drawback of the dipole technique is the expensive time-consumption of this method which roots from the segmentation of the line into a large number of small dipoles [31]-[33]. In order to have a relatively good accuracy in the calculations, the length of each dipole should be small enough so that the assumption of constant current on each segment sounds reasonable. In a qualitative clarification, the length of the dipole should be small compared to both the wavelength at all the working frequencies and the distance between the source and the observation point.

The main features of the field waveforms that get affected by changing the length of the dipoles are their extremum values. To study the effect of the number of dipoles on the accuracy of the calculation results, the maximum value of the electric and magnetic field vectors' magnitude are calculated for a 2700-m-long transmission line, when the number of dipoles takes the values of 1000, 1350, 2000, and 4000. The line is excited by a

Gaussian current waveform with the equation of $i_s(t) = 150 \times e^{-\frac{(t-2\times10^{-8})^2}{2\times10^{-17}}}$. The current is assumed to propagate along the line with the speed of light and without any attenuation in its amplitude. The simulated line is extended along the *x*-axis with symmetry with respect to the *yz*-plane and located at the height of 20 m over the ground. The electric and magnetic fields are calculated at (x = 10 m, y = 10 m, z = 0) using complex image theory. Table 5.1 shows the dependence of the calculated electric and magnetic field values on the number of dipoles. The total time consumed by MATLAB to run the code for different cases is also shown in Table 5.1

The highlighted row of the table is chosen as the base for the comparison. The difference in the calculation results for different dipole lengths are presented in the percentile format.

It is shown that even when very small segments are used in the decomposition process, the percentage of difference for the magnitude of electric and magnetic fields does not exceed 1% and the rate of the difference is growing smaller at each step. This shows that a decision of trade-off between time and accuracy needs to be taken for each simulation.

Table 5.1. Time-consumption and difference in the value of calculated maximum electric field intensity for different dipole lengths (Δl = 67.5 cm is selected as the base for the comparison).

	Number of segments	|E|	|H|	Computation Time
Δl = 67.5 cm	4000	0%	0%	90 min 15.57 s
Δl = 1.35 m	2000	7.01×10^{-2}%	6.68×10^{-2}%	44 min 22.00 s
Δl = 2 m	1350	2.36×10^{-1}%	1.21×10^{-1}%	31 min 11.24 s
Δl = 2.7 m	1000	3.02×10^{-1}%	2.76×10^{-1}%	21 min 48.62 s

5.6 The Effect of Ground's Conductivity on the Electric and Magnetic Fields

Many investigators have used the approach proposed by Uman [5]-[7], to deal with practical problems such as radiation from high voltage substations [9], power electronic switches [34], transmission lines [8], and power system transients [10]. The first assumption for applying this method, which was reviewed in Chapter 2 of this thesis, is the infinite conductivity of the ground. This assumption is very idealistic and might result in significant amount of error when dealing with practical examples.

To study the impact of ground's conductivity, σ, on the magnitude and waveform of the electric and magnetic fields, complex image theory is employed. The excitation current is a Gaussian waveform with the equation of $i_s(t) = 150 \times e^{-\frac{(t-2\times10^{-8})^2}{2\times10^{-17}}}$. The input current and its Fourier transform are shown in Figure 5.28. The simulated line is a 100-m-long transmission line, extended along the *x*-axis with symmetry with respect to the *yz*-plane and located at the height of 20 m over the ground. The line is decomposed into 4000 segments, each with the length of 2.5 cm. The relative permittivity of the ground is fixed at $\epsilon_r = 4$ and ground's conductivity changes from 0.001 [S/m] to infinity. The transmission line is excited by the current source at its first segment and is left open-circuited at both ends. The current is assumed to propagate along the line with the speed of light and without any attenuation in its amplitude. The effect of reflection from the two open ends of the line is not considered. The electromagnetic fields are calculated at (x = 10 m, y = 10 m, z = 0). The results of this implementation are presented in Figures 5.29-5.36.

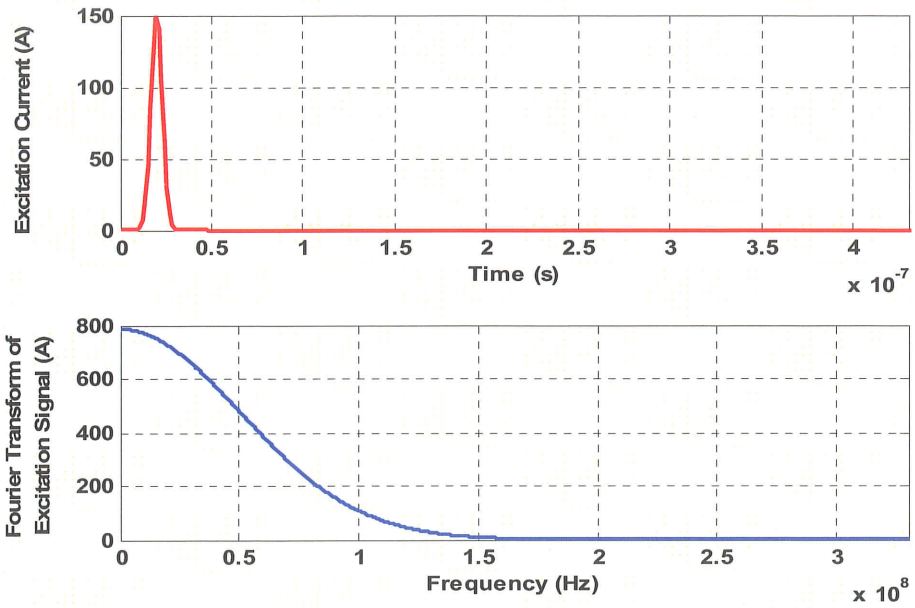

Figure 5.28. Time-domain waveform of Gaussian waveform and its Fourier transform.

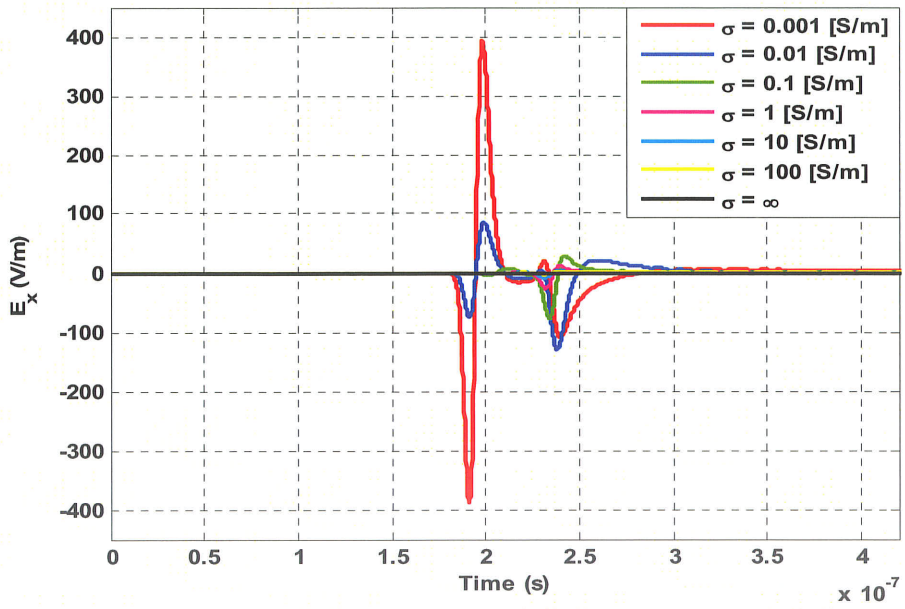

Figure 5.29. Time-domain waveform of the *x*-component of the electric field intensity, calculated at (x = 10 m, y = 10 m, z = 0) for different values of ground's conductivity.

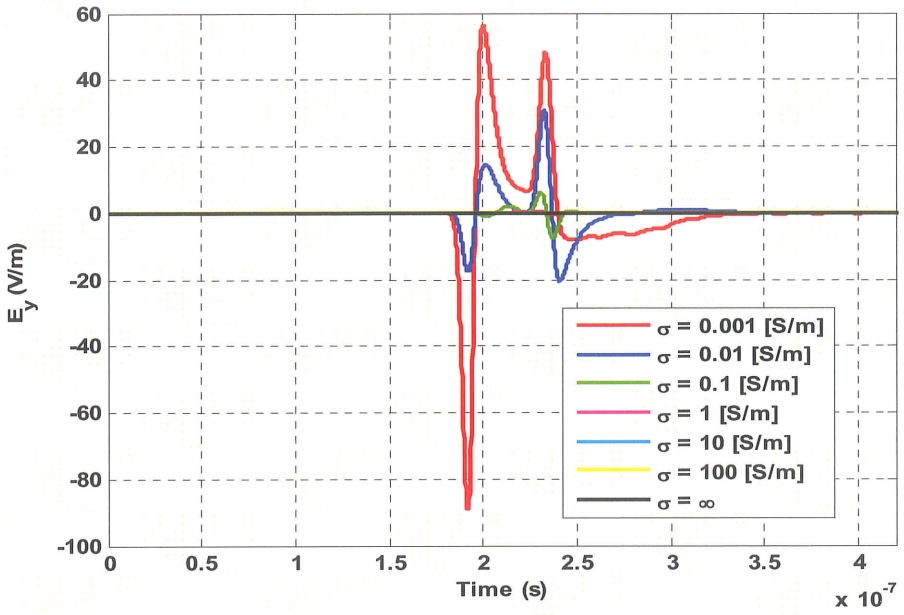

Figure 5.30. Time-domain waveform of the *y*-component of the electric field intensity, calculated at (x = 10 m, y = 10 m, z = 0) for different values of ground's conductivity.

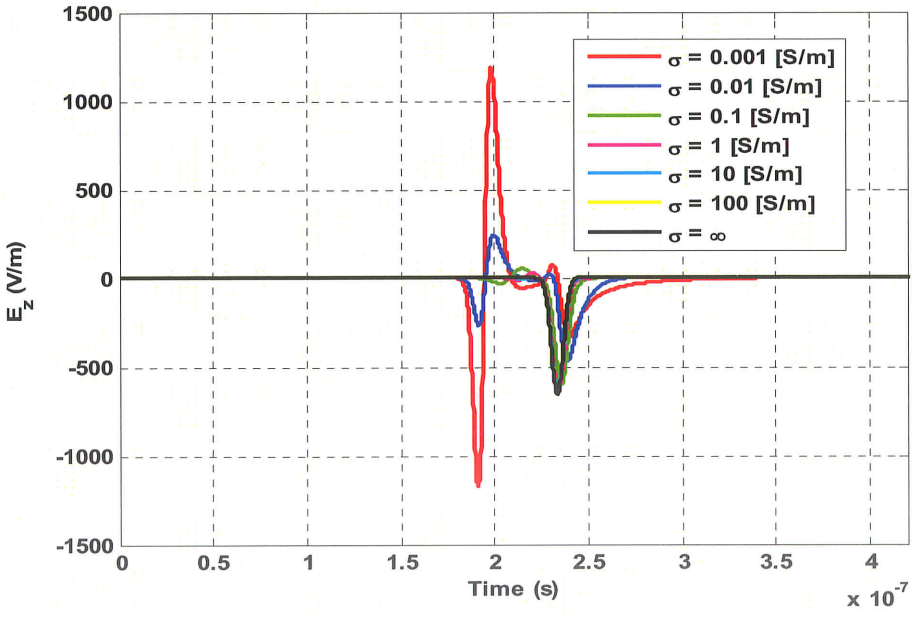

Figure 5.31. Time-domain waveform of the *z*-component of the electric field intensity, calculated at (x = 10 m, y = 10 m, z = 0) for different values of ground's conductivity.

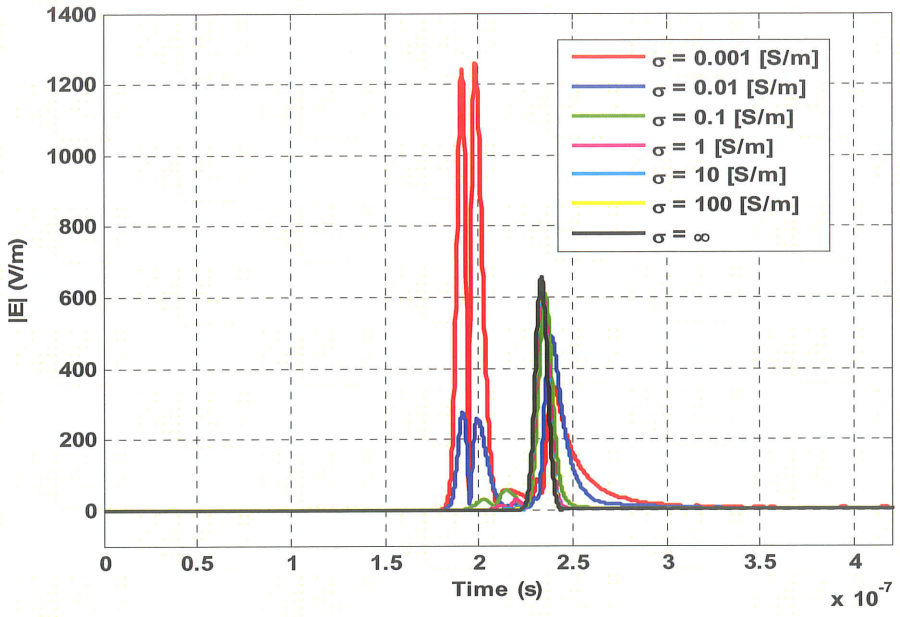

Figure 5.32. Time-domain waveform of the magnitude of the electric field intensity, calculated at (x = 10 m, y = 10 m, z = 0) for different values of ground's conductivity.

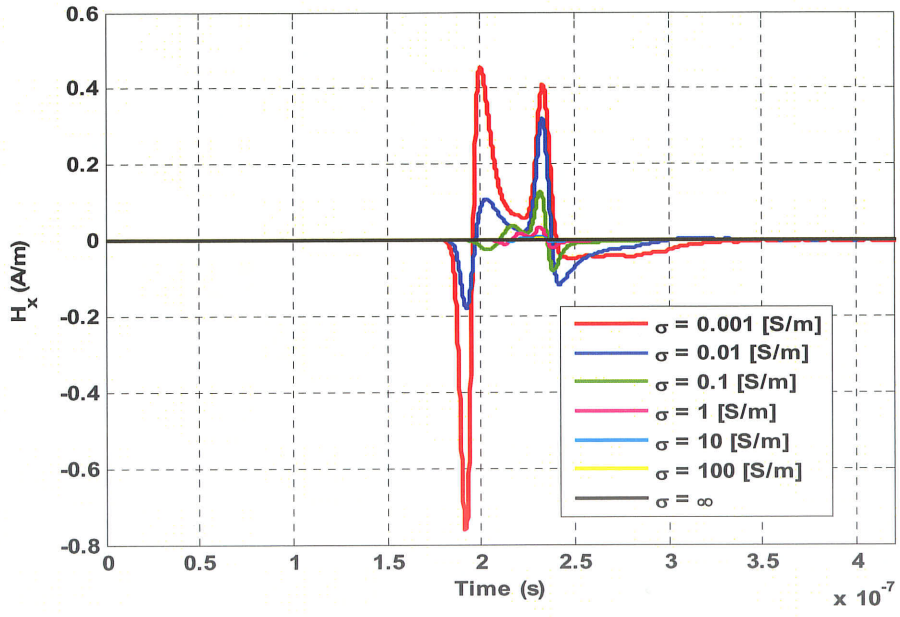

Figure 5.33. Time-domain waveform of the *x*-component of the magnetic field intensity, calculated at (x = 10 m, y = 10 m, z = 0) for different values of ground's conductivity.

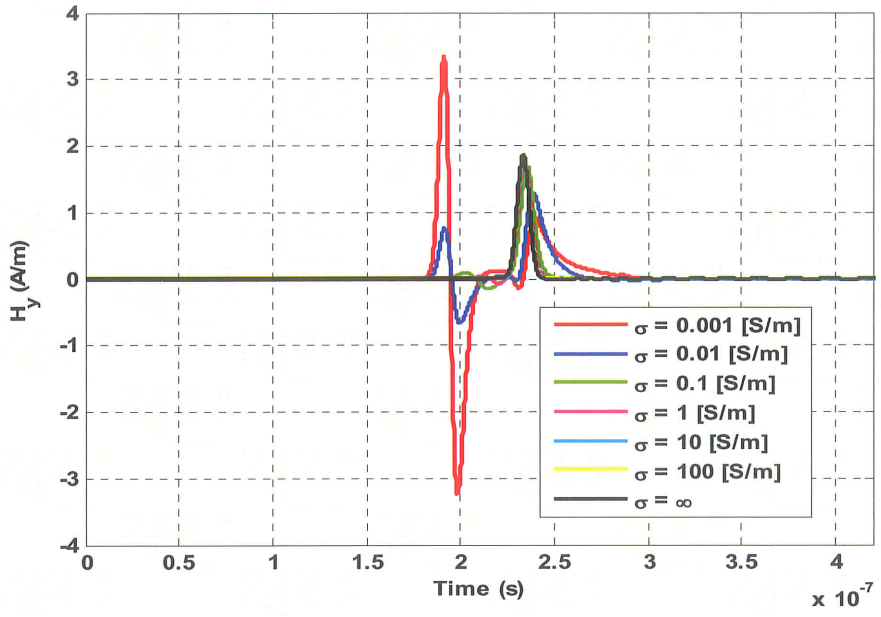

Figure 5.34. Time-domain waveform of the *y*-component of the magnetic field intensity, calculated at (x = 10 m, y = 10 m, z = 0) for different values of ground's conductivity.

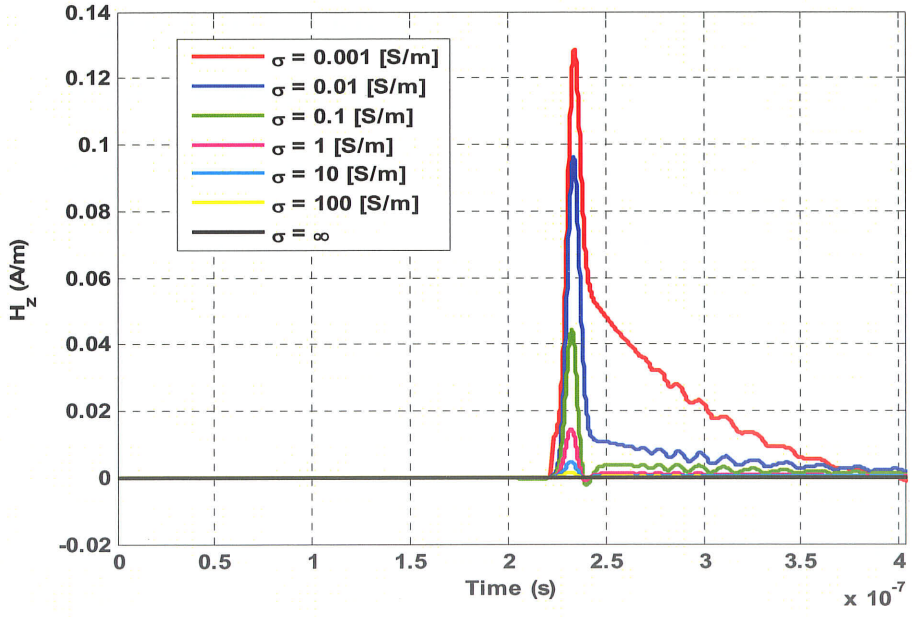

Figure 5.35. Time-domain waveform of the *z*-component of the magnetic field intensity, calculated at (x = 10 m, y = 10 m, z = 0) for different values of ground's conductivity.

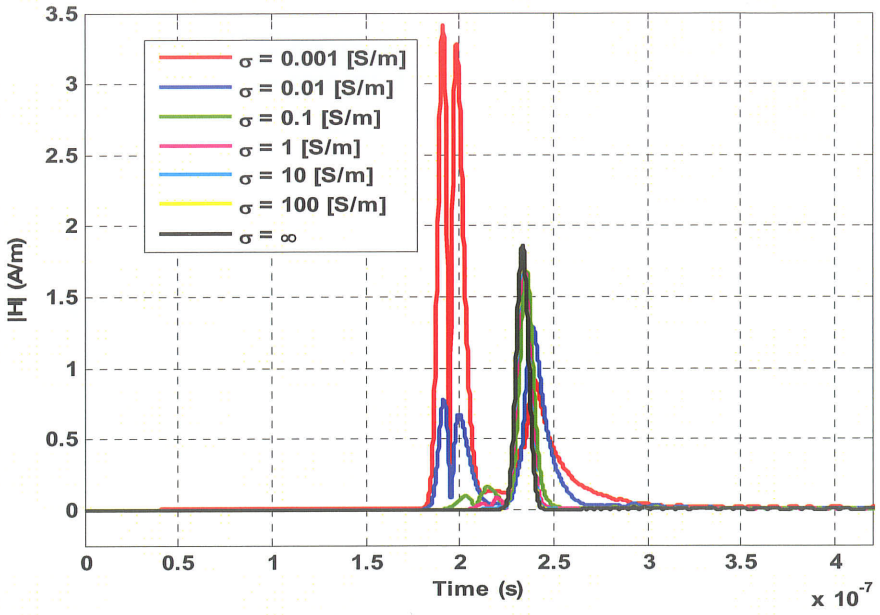

Figure 5.36. Time-domain waveform of the magnitude of the magnetic field intensity, calculated at (x = 10 m, y = 10 m, z = 0) for different values of ground's conductivity.

The results presented in Figures 5.29-5.36 show that all of the six components of the electric and magnetic field vectors change significantly when the value of σ is changed from 0.001 [S/m] to infinity. Even for highly conductive surfaces, the transversal components of the electric field intensity depend on the value of ground's conductivity. Since horizontal components of the electric field have major roles in electromagnetic coupling between horizontal transmission lines, the exact values of these components should be calculated accurately.

Figure 5.37 shows the *x*-component of the electric field intensity, calculated above two highly conductive surfaces, compared to the field calculated for an infinitely conductive ground.

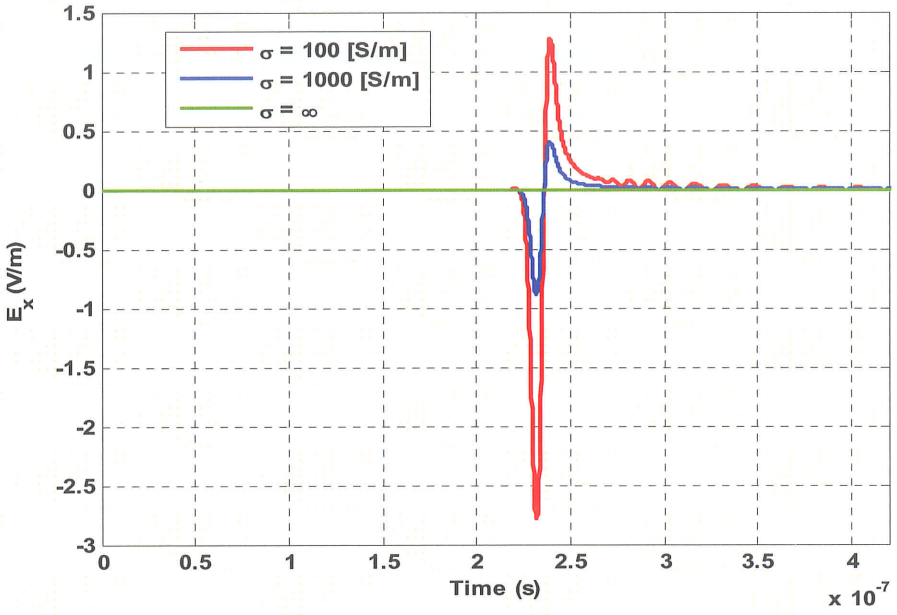

Figure 5.37. Time-domain waveform of the *x*-component of the electric field intensity, calculated at (x = 10 m, y = 10 m, z = 0) for three highly conductive surfaces.

5.7 The Effect of the Conductor Sag

Most of the methods employed for calculating the electric and magnetic fields assume that the current-carrying power transmission lines are straight wires. This assumption results in a model whose electromagnetic fields are distorted from those produced in reality [25] and [26]. The influence of the overhead line's geometry is noticed for the calculation of the electric and magnetic fields, especially in the vicinity of the half-span where the field becomes significant [25] and [26].

For a brief review on the geometry of transmission line's sag, one can refer to the Appendix C of this thesis.

In this section, an algorithm for calculation of the electric and magnetic field distribution near to the sagged overhead lines is presented. In this work, the approximate parabolic formula given in Equation (5.2) is assumed to match with the geometry of the overhead transmission line [26].

$$z = s\left(\frac{2x}{L}\right)^2 + h. \tag{5.2}$$

By knowing the relationship between the height of the sagged conductor and the transversal component (x-coordinate), the location of each segment of the line and its slope will be available. Each segment of the line is then broken into vertical and horizontal components. Each of these components may be treated as vertical/horizontal dipoles. Thus, the field expressions derived in Chapter 3 can be employed to find the total field at any arbitrary point in the vicinity of the transmission line.

The main simplifying approximation in this work is the assumption of the straight wire current distribution for the sagged line. In other word, it is assumed that the slope of each segment is small enough so that the current passing through it will have the same value of the current passing through a straight segment [25]. The decomposition procedure is visualized in Figure 5.38.

The electric and magnetic fields due to each dipole are calculated by applying the complex image theory, using Equations (3.50)-(3.55) and (3.65)-(3.70) derived in Chapter 3.

In this section, the line shown in Figure 5.38 is simulated and the electric and magnetic field intensity vectors are calculated for seven sag values. The simulated line is

a 100-m-long transmission line extended along the x-axis. The conductivity and relative permittivity of the ground are fixed at σ = 0.001 [S/m] and ϵ_r = 4. Seven values for sag, (s = 0, 0.5 m, 1 m, 2 m, 3 m, 4 m, and 5 m), are selected and the electric and magnetic fields are calculated at (x = 10 m, y = 100 m, z = 0).

The line is excited with a current waveform with the equation of $i_s(t) = 300 \times \left(\frac{2\times10^{-8}-t}{2\times10^{-17}}\right) \times e^{-\frac{(t-2\times10^{-8})^2}{2\times10^{-17}}}$. The input current and its Fourier transform are shown in Figure 5.39. The current source is placed at the first segment of the line while both ends of the line are open-circuited. The current is assumed to propagate along the line with the speed of light and without any attenuation. The effect of reflection from the open ends of the line is not considered. Time-domain electric and magnetic field waveforms, calculated using complex image theory, are presented in Figures 5.40 and 5.41.

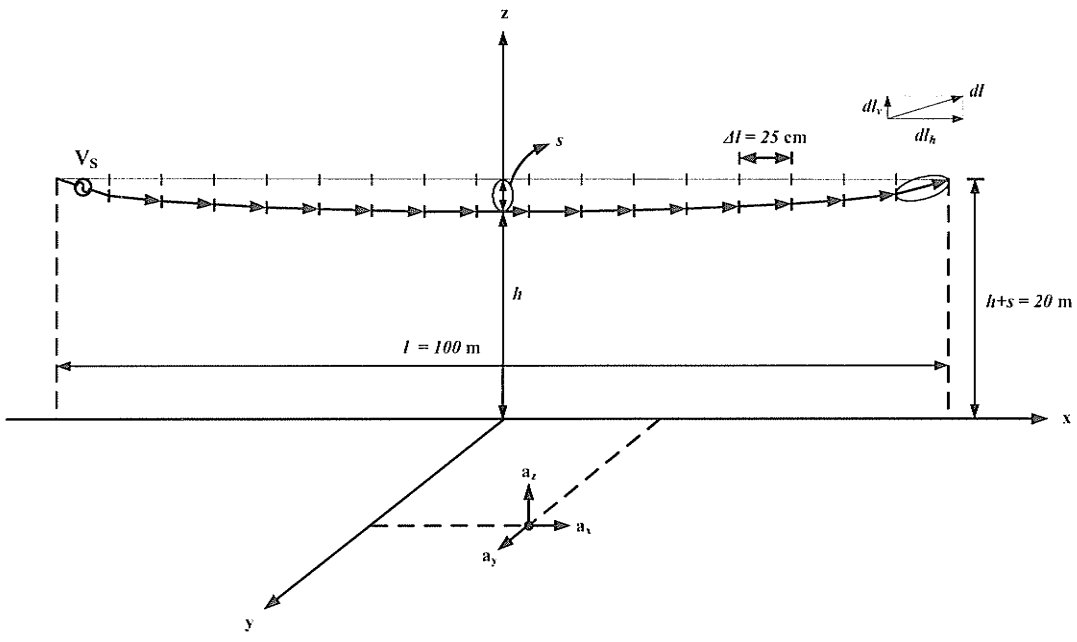

Figure 5.38. Geometry of the decomposed sagged conductor.

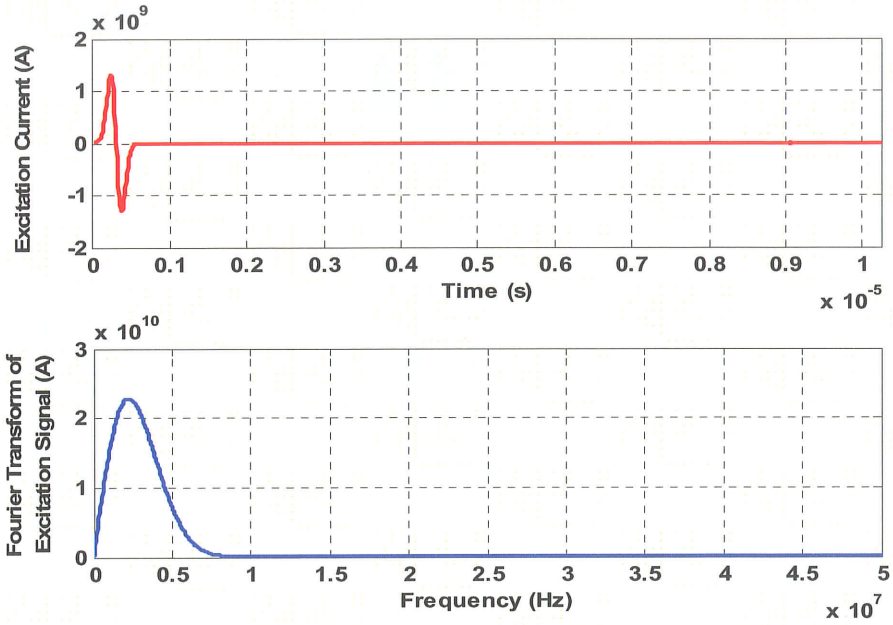

Figure 5.39. Time-domain waveform of the derivative of Gaussian waveform and its Fourier transform

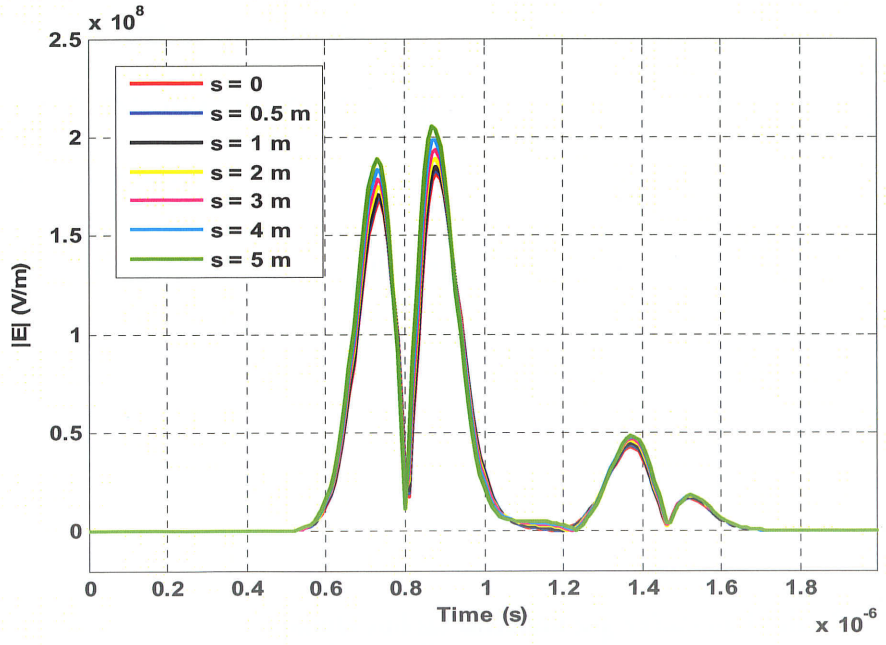

Figure 5.40. Magnitude of the electric field intensity for different values of sag when the observation point is located at (x = 10 m, y = 100 m, z = 0).

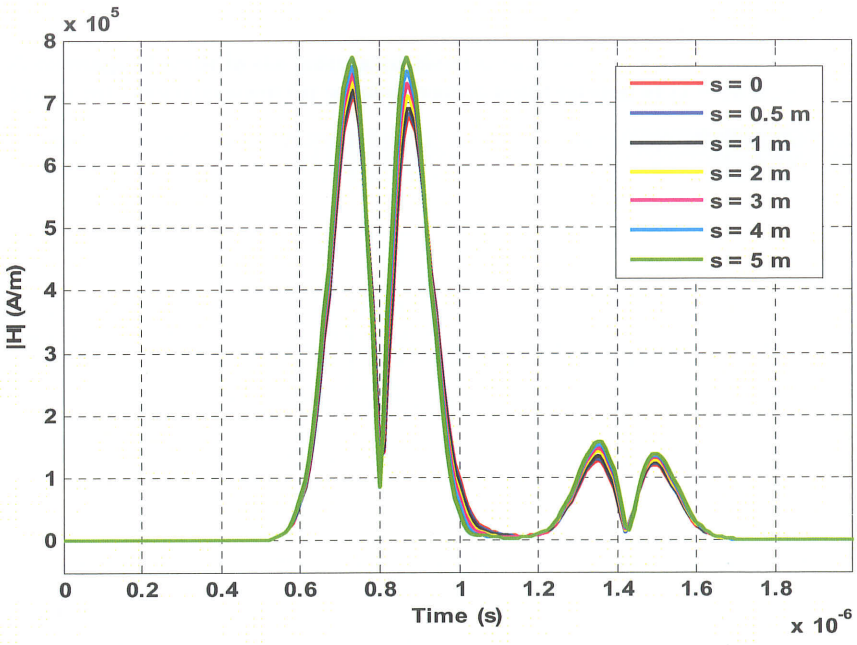

Figure 5.41. Magnitude of the magnetic field intensity for different values of sag when the observation point is located at (x = 10 m, y = 100 m, z = 0).

Figures 5.40 and 5.41 show that for the selected observation point and excitation waveform, the extremum values of the electric and magnetic field vectors highly depend on the value of conductor sag.

As it was mentioned before, the majority of the works done on the topic of electromagnetic radiation from power transmission lines have used the straight wire assumption for the overhead lines. In order to study the effect of the sag on the calculation process quantitatively, the percentage of the error in the maximum electromagnetic field components produced by straight wire approximation is tabulated for four different observation points and six different sag values in Tables 5.2-5.9.

Table 5.2. Percentage of error in the calculated electric field intensity due to not taking the sag of the conductor into consideration for an observation point located at (x = 10 m, y = 0, z = 0).

	$E_{x_{max}}$	$E_{y_{max}}$	$E_{z_{max}}$	$\|\mathbf{E}_{max}\|$
s = 0.5 m	6.27×10^{-2}%	3.31×10^{-2}%	1.33×10^{-1}%	1.33×10^{-1}%
s = 1 m	1.29×10^{-1}%	3.45×10^{-2}%	2.64×10^{-1}%	2.64×10^{-1}%
s = 2 m	2.74×10^{-1}%	5.87×10^{-2}%	5.24×10^{-2}%	5.24×10^{-2}%
s = 3 m	4.35×10^{-1}%	2.81×10^{-1}%	7.78×10^{-1}%	6.84×10^{-1}%
s = 4 m	6.13×10^{-1}%	6.33×10^{-1}%	1.02×10^{-1}%	3.93×10^{-1}%
s = 5 m	8.08×10^{-1}%	1.12	1.27	9.80×10^{-1}%

Table 5.3. Percentage of error in the calculated magnetic field intensity due to not taking the sag of the conductor into consideration for an observation point located at (x = 10 m, y = 0, z = 0).

	$H_{x_{max}}$	$H_{y_{max}}$	$H_{z_{max}}$	$\|\mathbf{H}_{max}\|$
s = 0.5 m	4.50×10^{-2}%	3.43×10^{-2}%	1.06×10^{-1}%	2.82×10^{-2}%
s = 1 m	2.41×10^{-2}%	7.09×10^{-2}%	2.12×10^{-1}%	6.01×10^{-2}%
s = 2 m	1.80×10^{-1}%	1.51×10^{-1}%	4.22×10^{-1}%	1.35×10^{-1}%
s = 3 m	4.69×10^{-1}%	2.42×10^{-1}%	6.30×10^{-1}%	2.27×10^{-1}%
s = 4 m	8.91×10^{-1}%	3.44×10^{-1}%	8.36×10^{-1}%	3.33×10^{-1}%
s = 5 m	1.45%	4.56×10^{-1}%	1.04	4.57×10^{-1}%

Table 5.4. Percentage of error in the calculated electric field intensity due to not taking the sag of the conductor into consideration for an observation point located at (x = 10 m, y = 10 m, z = 0).

	$E_{x_{max}}$	$E_{y_{max}}$	$E_{z_{max}}$	$\|\mathbf{E}_{max}\|$
s = 0.5 m	1.06×10^{-1}%	1.38×10^{-1}%	4.80×10^{-2}%	4.81×10^{-2}%
s = 1 m	2.18×10^{-1}%	3.08×10^{-1}%	9.49×10^{-2}%	9.51×10^{-2}%
s = 2 m	4.55×10^{-1}%	5.62×10^{-1}%	1.85×10^{-1}%	1.85×10^{-1}%
s = 3 m	7.12×10^{-1}%	9.02×10^{-1}%	2.70×10^{-1}%	2.70×10^{-1}%
s = 4 m	9.90×10^{-1}%	1.41%	3.48×10^{-1}%	3.49×10^{-1}%
s = 5 m	1.29%	2.08%	4.19×10^{-1}%	6.64×10^{-1}%

Table 5.5. Percentage of error in the calculated magnetic field intensity due to not taking the sag of the conductor into consideration for an observation point located at (x = 10 m, y = 10 m, z = 0).

	$H_{x_{max}}$	$H_{y_{max}}$	$H_{z_{max}}$	$\|\mathbf{H}_{max}\|$
s = 0.5 m	1.70×10^{-2}%	6.60×10^{-2}%	7.91×10^{-2}%	6.87×10^{-2}%
s = 1 m	7.57×10^{-2}%	1.35×10^{-1}%	1.58×10^{-1}%	1.42×10^{-1}%
s = 2 m	3.19×10^{-1}%	2.82×10^{-1}%	3.13×10^{-1}%	3.03×10^{-1}%
s = 3 m	7.29×10^{-1}%	4.42×10^{-1}%	4.67×10^{-1}%	4.83×10^{-1}%
s = 4 m	1.31%	6.15×10^{-1}%	6.15×10^{-1}%	6.83×10^{-1}%
s = 5 m	2.05%	8.01×10^{-1}%	7.67×10^{-1}%	9.04×10^{-1}%

Table 5.6. Percentage of error in the calculated electric field intensity due to not taking the sag of the conductor into consideration for an observation point located at (x = 10 m, y = 100 m, z = 0).

	$E_{x_{max}}$	$E_{y_{max}}$	$E_{z_{max}}$	$\|\mathbf{E}_{max}\|$
s = 0.5 m	1.07%	7.05×10^{-2}%	9.48×10^{-1}%	9.46×10^{-1}%
s = 1 m	2.18%	4.01×10^{-1}%	1.96%	1.95%
s = 2 m	4.61%	2.98%	4.15%	4.14%
s = 3 m	7.61%	7.75%	6.60%	6.59%
s = 4 m	10.8%	14.7%	9.32%	9.34%
s = 5 m	14.2%	23.9%	13.0%	13.1%

Table 5.7. Percentage of error in the calculated magnetic field intensity due to not taking the sag of the conductor into consideration for an observation point located at (x = 10 m, y = 100 m, z = 0).

	$H_{x_{max}}$	$H_{y_{max}}$	$H_{z_{max}}$	$\|\mathbf{H}_{max}\|$
s = 0.5 m	5.10×10^{-2}%	7.66×10^{-1}%	7.35×10^{-1}%	7.64×10^{-1}%
s = 1 m	4.74×10^{-1}%	1.56%	1.47%	1.55%
s = 2 m	2.44%	3.23%	2.95%	3.21%
s = 3 m	5.90%	5.03%	4.44%	4.98%
s = 4 m	10.85%	6.94%	5.93%	6.85%
s = 5 m	17.3%	8.98%	7.43%	8.85%

Table 5.8. Percentage of error in the calculated electric field intensity due to not taking the sag of the conductor into consideration for an observation point located at (x = 10 m, y = 300 m, z = 0).

	$E_{x_{max}}$	$E_{y_{max}}$	$E_{z_{max}}$	$\|\mathbf{E}_{max}\|$
s = 0.5 m	2.08%	2.65×10^{-1}%	1.28%	1.27%
s = 1 m	4.24%	1.51%	3.03%	3.02%
s = 2 m	8.80%	6.95%	9.32%	9.40%
s = 3 m	13.7%	16.3%	18.8%	18.8%
s = 4 m	18.9%	15.5%	33.7%	33.9%
s = 5 m	24.4%	4.70%	53.3%	53.6%

Table 5.9. Percentage of error in the calculated magnetic field intensity due to not taking the sag of the conductor into consideration for an observation point located at (x = 10 m, y = 300 m, z = 0).

	$H_{x_{max}}$	$H_{y_{max}}$	$H_{z_{max}}$	$\|\mathbf{H}_{max}\|$
s = 0.5 m	4.43×10^{-1}%	1.22%	1.35%	1.21%
s = 1 m	2.13%	2.49%	2.70%	2.46%
s = 2 m	9.27%	5.18%	5.40%	5.05%
s = 3 m	12.0%	8.05%	8.08%	7.81%
s = 4 m	5.50%	11.2%	10.8%	12.6%
s = 5 m	29.2%	14.7%	13.4%	18.4%

The results presented in Tables 5.2-5.9 show that the error due to not taking the sag of the conductor into account for the magnitude of electric and magnetic field has its highest value when the observation point gets far from the line. The amount of this error in calculation of electric and magnetic fields can be as high as 50% and 20%, respectively.

This observation can be justified by knowing that as the distance between the source and the observation point increases, the electromagnetic fields due to a horizontal dipole vanish much faster than those of a vertical dipole. As a result, as the observation point gets far from the transmission line, the impact of the small vertical dipoles on the total

electric and magnetic fields becomes more observable. Figures 5.42 and 5.43 show the dependency of the electric and magnetic field intensities on the source-to-observation point distance for horizontal and vertical dipoles. The horizontal and vertical dipoles are placed at (x = 0, y = 0, z = 15 m) above the ground with ϵ_r = 4 and σ = 0.1 [S/m]. The magnitude of the electric and magnetic fields corresponding to 50-cm-long horizontal/vertical dipoles are calculated at different observation points. Both of the dipoles are excited with a current waveform with the amplitude of 100 A and frequency of 100 kHz.

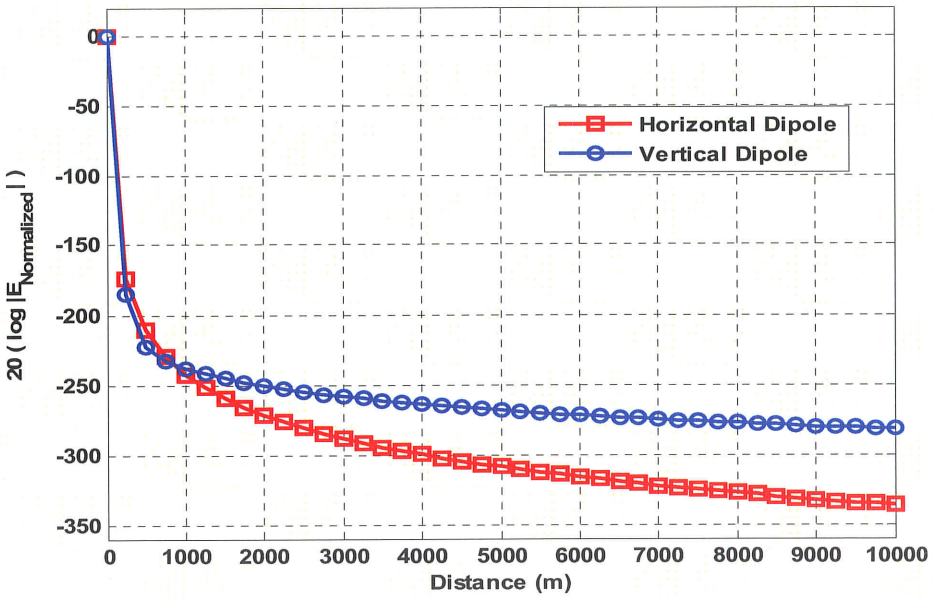

Figure 5.42. Variation of the maximum electric field intensity with the distance.

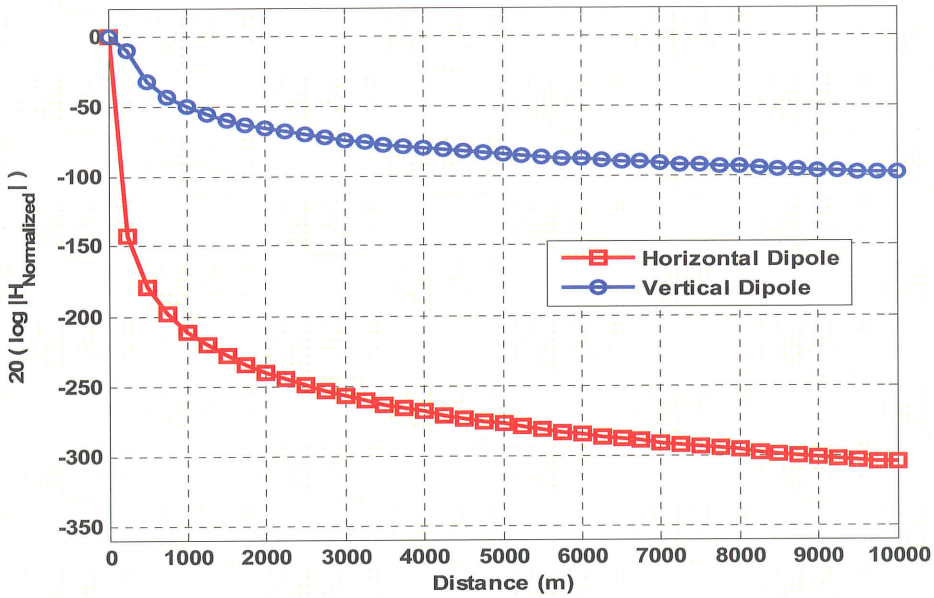

Figure 5.43. Variation of the maximum magnetic field intensity with the distance.

5.8 Application of MFDTD in Finding the EM radiation from the Line

In all of the examples mentioned earlier, the current distribution along the transmission line was assumed to be given. In other word, it was assumed that the excitation waveform propagates through the line with the speed of light and without any attenuation in its amplitude. This is true only for the case of a lossless transmission line.

In practical cases, finding the current distribution along the line is of crucial importance. To find the current on each segment of the decomposed line using the aforementioned dipole technique, we need to solve the well-known Telegrapher's equations given in Equations (5.3) and (5.4):

$$\frac{\partial}{\partial x}\mathbf{I}(x,s) + \mathbf{Y}(s)\mathbf{V}(x,s) = 0, \tag{5.3}$$

and,

$$\frac{\partial}{\partial x}\mathbf{V}(x,s) + \mathbf{Z}(s)\mathbf{I}(x,s) = 0. \tag{5.4}$$

FDTD technique can be applied to solve the system of the equations given in (5.3) and (5.4). In this thesis use is made of a recently implemented Modified FDTD (MFDTD) technique [23] and [24] to acquire the data regarding the current distribution along the line. In this technique, the frequency dependence of the per unit length parameters of the transmission line has been taken into account [23].

Using this technique, the magnitude and phase of current passing through each dipole can be obtained by knowing the excitation waveform. Thereafter, by merging the dipole technique and complex image theory, time-domain electric and magnetic field waveforms at any point in the vicinity of the transmission line can be found with a very good accuracy [68] and [69]. This algorithm can be applied for finding the radiation due to lightning, switching transients, power system over-voltages, and any other kind of transients associated with transmission lines.

In this section, a multi-conductor transmission line with the length of 10 km is simulated using MFDTD technique. The current distribution along the line is then extracted to find the electric and magnetic fields in the vicinity of the line. The geometrical properties of the simulated line are shown in Figures 5.44 and 5.45 [23].

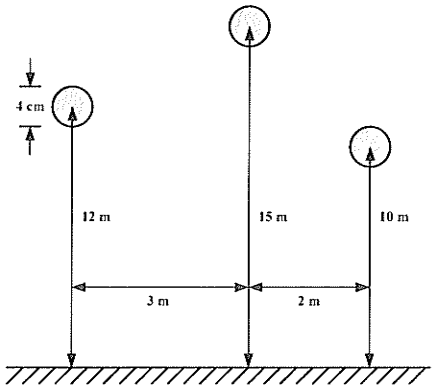

Figure 5.44. Cross-sectional view of the simulated multi-conductor transmission line.

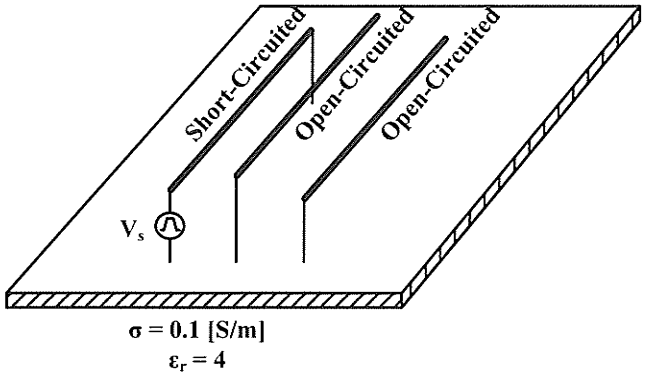

Figure 5.45. Geometry of the simulated multi-conductor transmission system.

As shown in Figure 5.45, the second and third conductors are short- and open-circuited at the sending and receiving ends, respectively. The receiving end of the first conductor is also short circuited. The excitation voltage waveform is a transient waveform with the equation of $V_s(t) = \frac{2(2.25\times10^{-6}-t)}{10^{-7}} \times e^{-\frac{(t-2.25\times10^{-6})^2}{10^{-12}}}$. The input voltage and its Fourier transform are shown in Figure 5.46. Figures 5.47 and 5.48 represent the electric and magnetic field components at an observation point in the air, located at (x = 10 m, y = 10 m, z = 0).

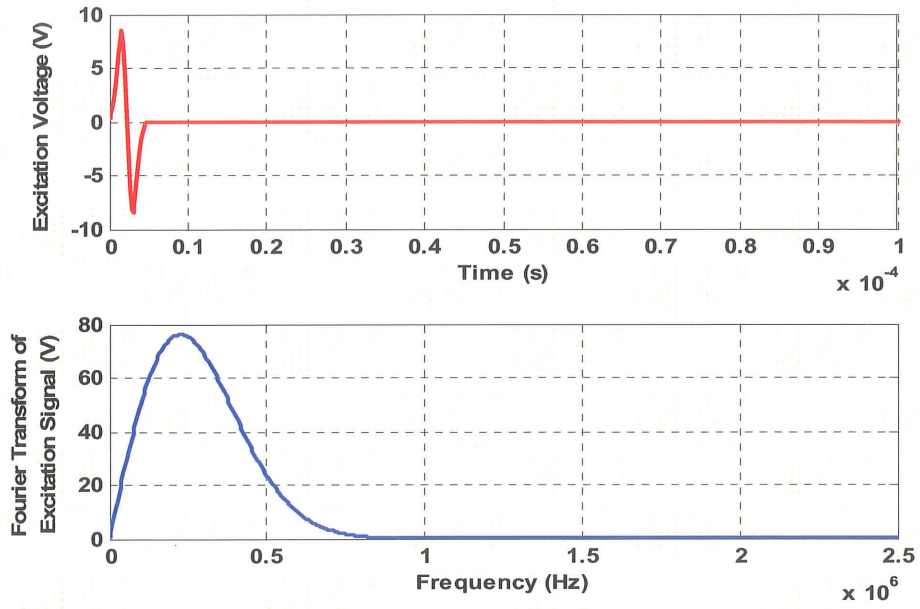

Figure 5.46. Time-domain excitation waveform and its Fourier transform.

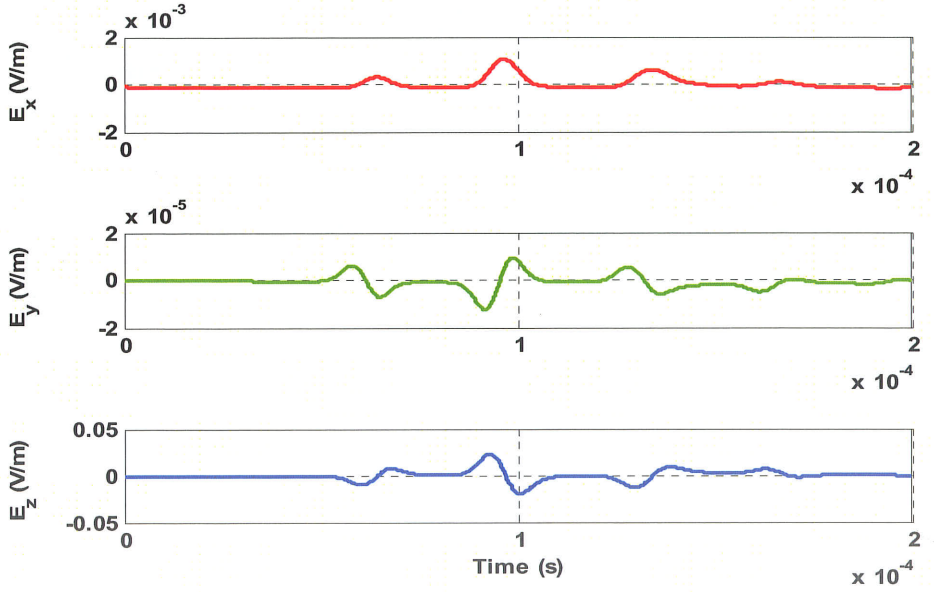

Figure 5.47. Transient electric field intensity waveform, calculated at (x = 10 m, y = 10 m, z = 0).

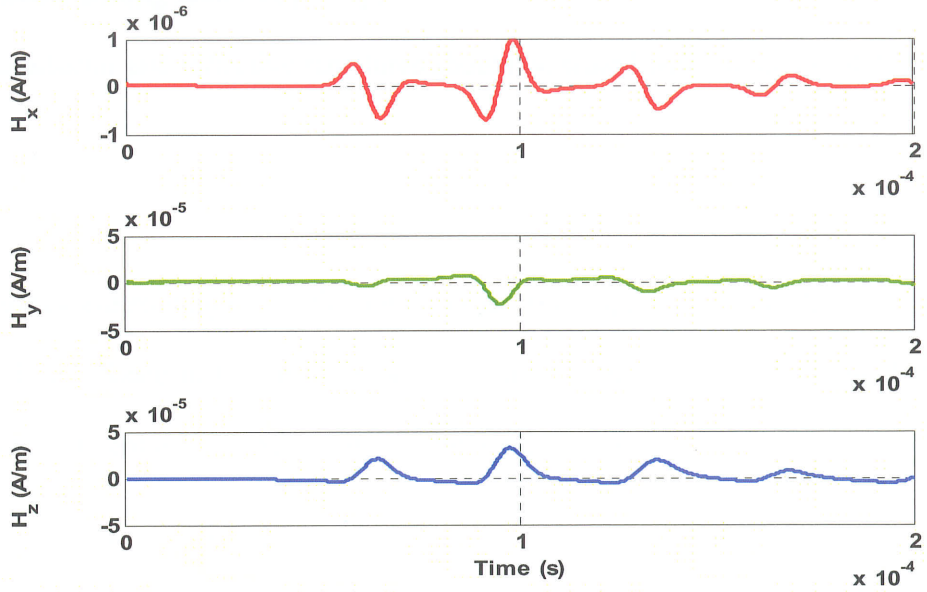

Figure 5.48. Transient magnetic field intensity waveform, calculated at (x = 10 m, y = 10 m, z = 0).

5.9 The Effect of Downscaling on the Electric and Magnetic Fields

In Chapter 4, the importance of the scale modeling and the scale laws were briefly reviewed. According to the statements made in Chapter 4, in order to be able to expand the results obtained from a reduced-scale model and predict the behaviour of the full-scale system, appropriate scale factors should be applied to each parameter of interest. In Table 4.1, the scale factors for most of the parameters that we come across in transient EM problems were illustrated.

The assumption that the intrinsic parameters of conductors and the surrounding surfaces, (σ, ϵ, μ), do not change during the scaling process will bring some error and inaccuracy in our calculations. Based on the discussions made in Chapter 4, if a

geometric scaling factor of p is applied to a transmission line system, the conductivity of the conductor and reflective structures should be scaled with the factor of $1/p$ to have an ideal downscaled system.

According to the results derived from complex image theory, the effect of lossy ground on electromagnetic radiation becomes more significant when the height of the line is reduced. Since in the scaled model the line is very close to the ground surface, the effect of the ground's conductivity becomes significant.

To analyze the effect of scaling on the electric and magnetic fields associated with a transmission line, the example shown in Figure 5.49 is simulated using NEC. To determine the amount of error caused by choosing the same intrinsic parameters for the ground, the scaled model is simulated once when the value of σ is not scaled and once with the scaled value for σ. The original line is a 100-m-long horizontal line extended along the x-axis and excited by a voltage source of amplitude 150 V and frequency of 60 Hz. The line is decomposed into 500 segments and the radius of the conductor is set to 5 cm. The line is located above lossy ground with the intrinsic parameters of $\epsilon_r = 4$ and $\sigma = 0.01$ [S/m].

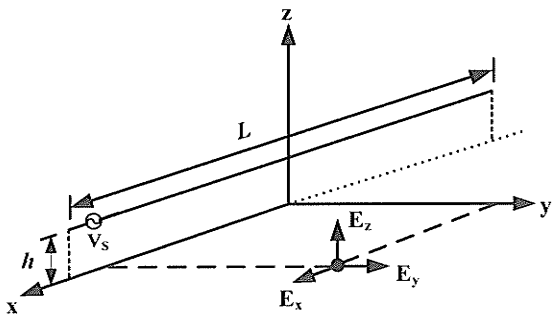

Figure 5.49. A model of an overhead transmission line.

The scaling factors for all the parameters of interest are given in

Table 5.10. The electric and magnetic fields at the ground level for eleven distinct observation points are found for the original and scaled systems. The *xyz* components and the total magnitude of the fields are illustrated in Figures 5.50-5.57.

Table 5.10. Scale factors applied for different parameters.

Parameter	Scale Factor
Length (l)	1/16
Electric Field Intensity (E)	1
Magnetic Field Intensity (H)	1
Frequency (f)	16
Conductivity (σ)	1 and 16
Voltage (V)	1/16

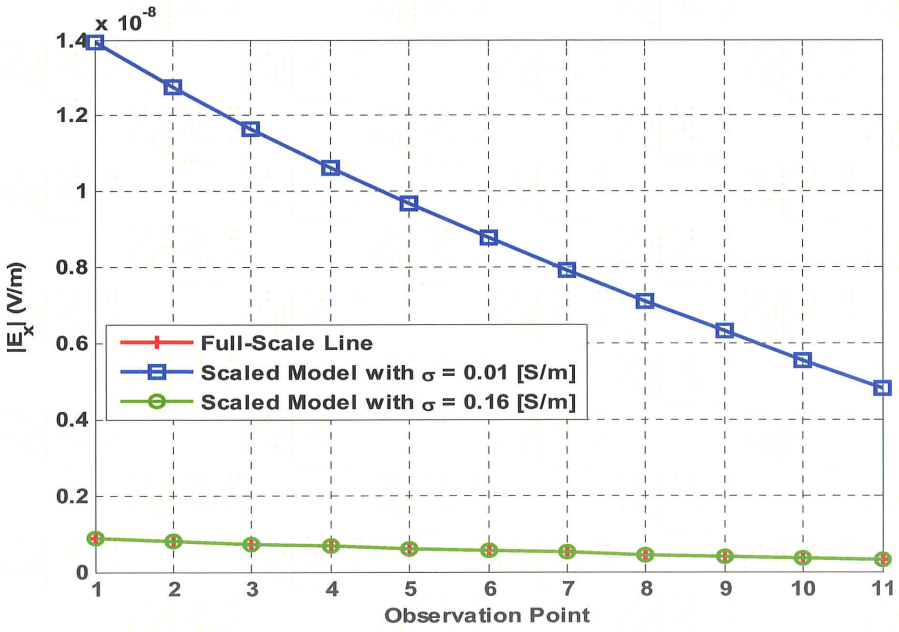

Figure 5.50. The *x*-component of the electric field intensity for the full-scale and downscaled transmission systems, with and without scaling the ground's conductivity.

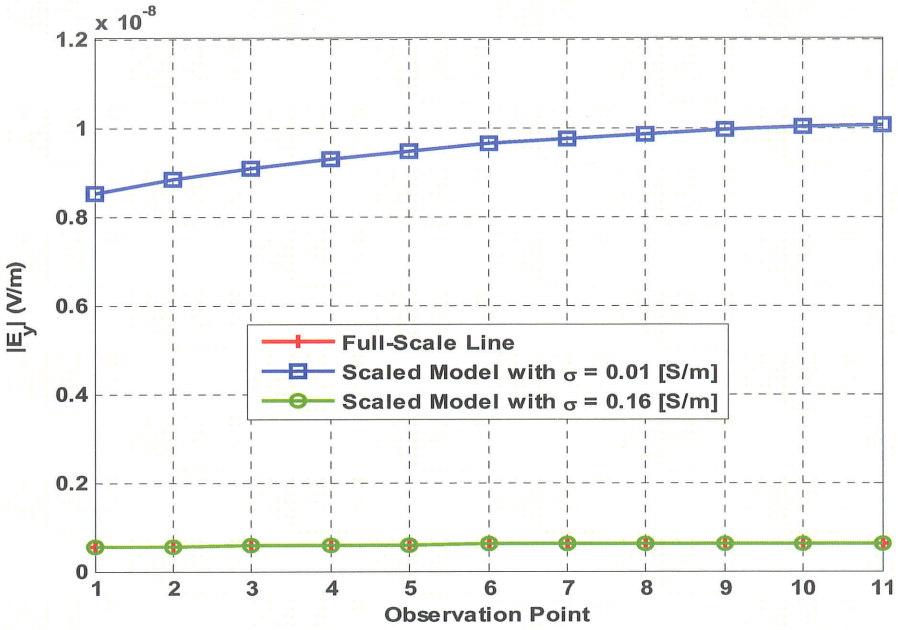

Figure 5.51. The *y*-component of the electric field intensity for the full-scale and downscaled transmission systems, with and without scaling the ground's conductivity.

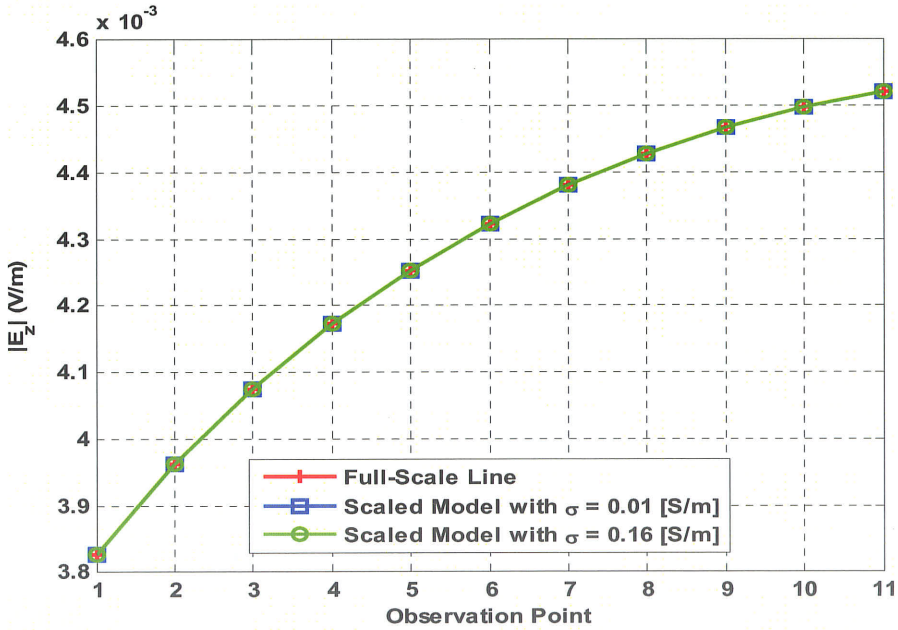

Figure 5.52. The *z*-component of the electric field intensity for the full-scale and downscaled transmission systems, with and without scaling the ground's conductivity.

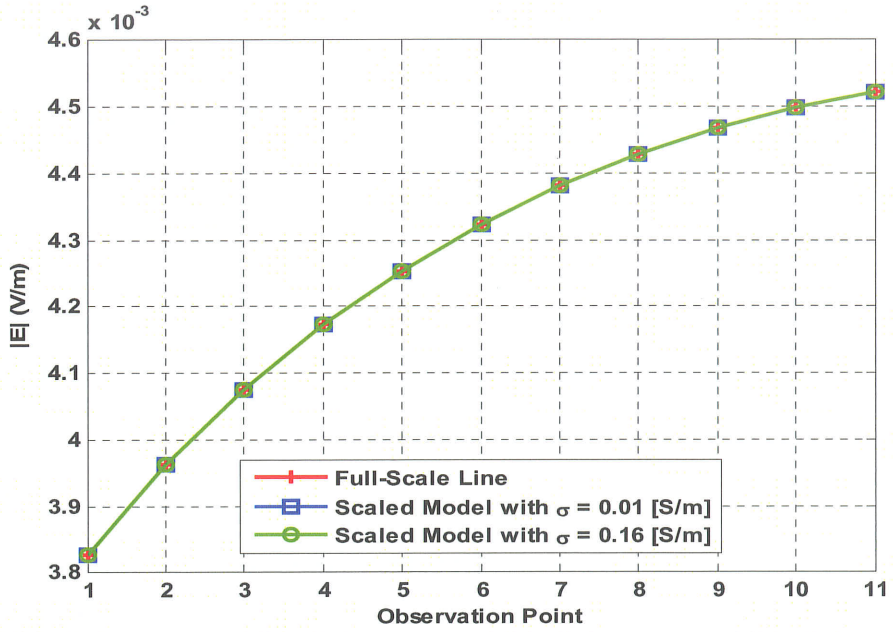

Figure 5.53. The magnitude of the electric field intensity for the full-scale and downscaled transmission systems, with and without scaling the ground's conductivity.

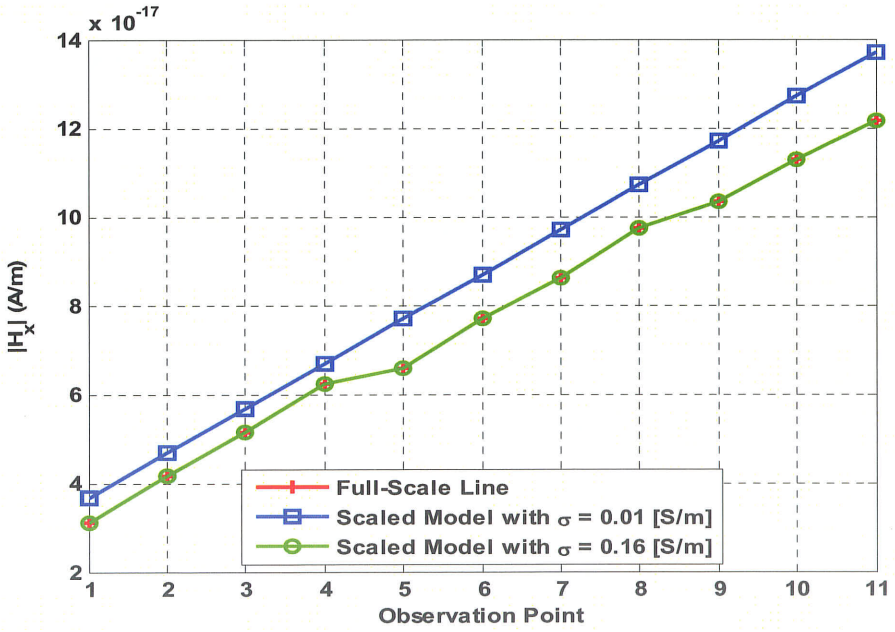

Figure 5.54. The *x*-component of the magnetic field intensity for the full-scale and downscaled transmission systems, with and without scaling the ground's conductivity.

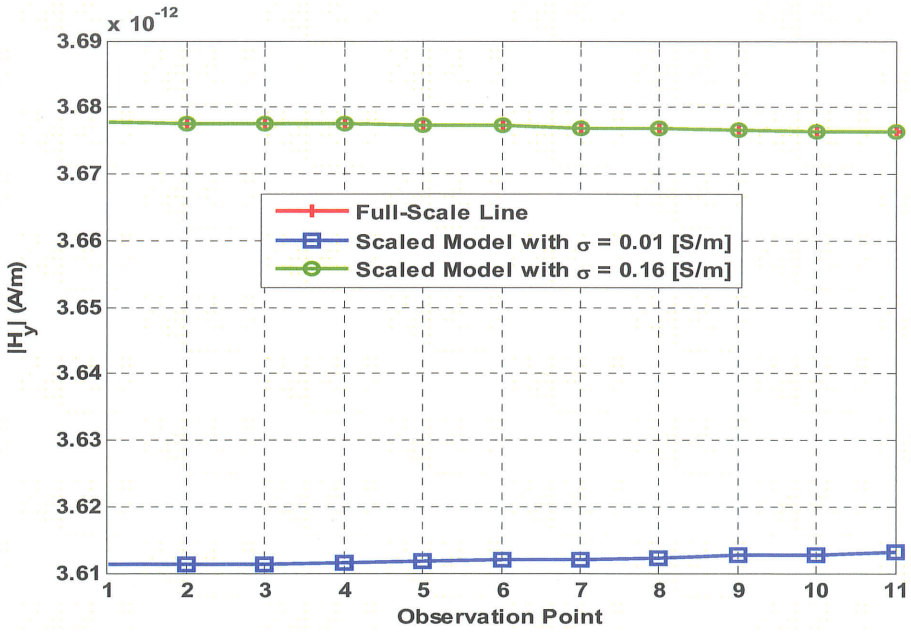

Figure 5.55. The *y*-component of the magnetic field intensity for the full-scale and downscaled transmission systems, with and without scaling the ground's conductivity.

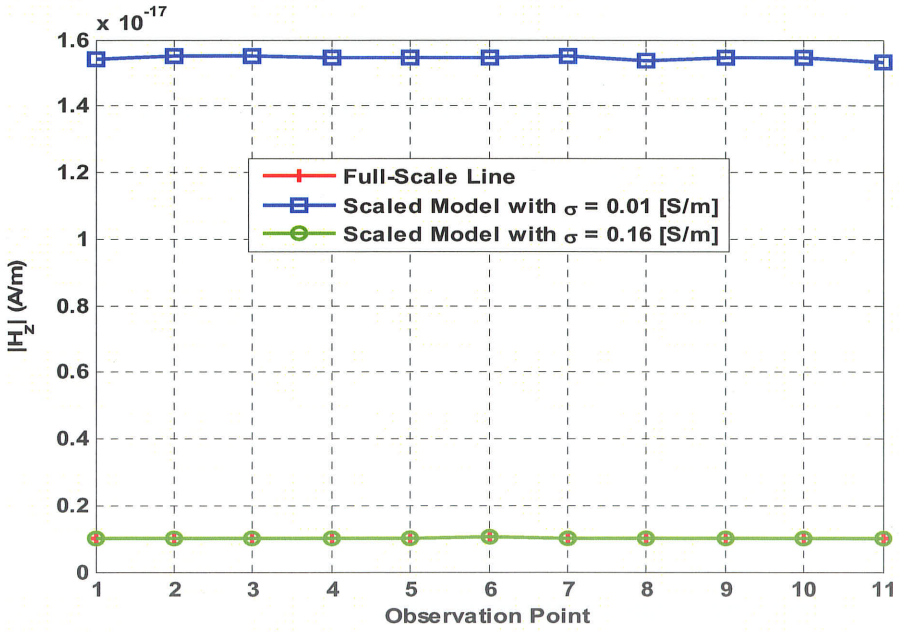

Figure 5.56. The *z*-component of the magnetic field intensity for the full-scale and downscaled transmission systems, with and without scaling the ground's conductivity.

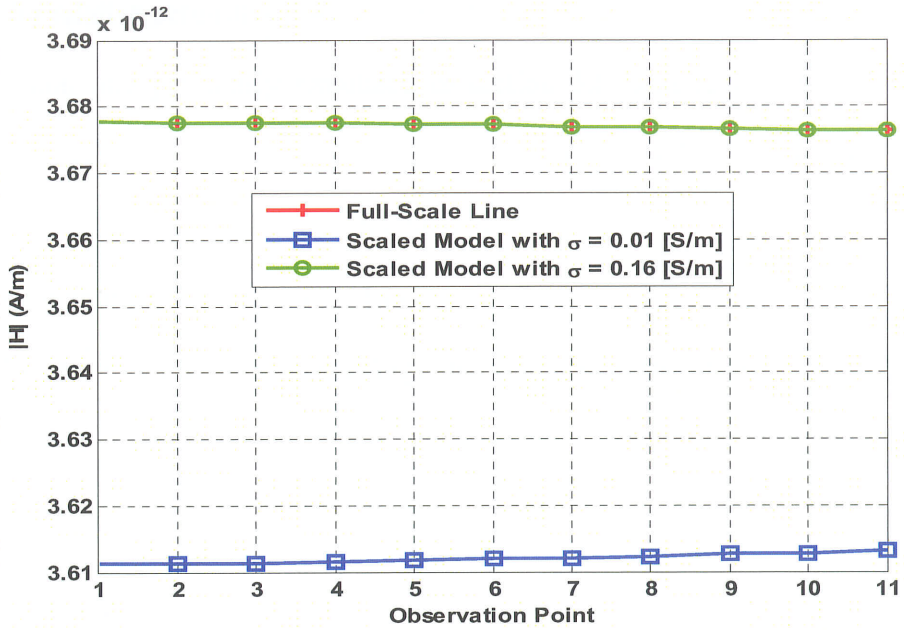

Figure 5.57. The magnitude of the magnetic field intensity for the full-scale and downscaled transmission systems, with and without scaling the ground's conductivity.

The results show that for obtaining more accurate results, we need to use a different material for the ground plane in the scaled model. The scale factor chosen for this example was 1/16. If we want to have a smaller model, the line will be closer to the ground plane and consequently, the effect of finite conductivity of the ground will become more significant. In that case, the error due to not scaling the conductivity of the ground becomes considerable.

5.10 The Effect of Relative Permittivity of the Ground

The only parameter which was not scaled in the example presented in the previous section was the relative permittivity of the ground, ϵ_r. To find out whether any change in the value of ϵ_r has any impact on the value of electric and magnetic fields, five different

values for relative permittivity, $\epsilon_r = 1$, 5, 10, 15 and 20, were chosen for the ground. The transmission line previously simulated in section 5.6 is simulated with these distinct values for ground's relative permittivity. The line is excited by the transient waveform shown earlier in Figure 5.28. The conductivity of the ground is fixed at $\sigma = 0.1$ [S/m]. The time-domain waveforms of the field vectors' magnitude are presented in Figures 5.58 and 5.59. As it can be seen, the change in the shape of the electric and magnetic field waveforms is insignificant. However, the maximum value of the electric and magnetic fields depend on the value of relative permittivity. The change in the maximum value of the *xyz* components and the magnitude of the field vectors with respect to the case of $\epsilon_r = 1$ are presented in the percentile format in Tables 5.11 and 5.12.

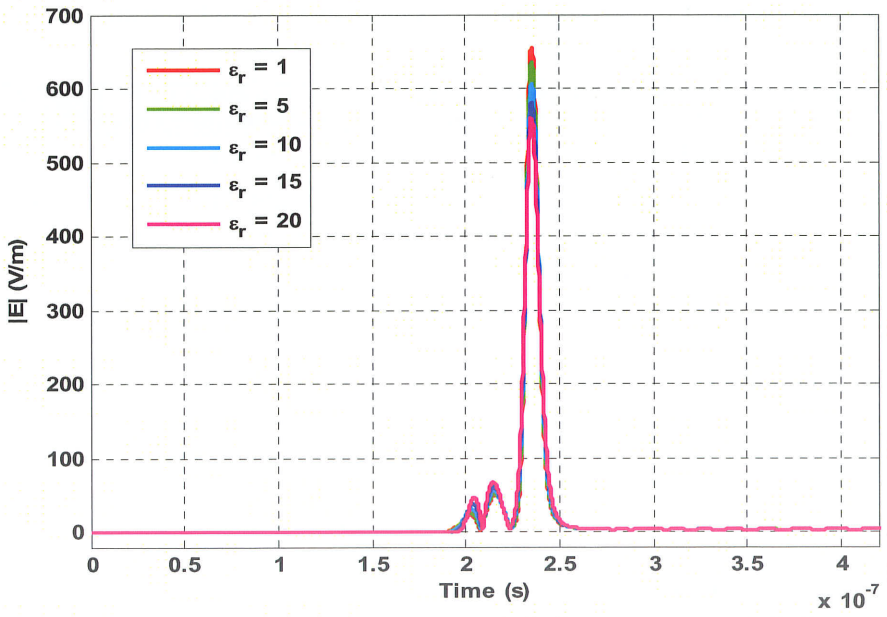

Figure 5.58. Time-domain waveform of the magnitude of the electric field intensity, calculated at (x = 10 m, y = 10 m, z = 0) for different values of ground's relative permittivity.

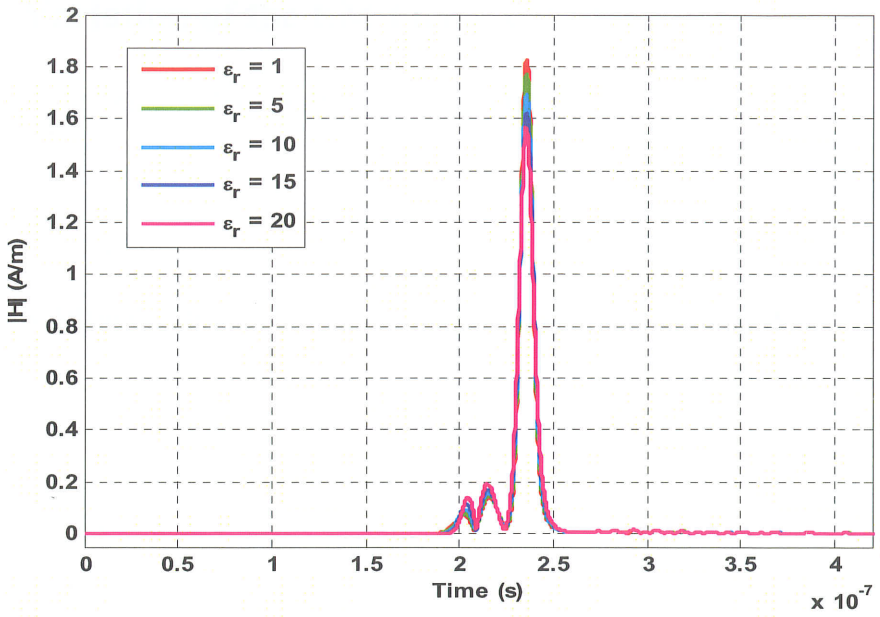

Figure 5.59. Time-domain waveform of the magnitude of the magnetic field intensity, calculated at (x = 10 m, y = 10 m, z = 0) for different values of ground's relative permittivity.

Table 5.11. Variation of the electric field intensity with the relative permittivity, compared with the case of $\epsilon_r = 1$.

	$E_{x_{max}}$	$E_{y_{max}}$	$E_{z_{max}}$	$\lvert\mathbf{E}_{max}\rvert$
$\epsilon_r = 5$	4.33%	1.48%	4.00%	2.77%
$\epsilon_r = 10$	13.2%	6.03%	12.1%	7.28%
$\epsilon_r = 15$	22.6%	11.6%	22.7%	11.2%
$\epsilon_r = 20$	31.3%	17.3%	36.8%	14.3%

Table 5.12. Variation of the magnetic field intensity with the relative permittivity, compared with the case of $\epsilon_r = 1$.

	$H_{x_{max}}$	$H_{y_{max}}$	$H_{z_{max}}$	$\lvert\mathbf{H}_{max}\rvert$
$\epsilon_r = 5$	6.96×10^{-1}%	2.77%	3.37×10^{-1}%	2.77%
$\epsilon_r = 10$	2.71%	7.22%	1.59%	7.21%
$\epsilon_r = 15$	5.35%	11.0%	3.44%	11.0%
$\epsilon_r = 20$	8.21%	14.0%	5.60%	14.0%

5.11 Variation of the EM Fields with Height of the Line

Overhead transmission lines with different voltage levels and in different locations are built with different heights. To see how any change in the height of the transmission line affects the electromagnetic field levels in the vicinity of the line, the transmission line previously simulated in section 5.6 is simulated with six distinct values for its height, h = 5 m, 10 m, 15 m, 20 m, 25 m, and 30 m. The line is excited by the transient waveform shown earlier in Figure 5.28. The time-domain electric and magnetic fields are calculated using complex image theory. The conductivity and relative permittivity of the ground are respectively fixed at σ = 0.1 [S/m] and ϵ_r = 4. The field waveforms calculated at the ground level in the middle of the line are shown in Figures 5.60 and 5.61.

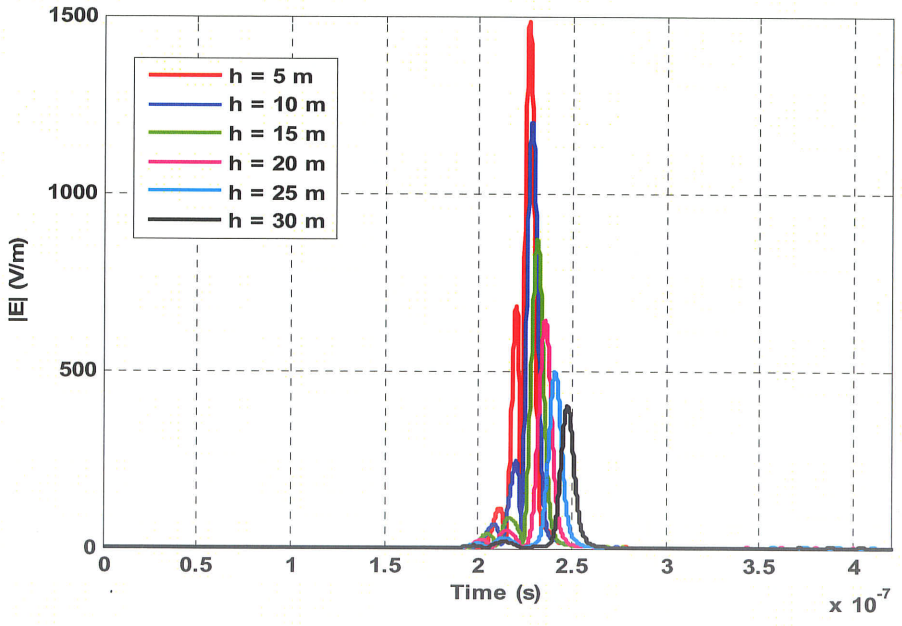

Figure 5.60. The magnitude of the electric field intensity at (x = 10 m, y = 10 m, z = 0) for different transmission line heights.

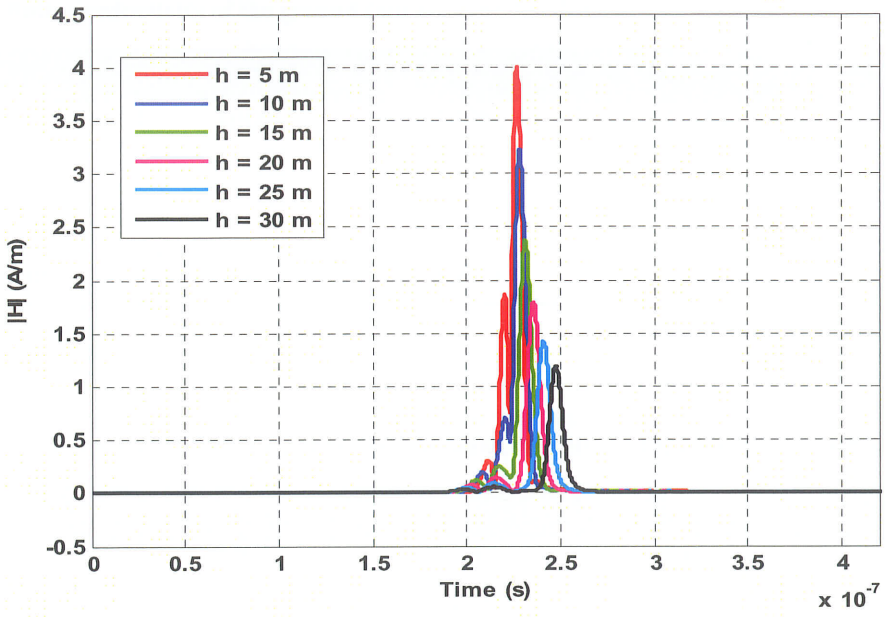

Figure 5.61. The magnitude of the magnetic field intensity at (x = 10 m, y = 10 m, z = 0) for different transmission line heights.

Figures 5.60 and 5.61 show that the magnitude of the electric and magnetic field intensity vectors increases drastically when the observation point gets close to the line.

In Chapter 3, by making use of the complex image theory, analytical expressions for electromagnetic fields were presented so that the effect of the finite conductivity of the ground is taken into account. In the downscaling example presented in this chapter, it was stated that the effect of finite conductivity of the ground becomes more considerable when the line gets closer to the ground. To support this claim, the effect of finite conductivity of the ground ($\sigma = 0.1$ [S/m]) is compared for four different cases, $h = 5$ m, 10 m, 15 m, and 20 m. The amount of error produced by the PEC ground assumption in the maximum value of electric and magnetic field components are specified in Tables 5.13 and 5.14.

Table 5.13. The percentage of error in calculation of the electric field intensity due to not taking the finite conductivity of the ground into account, for different transmission line heights.

	$E_{x_{max}}$	$E_{y_{max}}$	$E_{z_{max}}$	$\|\mathbf{E}_{max}\|$
h = 5 m	100%	100%	51.5%	51.9%
h = 10 m	100%	100%	26.7%	27.3%
h = 15 m	100%	100%	9.40%	9.98%
h = 20 m	100%	100%	2.64%	2.02%

Table 5.14. The percentage of error in calculation of the magnetic field intensity due to not taking the finite conductivity of the ground into account, for different transmission line heights.

	$H_{x_{max}}$	$H_{y_{max}}$	$H_{z_{max}}$	$\|\mathbf{H}_{max}\|$
h = 5 m	100%	51.5%	100%	51.6%
h = 10 m	100%	25.9%	100%	26.0%
h = 15 m	100%	8.10%	100%	8.12%
h = 20 m	100%	4.03%	100%	4.02%

From the results shown in Tables 5.13 and 5.14, it is clear that PEC ground assumption brings significant computational error in the calculation of the electric and magnetic field intensities. Moreover, the results show that the effect of finite conductivity of the ground on the electric and magnetic field values becomes more significant as the line gets close to the ground plane. Therefore, careful consideration should be taken in choosing the ground surfaces with appropriately scaled conductivity in downscale modeling studies.

Chapter 6

Concluding Remarks

6.1 Overview

Calculation of the electric and magnetic fields in the vicinity of power transmission lines has been subject of research and study for more than a century. In this thesis, the large body of research on this issue was reviewed and divided into two categories. In the first category, the ground is treated as a perfectly-conductive surface, while the second category is based on the assumption of a finitely-conductive ground. To solve this problem, use was made of the Hertzian dipole technique introduced in Chapter 2. In this technique, the transmission line is decomposed into a large number of small dipoles. The length of each dipole is so small that the current passing through each dipole can be assumed to be constant along its length at any time. Also, the distance between any dipole and the observation point is much larger than the length of each dipole.

Using the dipole technique, the problem of calculating electromagnetic radiation from power lines was reduced to the problem of field calculation due to a horizontal dipole. Three analytical approaches were applied to solve this problem. In the first approach, the

exact analytical expressions for the electric and magnetic fields in the space due to an infinitesimal dipole in free-space were re-derived. The combination of this method and image theory enabled us to formulate the electromagnetic field expressions associated with an overhead transmission line located above perfectly-conductive ground.

The other two approaches implemented in this thesis were the frequency-domain formulations proposed by R. W. P. King and P. R. Bannister. Both of these approaches lead to approximate formulas for the electric and magnetic fields in the vicinity of a horizontal dipole located above lossy ground. The method proposed by King solves the transformed form of frequency-domain Maxwell's equations subject to the specific boundary conditions. However, Bannister tries to formulate the same problem using the complex image theory by approximating the Sommerfeld integrals. The restriction on the application of these techniques is on the proportion of the wave number in the air and the ground. While Bannister's method is only limited to the cases were $k_1^2 \ll |k_2^2|$, King's approach puts another limitation on the applicability of the formulas, asking for $|k_2\rho|$ to be bigger than one; where k_1 and k_2 are the wave numbers in the ground and air and ρ is the radial distance between the source and the observation point.

These two frequency-domain approaches do not provide valid answer for the zero-frequency component of the electromagnetic fields. Hence, to overcome this deficiency, a set of simplified formulas for the extremely low frequencies derived by R. G. Olsen was employed to calculate the electrostatic fields due to the zero-frequency component of the excitation waveform.

Most of the previous works dealing with the problem of radiation from transmission lines treat the overhead line as a straight wire. Neglecting the sag of the conductor leads to computational error, especially in the transient analysis. To take the effect of sag of the line into account, an algorithm was suggested to approach this problem. In the proposed technique, a parabola is assumed to represent the catenary of the line. The dipole technique is then applied to decompose the transmission line into small segments. Each segment is then broken into horizontal and vertical components. The contribution of each segment is found using the frequency-domain approaches reviewed in Chapter 3. In this technique, it is assumed that the existence of sag does not change the current distribution along the line significantly.

The last step in any theoretical study is validation of the obtained formulas experimentally. Performing the experiments on a full-scale transmission system is costly. That's why scale modeling is a popular verification tool in power system analysis. Nonetheless, geometrical scaling of physical dimensions demands scaling of all the temporal and physical parameters such as field intensities, currents, and voltages with appropriate scale factors. Chapter 4 of this thesis was completely devoted to deriving such scale factors. By making use of the linearity of Maxwell's equations and by applying the similarity theory, scaling factors for all the parameters encountered in the transient electromagnetic analysis were derived analytically.

6.2 Summary of the Simulation Results

NEC-4, which is a numerical software package based on method of moments, was employed to verify the validity of the methods reviewed in Chapters 2 and 3. The results

show that the magnitude of electric and magnetic fields calculated using NEC, match with those calculated by applying King's formulation and complex image theory.

Next, using the exact analytical approach explained in Chapter 2, the variation of the electromagnetic field waveforms as the observation point gets far from the transmission line was studied in detail. It was observed that the expressions for the electromagnetic fields include three main components, each dominating in a different distance region.

In many of the studies regarding the problem of radiation from power transmission and distribution apparatus, the ground is treated as a perfect conductor. To study the amount of error brought into calculations by assuming perfectly-conductive ground, the effect of ground loss was analyzed by use of example. According to the simulation, the magnitude of the electric and magnetic fields are altered drastically when the value of the ground's conductivity is changed. Also, the transversal component of electromagnetic fields (x component) changes significantly with any change in the conductivity of the ground.

Using the segmentation technique reviewed in Chapter 2, the impact of conductor's sag on the electric and magnetic fields was studied in detail. It was observed that ignoring the existence of sag in the calculation brings error into the calculation of electric and magnetic fields. Interestingly, the error in the calculation of the fields increases when the observation point gets far from the line. This observation was justified due to the fact that the electric and magnetic fields associated with a horizontal dipole vanish much faster with the distance than those of a vertical dipole. Therefore, the vertical components of the

segmented line play a major role in determining the value of the electric and magnetic fields in the far-field region.

To obtain the full waveform of the electromagnetic fields aroused by a transient excitation such as lightning or switching transient phenomena, the current distribution along the line should be available. Current and voltage values at any point of the line can be obtained by solving Telegrapher's equations, if the excitation source is known. In this thesis, a modified finite-difference time-domain (MFDTD) technique was employed to solve Telegrapher's equations. Merging the MFDTD method with the dipole technique enables us to find the transient currents, voltages and electromagnetic fields after any kind of perturbation, given that the excitation source is known. As an example of this application, a multi-conductor transmission line was simulated using MFDTD technique and the obtained current distribution along the transmission line was extracted to find the *xyz* components of electric and magnetic field waveforms.

To verify the scaling factor table derived in Chapter 4, a full-scale transmission line and its reduced-scale model were simulated in NEC-4. The results of this simulation showed that in order to increase the accuracy of downscale modeling, a conducting surface with a much higher conductivity value than that of the original ground plane should be employed. In this case, the measurements obtained from the reduced-scale model can be extended to predict the behaviour of the full-scale transmission system.

6.3 Future Work

The theoretical work done in this project can be utilized for prediction of the electromagnetic fields associated with overhead transmission lines in the transient or

steady-state modes. Although the theoretical expressions were verified using the numerical electromagnetic code (NEC), the impact of experimental and physical parameters affecting the response of the transmission system, such as humidity, wind, and corona, were never taken into account. To have a clear knowledge on the extent of effect of such parameters, fabrication of a downscaled model and performing experimental measurements on this model is necessary. The experimental measurement can then be compared with the numerical and theoretical results. Using the scale factor database presented in Chapter 4, experimental results can be employed to predict the behaviour of the full-scale transmission system.

The whole focus of this work was on the overhead transmission system. A similar procedure followed in this thesis can be employed to find the electromagnetic behaviour of buried power cables. This can be achieved by applying minor changes in the field expressions derived in Chapter 3. The combination of the new set of formulas and dipole technique will lead to derivation of the electric and magnetic field values associated with power cables at any point in the ground or air. As a result, the effects of the energized electric cables on the environment and adjacent equipment can be studied.

The effect of line insulation and stratified ground on the emitted fields from the power transmission lines were neglected in this thesis. To find out the impact of shielding on the transmission line radiation, the set of formulas derived by King can be extended to include the effect of shielding on the emitted fields. Moreover, the electromagnetic effect of a multi-layered ground can be taken into consideration by modifying the complex image theory.

In the proposed algorithm for calculation of the radiated fields due to a sagged conductor, it was assumed that the existence of sag does not change the current distribution along the line. Although this sounds to be a legitimate assumption, the MFDTD technique used in this thesis can be modified to predict the current distribution along a sagged transmission line.

Finally, the procedure explained in this work can be used to study the electromagnetic effects of the power transmission lines on other instruments in the vicinity of the transmission system. As an important application, the coupling between power lines and communication lines, pipelines, and railroads can be studied. Also, the theoretical results presented in this thesis can be extended to find the fields emitted from other power system apparatus such as high voltage substations, grounding systems, and power electronic converters. Moreover, the health issues associated with power transmission lines in the low- and high-frequency ranges can be studied using the theoretical and numerical results derived in Chapters 3 and 5.

References

[1] A. Sommerfeld, "Propagation of Waves in Wireless Telegraphy", *Annalen der Physik*, vol. 28, pp. 665-737, 1909.

[2] A. Sommerfeld, "Propagation of Waves in Wireless Telegraphy", *Annalen der Physik*, vol. 81, pp. 1135-1153, 1926.

[3] C. A. Balanis, *Antenna Theory–Analysis and Design*, John Wiley & Sons, Hoboken, New Jersey, USA, 2005.

[4] M. Rubinstein and M. A. Uman, "Methods for Calculating the Electromagnetic Fields from a Known Source Distribution: Application to Lightning", *IEEE Transaction on Electromagnetic Compatibility*, vol. 31, no. 2, pp. 183-189, May 1989.

[5] M. A. Uman, D. K. McLain, and E. P. Krider, "The Electromagnetic Radiation from a Finite Antenna", *American Journal of Physics*, vol. 43, pp. 33-38, January 1975.

[6] M. Rubinstein and M. A. Uman, "Transient Electric and Magnetic Fields Associated with Establishing a Finite Electrostatic Dipole, Revisited" *IEEE Transaction on Electromagnetic Compatibility,* vol. 33, no. 4, pp. 312-320, November 1991.

[7] M. J. Master and M. A. Uman, "Transient Electric and Magnetic Fields Associated with Establishing a Finite Electrostatic Dipole", *American Journal of Physics,* vol. 51, no. 2, pp. 118-126, February 1983.

[8] U. Reggiani, A. Massarini, L. Sandrolini, M. Ciccoto, X. Liu, D. W. P. Thomas, and C. Christopoulos, "Experimental Verification of Predicted Electromagnetic Fields Radiated by Straight Interconnect Cables Carrying High-Frequency Currents", *Proceeding of IEEE Bologna PowerTech Conference*, Bologna, Italy, June 2003.

[9] E. T. Pereira, D. W. P. Thomas, A. F. Howe, and C. Christopoulos, "Computation of Electromagnetic Switching Transients in a Substation", *International Conference on Computation in Electromagnetics*, pp. 331-334, November 1991.

[10] N. Ari and W. Blumer, "Transient Electromagnetic Fields Due to Switching Operations in Electric Power Systems", *IEEE Transaction on Electromagnetic Compatibility*, vol. EMC-29, no. 3, August 1987.

[11] P. R. Bannister, "New Formulas for HED (Horizontal Electric Dipole), HMD (Horizontal Magnetic Dipole), VED (Vertical Electric Dipole), VMD (Vertical Magnetic Dipole) Subsurface to Subsurface Propagation", *NUSC Technical Report 6881*, Naval Underwater Systems Center, New London, CT, January 1984.

[12] P. R. Bannister, "Applications of Complex Image Theory", *Radio Science*, vol. 21, no. 4, pp. 605-616, August 1986.

[13] P. R. Bannister, "Image-Theory Electromagnetic Fields of Horizontal Dipole Antennas in Presence of Conducting Half-Space", *NUSC Technical Report 6511*, Naval Underwater Systems Center, New London, CT, September 1981.

[14] P. R. Bannister, "Extension of Finitely Conducting Earth-Image Theory Results to Any Range", *NUSC Technical Report 6885*, Naval Underwater Systems Center, New London, CT, January 1984.

[15] P. R. Bannister, "Summary of Image Theory Expressions for the Quasi-Static Fields of Antennas at or above the Earth's Surface", *Proceeding of IEEE*, vol. 67, no. 7, pp. 1001-1008, July 1979.

[16] R. W. P. King, M. Owens, and T.T. Wu, *Lateral Electromagnetic Waves*, Springer, New York, USA, 1992.

[17] R. W. P. King, "The Electromagnetic Field of a Horizontal Electric Dipole in the Presence of a Three-Layered Region", *Journal of Applied Physics*, vol. 69, pp. 7987-7995, June 1991.

[18] R. W. P. King, "The Electromagnetic Field of a Horizontal Electric Dipole in the Presence of a Three-Layered Region: Supplement", *Journal of Applied Physics*, vol. 74, pp. 4845-4848, October 1993.

[19] R. W. P. King and T. T. Wu, "The Complete Electromagnetic Field of a Three-Phase Transmission Line Over the Earth and Its Interaction with the Human Body", *Journal of Applied Physics,* vol. 78, pp. 668-683, July 1995.

[20] R. G. Olsen, "Power Transmission Line Electromagnetics", *IEEE Antennas and Propagation Magazine*, vol. 36, no. 6, pp. 7-16, December 1996.

[21] R. G. Olsen and P. S. Wong, "Characteristics of Low Frequency Electric and Magnetic Fields in the Vicinity of Electric Power Lines", *IEEE Transaction on Power Delivery*, vol. 7, no. 4, pp. 2046-2055, October 1992.

[22] J. Burke, "Numerical Electromagnetic Code (NEC-4)–Method of Moments", *User's Manual*, Lawrence Livermore National Laboratory, January 1992.

[23] B. Kordi, J. Lo Vetri, and G. E. Bridges, "Finite-Difference Analysis of Dispersive Transmission Lines within a Circuit Simulator", *IEEE Transaction on Power Delivery*, vol. 21, no. 1, pp. 234-242, January 2006.

[24] B. Kordi, J. Lo Vetri, and G. Bridges, "Integration of an FDTD Analysis of Lossy Multiconductor Transmission Lines within a General-Purpose Circuit Simulator", *Proceeding of ANTEM Conference*, Ottawa, Canada, July 2004.

[25] A. V. Mamishev, R. D. Nevels, and B. D. Russel, "Effects of Conductor Sag on Spatial Distribution of Power Line Magnetic Field", *IEEE Transaction on Power Delivery*, vol. 11, no. 3, pp. 1571-1576, July 1996.

[26] R. Amiri, H. Hadi, and M. Marich, "The Influence of Sag in the Electric Field Calculation around High Voltage Overhead Transmission Lines", *Annual Report–Conference on Electrical Insulation and Dielectric Phenomena*, pp. 206-209, Kansas City, USA, October 2006.

[27] R. Frentzel, "Use of Similarity Relations in the Analysis of Lightning-Induced Transient Phenomena", *European Transaction on Electrical Power*, vol. 7, no. 3, pp. 173-177, June 1997.

[28] I. A. Metwally, F. H. Heidler, and W. J. Zischank, "Magnetic Fields and Loop Voltages Inside Reduced- and Full-Scale Structures Produced by Direct

Lightning Strikes", *IEEE Transaction on Electromagnetic Compatibility*, vol. 48, no. 2, May 2006.

[29] A. Piantini, J. M. Janiszewski, A. Borghetti, C. A. Nucci, and M. Paolone, "A Scale Model for the Study of the LEMP Response of Complex Power Distribution Networks", *IEEE Transaction on Power Delivery*, vol. 22, no. 1, January 2007.

[30] D. E. Thomas, C. M. Wiggins, F. S. Nickel, C. D. Ko, and S. E. Wright, "Prediction of Electromagnetic Field and Current Transients in Power Transmission and Distribution Systems", *IEEE Transaction on Power Delivery*, vol. 4, no. 1, pp. 744-755, January 1989.

[31] R. S. Shi, A. Darcherif, and J. C. Sabonnadiere, "Computation of Transient Electromagnetic Fields Radiated by a Transmission Line: An Exact Model", *IEEE Transaction on Magnetics*, vol. 31, no. 4, pp. 2423-2431, July 1995.

[32] R. S. Shi, J. C. Sabonnadiere, and A. Darcherif, "An Exact Analytical Model for Predicting Electromagnetic Fields Produced by Current Transients", *Journal of Physics III France*, vol. 2, pp. 1473-1477, August 1992.

[33] B. Nekhoul and R. Feuilet, "A New Method for Calculating the Transient Electromagnetic Field Radiated by a Power Transmission Line", *Proceeding of Ninth International Conference on Electromagnetic Compatibility*, pp. 143-147, Manchester, UK, September 1994.

[34] M. Melit, B. Nekhoul, N. Boudjerda, K. Kerroum, and K. Elkhamalichi Drissi, "Calculating of the Transient Electromagnetic Fields Emitted by Power

Electronic Converters Using the Hybrid Approach", *Book of Abstracts–EUROEM Conference*, Hamburg, Germany, September 2008.

[35] B. Kordi, R. Moini, and F. Rachidi, "Modeling an Inclined Lightning Return Stroke Channel Using Antenna Theory", *Proceeding of International Zurich Symposium on Electromagnetic Compatibility*, Zurich, Switzerland, February 2001.

[36] K. Sarabandi, M. D. Casciato, and I. S. Koh, "Efficient Calculation of the Fields of a Dipole Radiating above an Impedance Surface", *IEEE Transaction on Antennas and Propagation*, vol. 50, no. 9, pp. 1222-1233, September 2002.

[37] J. R. Wait, "Low Frequency Radiation from a Horizontal Antenna over a Spherical Earth", *Canadian Journal of Physics*, vol. 34, pp. 586-595, 1956.

[38] J. R. Wait, "The Electromagnetic Fields of a Horizontal Dipole in the Presence of a Conducting Half-Space", *Canadian Journal of Physics*, vol. 39, pp. 1017-1028, 1961.

[39] J. R. Wait, "Transient Fields of a Vertical Dipole over a Homogeneous Curved Ground", *Canadian Journal of Physics*, vol. 34, pp. 27-35, 1956.

[40] J. R. Wait, *Electromagnetic Waves in Stratified Media*, The MacMillan Co., New York, U.S.A, 1962.

[41] A. Baños, *Dipole Radiation in the Presence of a Conducting Half-Space*, Pergamon Press Inc., New York, USA, 1966.

[42] P. R. Bannister, "Quasi-Static Fields of Dipole Antennas at the Earth's Surface", *Radio Science*, vol. 1, no. 11, pp. 1321-1330, November 1966.

[43] P. R. Bannister, "The Quasi-Near Fields of Dipole Antennas", *IEEE Transaction on Antennas and Propagation*, vol. AP-15, no. 5, pp. 618-626, September 1967.

[44] P. R. Bannister, "New Formulas that Extends Norton's Far-field Elementary Dipole Equations to the Quasi-Near Field Range", *NUSC Technical Report 6883*, Naval Underwater Systems Center, New London, CT, January 1984.

[45] P. R. Bannister, "Extension of Quasi-Static Range Finitely Conducting Earth-Image Theory Techniques to Other Ranges", *IEEE Transaction on Antennas and Propagation*, vol. AP-26, no. 3, pp. 507-508, May 1978.

[46] K. A. Norton, "The Propagation of Radio Waves over the Surface of the Earth and in the Upper Atmosphere", *Proceeding of Institution of Radio Engineers*, vol. 25, no. 9, pp. 1203-1236, September 1937.

[47] J. R. Wait and K. P. Spies, "On the Image Representation of the Quasi-Static Fields of a Line Current Source above the Ground", *Canadian Journal of Physics*, vol. 47, no. 23, pp. 2731-2733, December 1969.

[48] S. Zhang and J. Jin, *Computation of Special Functions*, Wiley-Interscience, New York, USA, 1996.

[49] P. R. Bannister, "Utilization of Image Theory Techniques in Determining the Mutual Coupling between Elevated Long Horizontal Line Sources", *Radio Science*, vol. 5, no. 11, pp. 1375-1381, November 1970.

[50] D. Metwally and S. F. Mahmoud, "Error Analysis of Image Representation for Sources Near to a Dissipative Earth", *IEEE Transactions on Antennas and Propagation*, vol. AP-30, no. 5, pp. 1005-1008, September 1982.

[51] S. F. Mahmoud and A. A. Mohsen, "Assessment of Image Theory for Field Evaluation over a Multilayer Earth", *IEEE Transactions on Antennas and Propagation*, vol. AP-33, no. 10, pp. 1054-1058, October 1985.

[52] A. Zeddam and P. Degauque, "Current and Voltage Induced on Telecommunication Cables by a Lightning Stroke", *Electromagnetics*, vol. 7, no. 3 & 4, pp. 541-564, 1987.

[53] N. A. Rahman, H. Hussain, I. Said, T. S. Jalal, and A. S. Farag, "Magnetic Fields from a Scaled Down Model Transmission Line–Simulation and Comparison to Measurements", *Proceeding of Asia-Pacific Conference on Electromagnetics*, pp. 147-151, December 2005.

[54] I. A. Metwally, "Triboelectrification of Oil Flow in Pipelines Adjacent to AC Power Transmission Lines", *Proceeding of International Symposium on Electrical Insulating Materials*, Japan, September 1998.

[55] T. Zhao, S. A. Sebo, and D. G. Kasten, "Calculation of Single Phase AC and Monopolar DC Hybrid Corona Effects", *IEEE Transaction on Power Delivery*, vol. 11, no. 3, July 1996.

[56] T. Zhao, J. Illan, J. M. Cohol, R. D. Hinton, S. A. Sebo, and D. G. Kasten, "Design, Construction and Utilization of a New Reduced-Scale Model for the study of Hybrid (AC and DC) Line Corona", *Proceeding of IEEE PES Transmission and Distribution Conference*, pp. 239-245, April 1994.

[57] I. A. Metwally, "Investigation of Corona Phenomenon for a Reduced-Scale Model of Hybrid AC and DC Lines", *Proceeding of IEEE Conference on*

Electrical Insulation and Dielectric Phenomena, San Francisco, pp. 610-613, October 1996.

[58] D. G. Kasten, S. A. Sebo, T. Zhao, L. E. Zaffanella, and B. A. Clairmont, "Corona Tests on Reduced-Scale Two-Conductor Hybrid Lines", *Annual Report–Conference on Electrical Insulation and Dielectric Phenomena*, pp. 624-629, October 1993.

[59] S. A. Sebo, D. G. Kasten, and T. Zhao, "Development of Reduced-Scale Line Modeling for the Study of Hybrid Corona", *Annual Report–Conference on Electrical Insulation and Dielectric Phenomena*, pp. 538-543, October 1993.

[60] A. Piantini and J. M. Janiszewski, "Lightning-Induced Voltages on Overhead Lines–Applications of the Rusck Model", *IEEE Transaction on Electromagnetic Compatibility*, vol. 51, no. 3, August 2009.

[61] A. Kern, F. Heidler, M. Seevers, and W. Zischank, "Magnetic Fields and Induced Voltages in Case of a Direct Strike–Comparison of Results Obtained from Measurements at a Scaled Building to Those of IEC 62305-4", *Journal of Electrostatics*, vol. 65, no. 5-6, pp. 379-385, 2007.

[62] M. Ishii, K. Michishita, and Y. Hongo, "Experimental Study of Lightning-Induced Voltage on an Overhead Wire over Lossy Ground", *IEEE Transaction on Electromagnetic Compatibility*, vol. 41, no. 1, pp. 39-45, February 1999.

[63] C. R. Paul, *Analysis of Multiconductor Transmission Lines*, Wiley-IEEE Press, New York, USA, October 2007.

[64] M. Ishii and Y. Baba, "Advanced Computational Methods in Lightning Performance–The Numerical Electromagnetic Code (NEC-2)," *Proceeding of IEEE PES Meeting,* Singapore, January 2000.

[65] R. K. Pokharel and M. Ishii, "Applications of Time-Domain Numerical Electromagnetic Code to Lightning Surge Analysis", *IEEE Transaction on Electromagnetic Compatibility*, vol. 49, no. 3, pp. 623-631, August 2007.

[66] R. K. Pokharel, M. Ishii, and Y. Baba, "Numerical Electromagnetic Analysis of Lightning-Induced Voltage over Ground of Finite Conductivity", *IEEE Transaction on Electromagnetic Compatibility*, vol. 45, no. 4, pp. 651-657, November 2003.

[67] Y. Baba and M. Ishii, "Characteristics of Electromagnetic Return-Stroke Models", *IEEE Transaction on Electromagnetic Compatibility*, vol. 45, no. 1, pp. 129-134, February 2003.

[68] P. Taheri, B. Kordi, and A. M. Gole, "Electric Fields Radiated by an Overhead Transmission Line over a Lossy Ground," *Proceeding of UPEC 2008*, Padova, Italy, September 2008.

[69] P. Taheri, B. Kordi, and A. Gole, "Transient Electromagnetic Fields Associated with a Power Transmission Line above a Lossy Ground", *Proceeding of ANTEM/URSI 2009*, Banff, Canada, February 2009.

[70] F. Heidler, J. M. Cvetic, and B. V. Stanic, "Calculation of Lightning Current Parameters," *IEEE Transaction on Power Delivery*, vol. 14, no. 2, pp. 399-404, April 1999.

Appendices

Appendix A

King's Formulation

This Appendix provides the mathematical calculations followed by King and Wu [A.1]-[A.3], leading to the electric and magnetic field expressions for a horizontal dipole above lossy ground.

A.1 Maxwell's Equations and Their Transforms

Consider the x-directed horizontal electric dipole shown in Figure A.1, located at $z = d$ on the z-axis. The wave numbers of the two regions are $k_i = \omega(\mu_0 \tilde{\epsilon}_i)^{1/2}$, where $\tilde{\epsilon}_i = \epsilon_i + j\,\sigma_i/\omega$ and $i = 1, 2$. It is assumed that both regions are nonmagnetic so that $\mu_1 = \mu_2 = \mu_0$. Maxwell's equations in the two regions are derived assuming $\exp(-j\omega t)$ time-dependence:

$$\nabla \times \mathbf{E}_i = j\omega \mathbf{B}_i, \tag{A.1}$$

and,

$$\nabla \times \mathbf{B}_i = \mu_0(-j\omega\tilde{\epsilon}_i \mathbf{E}_i + \hat{\mathbf{x}} J_x), \tag{A.2}$$

where,

$$J_x = \delta(x)\delta(y)\delta(z-d), \tag{A.3}$$

is the normalized volume density of current in the dipole. Equations (A.1) and (A.2) are to be solved for $\mathbf{E}_i$ and $\mathbf{B}_i$, subject to the following boundary conditions,

$$E_{1x}(x, y, 0) = E_{2x}(x, y, 0), \tag{A.4}$$

$$E_{1y}(x, y, 0) = E_{2y}(x, y, 0), \tag{A.5}$$

$$k_1 E_{1z}(x, y, 0) = k_2 E_{2z}(x, y, 0), \tag{A.6}$$

$$\mathbf{B_1}(x, y, 0) = \mathbf{B_2}(x, y, 0). \tag{A.7}$$

The translational invariance of the boundary in the x- and y-directions suggests the use of the transform

$$\mathbf{E}(x, y, z) = \frac{1}{(2\pi)^2} \int_{-\infty}^{\infty} \int_{-\infty}^{\infty} e^{j(\xi x + \eta y)} \bar{\mathbf{E}}(\xi, \eta, z) d\eta \, d\xi, \tag{A.8}$$

and a similar one for $\mathbf{B}(x, y, z)$.

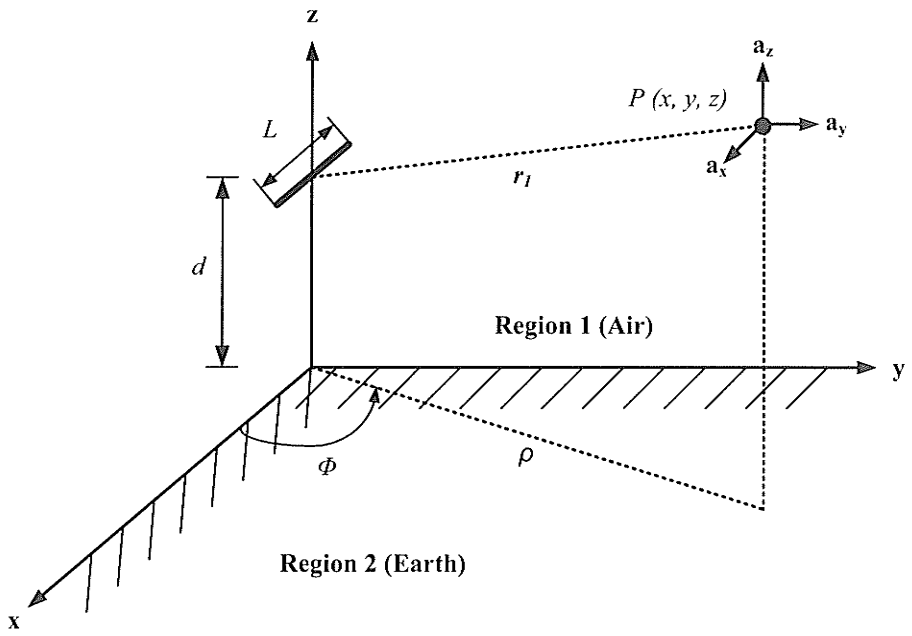

Figure A. 1. Geometry of an x-directed horizontal dipole, located on the z-axis above finitely-conductive ground.

The transformed form of $J_x(x,y,z)$ is

$$\bar{J}_x(\xi,\eta,z) = \delta(z-d). \tag{A.9}$$

The transformed Maxwell's equations in Cartesian coordinates are,

$$j\eta\bar{E}_{iz} - \frac{\partial}{\partial z}\bar{E}_{iy} = j\omega\bar{B}_{ix}, \tag{A.10}$$

$$\frac{\partial}{\partial z}\bar{E}_{ix} - j\xi\bar{E}_{iz} = j\omega\bar{B}_{iy}, \tag{A.11}$$

$$j\xi\bar{E}_{iy} - j\eta\bar{E}_{ix} = j\omega\bar{B}_{iz}, \tag{A.12}$$

$$j\eta\bar{B}_{iz} - \frac{\partial}{\partial z}\bar{B}_{iy} = -\frac{jk_i^2}{\omega}\bar{E}_{ix} + \mu_0\delta(z-d), \tag{A.13}$$

$$\frac{\partial}{\partial z}\bar{B}_{ix} - j\xi\bar{B}_{iz} = -\frac{jk_i^2}{\omega}\bar{E}_{iy}, \tag{A.14}$$

$$j\xi\bar{B}_{iy} - j\eta\bar{B}_{ix} = -\frac{jk_i^2}{\omega}\bar{E}_{iz}. \tag{A.15}$$

With these equations, the y- and z-components of both $\bar{\mathbf{E}}_i$ and $\bar{\mathbf{B}}_i$ can be expressed in terms of $\bar{E}_{ix}$ and $\bar{B}_{ix}$. The results are

$$\bar{E}_{iy} = \frac{1}{k_i^2-\xi^2}\left(-\xi\eta\bar{E}_{ix} + j\omega\frac{\partial}{\partial z}\bar{B}_{ix}\right), \tag{A.16}$$

$$\bar{E}_{iz} = \frac{1}{k_i^2-\xi^2}\left(j\xi\frac{\partial}{\partial z}\bar{E}_{ix} + \eta\omega\bar{B}_{ix}\right), \tag{A.17}$$

$$\bar{B}_{iy} = \frac{1}{k_i^2-\xi^2}\left(-\frac{jk_i^2}{\omega}\frac{\partial}{\partial z}\bar{E}_{ix} - \xi\eta\bar{B}_{ix}\right), \tag{A.18}$$

$$\bar{B}_{iz} = \frac{1}{k_i^2-\xi^2}\left(-\frac{k_i^2\eta}{\omega}\bar{E}_{ix} + j\xi\frac{\partial}{\partial z}\bar{B}_{ix}\right). \tag{A.19}$$

The substitution of (A.16)-(A.19) into (A.10) and (A.13) leads to the following ordinary differential equations for $\bar{E}_{ix}$ and $\bar{B}_{ix}$

$$\left(\frac{d^2}{dz^2}+\gamma_i^2\right)\bar{E}_{ix} = \frac{\omega\mu_0(k_i^2-\xi^2)}{jk_i^2}\delta(z-d), \tag{A.20}$$

$$\left(\frac{d^2}{dz^2}+\gamma_i^2\right)\bar{B}_{ix} = 0, \tag{A.21}$$

where,

$$\gamma_i^2 = k_i^2-\xi^2-\eta^2. \tag{A.22}$$

A.2 Solution of the Differential Equations

First consider the Equation (A.21) for $\bar{B}_{ix}$ with $i = 1$ and $z > 0$. The general solution in region 1, $z > 0$, is

$$\bar{B}_{1x} = C_1' e^{-j\gamma_1 z} + C_1 e^{j\gamma_1 z}, \tag{A.23}$$

where, from (A.22) with $k_1 = \beta_1 + j\alpha_1$,

$$\gamma_1 = (\beta_1^2-\alpha_1^2-\xi^2-\eta^2+2j\alpha_1\beta_1)^{1/2}. \tag{A.24}$$

When $\xi^2+\eta^2 > \beta_1^2-\alpha_1^2$,

$$\gamma_1 = j(\xi^2+\eta^2-\beta_1^2+\alpha_1^2)^{1/2}[f(p_1)-jg(p_1)], \tag{A.25}$$

where $p_1 = 2\alpha_1\beta_1/(\xi^2+\eta^2-\beta_1^2+\alpha_1^2)$ is positive and real, and $f(p_1) = \cosh\left(\frac{1}{2}\sinh^{-1}p_1\right)$ and $g(p_1) = \sinh\left(\frac{1}{2}\sinh^{-1}p_1\right)$. It follows that,

$$\begin{aligned}\pm j\gamma_1 z = {} & \mp z(\xi^2+\eta^2-\beta_1^2+\alpha_1^2)^{1/2}f(p_1) \\ & \pm jz(\xi^2+\eta^2-\beta_1^2+\alpha_1^2)^{1/2}g(p_1).\end{aligned} \tag{A.26}$$

Clearly, with $z > 0$, $\exp(-j\gamma_1 z) \longrightarrow \infty$ as $z \longrightarrow \infty$, which is an unacceptable solution. Therefore, $C_1' = 0$, and,

$$\bar{B}_{1x} = C_1 e^{j\gamma_1 z}; \qquad z \geq 0. \tag{A.27}$$

This solution was obtained for $\xi^2 + \eta^2 > \beta_1^2 - \alpha_1^2$; by continuity it also holds when $\xi^2 + \eta^2 < \beta_1^2 - \alpha_1^2$.

When the same sequence of steps is followed for region 2, $z < 0$, and the boundary condition $\bar{B}_{1x} = \bar{B}_{2x}$ at $z = 0$ is applied, it follows that,

$$\bar{B}_{2x} = C_1 e^{-j\gamma_2 z}; \qquad z < 0. \tag{A.28}$$

The differential equation (A.20) for $\bar{E}_{2x}$ is homogeneous and a solution is obtained just as for $\bar{B}_{2x}$. It is

$$\bar{E}_{2x} = C_2 e^{-j\gamma_2 z}; \qquad z < 0. \tag{A.29}$$

The δ-function on the right side of the Equation (A.20), makes the solution for $\bar{E}_{1x}$, $z > 0$, more complicated. The particular solution for the equation is,

$$\bar{E}_{1x_p} = -\frac{\omega\mu_0(k_1^2 - \xi^2)}{2\gamma_1 k_1^2} e^{j\gamma_1|z-d|}, \tag{A.30}$$

so that,

$$\bar{E}_{1x} = C'e^{-j\gamma_1 z} + Ce^{j\gamma_1 z} - \frac{\omega\mu_0(k_1^2 - \xi^2)}{2\gamma_1 k_1^2} e^{j\gamma_1|z-d|}; \qquad z \geq 0. \tag{A.31}$$

As in the solution (A.23) for $\bar{B}_{1x}$, the constant C' must vanish since $\exp(-j\gamma_1 z) \longrightarrow \infty$ as $z \longrightarrow \infty$. The boundary condition $\bar{E}_{1x} = \bar{E}_{2x}$ at $z = 0$ gives

$$C = C_2 + \frac{\omega\mu_0(k_1^2 - \xi^2)}{2\gamma_1 k_1^2} e^{j\gamma_1 d}, \tag{A.32}$$

so that,

$$\bar{E}_{1x} = C_2 e^{j\gamma_1 z} - \frac{\omega\mu_0(k_1^2 - \xi^2)}{j\gamma_1 k_1^2} e^{j\gamma_1 d} \sin\gamma_1 z; \qquad 0 \leq z \leq d, \tag{A.33}$$

$$\bar{E}_{1x} = \left(C_2 - \frac{\omega\mu_0(k_1^2 - \xi^2)}{j\gamma_1 k_1^2} \sin\gamma_1 d\right) e^{j\gamma_1 z}; \qquad d \leq z. \tag{A.34}$$

The solutions (A.27) and (A.28) for $\bar{B}_x$ and (A.29), (A.33), and (A.34) for $\bar{E}_x$ satisfy the boundary conditions $E_{1x} = E_{2x}$, $B_{1x} = B_{2x}$ at $z = 0$. The continuity of E_y, kE_z, B_y, and B_z remains to be assured. Since these four additional boundary conditions are not independent, only two need to be enforced in order to determine the arbitrary constants C_1 and C_2 in the formulas for $\bar{E}_x$ and $\bar{B}_x$. Specifically, the conditions $E_{2y} = E_{1y}$, $B_{2y} = B_{1y}$ at $z = 0$ lead to the following system of equations:

$$\begin{bmatrix} \left(\frac{\gamma_1}{k_1^2-\xi^2}+\frac{\gamma_2}{k_2^2-\xi^2}\right) & \left(\frac{1}{k_1^2-\xi^2}-\frac{1}{k_2^2-\xi^2}\right)\xi\eta \\ \left(\frac{1}{k_1^2-\xi^2}-\frac{1}{k_2^2-\xi^2}\right)\xi\eta & -\left(\frac{\gamma_1 k_1^2}{k_1^2-\xi^2}+\frac{\gamma_2 k_2^2}{k_2^2-\xi^2}\right) \end{bmatrix} \begin{bmatrix} C_1 \\ \frac{C_2}{\omega} \end{bmatrix} = \begin{bmatrix} 0 \\ \mu_0 e^{j\gamma_1 d} \end{bmatrix}. \tag{A.35}$$

With $\gamma_i^2 = k_i^2 - \xi^2 - \eta^2$ and extensive manipulation, the constants C_1 and C_2 are

$$C_1 = -\frac{\xi\eta(k_1^2-k_2^2)}{MN}\mu_0 e^{i\gamma_1 d}, \tag{A.36}$$

$$C_2 = -\frac{\gamma_1(k_2^2-\xi^2)+\gamma_2(k_1^2-\xi^2)}{MN}\omega\mu_0 e^{i\gamma_1 d}, \tag{A.37}$$

where

$$M \equiv \gamma_1 + \gamma_2; \qquad \text{and} \qquad N \equiv k_1^2\gamma_2 + k_2^2\gamma_1. \tag{A.38}$$

When these expressions are substituted in (A.27)-(A.29), (A.33), and (A.34), the solutions $\bar{B}_{ix}$ and $\bar{E}_{ix}$, $i = 1, 2$, are obtained. The further substitutions of $\bar{B}_{ix}$ and $\bar{E}_{ix}$ in (A.16)-(A.19) provide $\bar{E}_{iy}, \bar{E}_{iz}, \bar{B}_{iy}$, and $\bar{B}_{iz}$.

A.3 Components of the Electromagnetic Fields

The six components of the electromagnetic field in cylindrical coordinates are obtained in the form of infinite integrals when the Fourier transforms derived in (A.8) are substituted. In region 1, the EM field components are given as

$$E_{1\rho} = -\frac{\omega\mu_0}{4\pi k_1^2}\cos\phi\left[\int_0^\infty\left(k_1^2 J_0(\lambda\rho)\right.\right.$$
$$\left.-\frac{\lambda^2}{2}[J_0(\lambda\rho)-J_2(\lambda\rho)]\right)\gamma_1^{-1}e^{j\gamma_1|z-d|}\lambda d\lambda$$
$$+\int_0^\infty\left(\frac{\gamma_1 Q}{2}[J_0(\lambda\rho)-J_2(\lambda\rho)]\right.$$
$$\left.\left.-\frac{k_1^2 P}{2\gamma_1}[J_0(\lambda\rho)+J_2(\lambda\rho)]\right)e^{j\gamma_1(z+d)}\lambda d\lambda\right], \tag{A.39}$$

$$E_{1\phi} = \frac{\omega\mu_0}{4\pi k_1^2}\sin\phi\left[\int_0^\infty\left(k_1^2 J_0(\lambda\rho)\right.\right.$$
$$\left.-\frac{\lambda^2}{2}[J_0(\lambda\rho)+J_2(\lambda\rho)]\right)\gamma_1^{-1}e^{j\gamma_1|z-d|}\lambda d\lambda$$
$$+\int_0^\infty\left(\frac{\gamma_1 Q}{2}[J_0(\lambda\rho)+J_2(\lambda\rho)]\right.$$
$$\left.\left.-\frac{k_1^2 P}{2\gamma_1}[J_0(\lambda\rho)-J_2(\lambda\rho)]\right)e^{j\gamma_1(z+d)}\lambda d\lambda\right], \tag{A.40}$$

$$E_{1z} = \frac{j\omega\mu_0}{4\pi k_1^2}\cos\phi\int_0^\infty\left(\pm e^{j\gamma_1|z-d|}+Qe^{j\gamma_1(z+d)}\right)J_1(\lambda\rho)\lambda^2 d\lambda, \tag{A.41}$$

$$B_{1\rho} = -\frac{\mu_0}{4\pi}\sin\phi\left[\pm\int_0^\infty J_0(\lambda\rho)e^{j\gamma_1|z-d|}\lambda d\lambda\right.$$
$$+\int_0^\infty\left(\frac{Q}{2}[J_0(\lambda\rho)+J_2(\lambda\rho)]\right.$$
$$\left.\left.-\frac{P}{2}[J_0(\lambda\rho)-J_2(\lambda\rho)]\right)e^{j\gamma_1(z+d)}\lambda d\lambda\right], \tag{A.42}$$

$$B_{1\phi} = -\frac{\mu_0}{4\pi}\cos\phi\left[\pm\int_0^\infty J_0(\lambda\rho)e^{j\gamma_1|z-d|}\lambda d\lambda\right.$$
$$+\int_0^\infty\left(\frac{Q}{2}[J_0(\lambda\rho)-J_2(\lambda\rho)]\right. \tag{A.43}$$
$$\left.\left.-\frac{P}{2}[J_0(\lambda\rho)+J_2(\lambda\rho)]\right)e^{j\gamma_1(z+d)}\lambda d\lambda\right],$$

$$B_{1z} = \frac{j\mu_0}{4\pi}\sin\phi\int_0^\infty\left(e^{j\gamma_1|z-d|}-Pe^{j\gamma_1(z+d)}\right)\gamma_1^{-1}J_1(\lambda\rho)\lambda^2 d\lambda. \tag{A.44}$$

where

$$P = \frac{\gamma_2-\gamma_1}{\gamma_1+\gamma_2}, \tag{A.45}$$

$$Q = \frac{k_1^2\gamma_2-k_2^2\gamma_1}{k_2^2\gamma_1+k_1^2\gamma_2}, \tag{A.46}$$

$$\rho = (x^2+y^2)^{1/2}, \tag{A.47}$$

$$\phi = \tan^{-1}\left(\frac{y}{x}\right), \tag{A.48}$$

and,

$$J_n(\lambda\rho) = \frac{j^{-n}}{2\pi}\int_0^{2\pi}e^{j\lambda\rho\cos\theta}e^{jn\theta}d\theta, \tag{A.49}$$

is the integral form of the Bessel functions.

This completes the formulation of the electromagnetic field at all points in the upper half-space when the source is a horizontal dipole with the unit electric moment located at a distance d from the boundary surface.

The integrals appeared in Equations (A.39)-(A.44) can be evaluated approximately with the condition $|k_2/k_1|^2 \gg 1$ or $|k_2| \geq 3k_1$. After complicated mathematical

manipulations, the six components of the electric and magnetic fields at any point (ρ, ϕ, z) in the air over the earth can be obtained as,

$$
\begin{aligned}
E_{1\rho}(\rho,\phi,z) = \frac{\omega\mu_0}{4\pi k_1}\cos\phi\Bigg\{ & e^{jk_1r_1}\left[\frac{2}{r_1^2}+\frac{2j}{k_1r_1^3}\right. \\
& \left.+\left(\frac{z-d}{r_1}\right)^2\left(\frac{jk_1}{r_1}-\frac{3}{r_1^2}-\frac{3j}{k_1r_1^3}\right)\right] \\
& -e^{jk_1r_2}\left[\frac{2}{r_2^2}+\frac{2j}{k_1r_2^3}+\left(\frac{z+d}{r_2}\right)^2\left(\frac{jk_1}{r_2}-\frac{3}{r_2^2}-\frac{3j}{k_1r_2^3}\right)\right. \\
& -\frac{2k_1}{k_2}\left(\frac{z+d}{r_2}\right)\left(\frac{jk_1}{r_2}-\frac{1}{r_2^2}\right) \\
& \left.\left.+\frac{2k_1^2}{k_2^2}\left\{\frac{jk_1}{r_2}-\frac{1}{r_2^2}-\frac{j}{k_1r_2^3}-\frac{k_1^3}{k_2}\left(\frac{r_2}{\rho}\right)\left(\frac{\pi}{k_1r_2}\right)^{1/2}e^{-jP}F(P)\right\}\right]\right\},
\end{aligned}
\tag{A.50}
$$

$$
\begin{aligned}
E_{1\phi}(\rho,\phi,z) = -\frac{\omega\mu_0}{4\pi k_1}\sin\phi\Bigg(& e^{jk_1r_1}\left(\frac{jk_1}{r_1}-\frac{1}{r_1^2}-\frac{j}{k_1r_1^3}\right) \\
& -e^{ik_1r_2}\left(\frac{jk_1}{r_2}-\frac{1}{r_2^2}-\frac{j}{k_1r_2^3}\right) \\
& -e^{jk_1r_2}\left\{-\frac{2k_1}{k_2}\left(\frac{z+d}{r_2}\right)\left(\frac{jk_1}{r_2}-\frac{1}{r_2^2}\right)\right. \\
& +\frac{2k_1^2}{k_2^2}\left[\frac{2}{r_2^2}+\frac{2j}{k_1r_2^3}+\left(\frac{z+d}{r_2}\right)^2\left(\frac{jk_1}{r_2}-\frac{3}{r_2^2}-\frac{3j}{k_1r_2^3}\right)\right] \\
& \left.+\frac{2jk_1^4}{k_2^3\rho}\left(\frac{r_2}{\rho}\right)^2\left(\frac{\pi}{k_1r_2}\right)^{1/2}e^{-jP}F(P)\right\}\Bigg),
\end{aligned}
\tag{A.51}
$$

$$E_{1z}(\rho,\phi,z) = \frac{\omega\mu_0}{4\pi k_1}\cos\phi\left\{-e^{jk_1r_1}\left(\frac{\rho}{r_1}\right)\left(\frac{z-d}{r_1}\right)\left(\frac{jk_1}{r_1}-\frac{3}{r_1^2}-\frac{3j}{k_1r_1^3}\right)\right.$$
$$+e^{jk_1r_2}\left(\frac{\rho}{r_2}\right)\left(\frac{z+d}{r_2}\right)\left(\frac{jk_1}{r_2}-\frac{3}{r_2^2}-\frac{3j}{k_1r_2^3}\right) \quad \text{(A.52)}$$
$$\left.-\frac{2k_1}{k_2}e^{jk_1r_2}\left[\left(\frac{\rho}{r_2}\right)\left(\frac{jk_1}{r_2}-\frac{1}{r_2^2}\right)-\frac{k_1^3}{k_2}\left(\frac{\pi}{k_1r_2}\right)^{1/2}e^{-jP}F(P)\right]\right\},$$

$$B_{1\rho}(\rho,\phi,z) = \frac{\mu_0}{4\pi}\sin\phi\left\{e^{jk_1r_1}\left(\frac{z-d}{r_1}\right)\left(\frac{jk_1}{r_1}-\frac{1}{r_1^2}\right)\right.$$
$$-e^{jk_1r_2}\left(\frac{z+d}{r_2}\right)\left(\frac{jk_1}{r_2}-\frac{1}{r_2^2}\right) \quad \text{(A.53)}$$
$$+\frac{2k_1}{k_2}e^{jk_1r_2}\left[\frac{2}{r_2^2}+\frac{2j}{k_1r_2^3}+\left(\frac{z+d}{r_2}\right)^2\left(\frac{jk_1}{r_2}-\frac{3}{r_2^2}-\frac{3j}{k_1r_2^3}\right)\right.$$
$$\left.\left.+\frac{jk_1^2}{k_2\rho}\left(\frac{r_2}{\rho}\right)^2\left(\frac{\pi}{k_1r_2}\right)^{1/2}e^{-jP}F(P)\right]\right\},$$

$$B_{1\phi}(\rho,\phi,z) = \frac{\mu_0}{4\pi}\cos\phi\left\{e^{jk_1r_1}\left(\frac{z-d}{r_1}\right)\left(\frac{jk_1}{r_1}-\frac{1}{r_1^2}\right)\right.$$
$$-e^{jk_1r_2}\left(\frac{z+d}{r_2}\right)\left(\frac{jk_1}{r_2}-\frac{1}{r_2^2}\right) \quad \text{(A.54)}$$
$$+\frac{2k_1}{k_2}e^{jk_1r_2}\left[\frac{jk_1}{r_2}-\frac{1}{r_2^2}-\frac{j}{k_1r_2^3}\right.$$
$$\left.\left.-\frac{k_1^3}{k_2}\left(\frac{r_2}{\rho}\right)\left(\frac{\pi}{k_1r_2}\right)^{1/2}e^{-jP}F(P)\right]\right\},$$

$$
\begin{aligned}
B_{1z}(\rho,\phi,z) \;=\; & -\frac{\mu_0}{4\pi}\sin\phi\left(e^{jk_1r_1}\left(\frac{\rho}{r_1}\right)\left(\frac{jk_1}{r_1}-\frac{1}{r_1^2}\right)\right. \\
& -e^{jk_1r_2}\left(\frac{\rho}{r_2}\right)\left(\frac{jk_1}{r_2}-\frac{1}{r_2^2}\right) \\
& +2e^{jk_1r_2}\left(\frac{\rho}{r_2}\right)\left\{\frac{k_1}{k_2}\left(\frac{z+d}{r_2}\right)\left(\frac{jk_1}{r_2}-\frac{3}{r_2^2}-\frac{3j}{k_1r_2^3}\right)\right. \\
& -\frac{k_1^2}{k_2^2}\left[\frac{1}{r_2^2}+\frac{3j}{k_1r_2^3}-\frac{3}{k_1^2r_2^4}\right. \\
& \left.\left.\left.+\left(\frac{z+d}{r_2}\right)^2\left(\frac{jk_1}{r_2}-\frac{6}{r_2^2}-\frac{15j}{k_1r_2^3}\right)\right]\right\}\right),
\end{aligned}
\tag{A.55}
$$

where,

$$
P \;=\; S\left(\frac{S+Z+D}{R}\right)^2, \tag{A.56}
$$

with,

$$
S \;=\; \frac{k_1^3r_2}{2k_2^2}; \qquad R \;=\; \frac{k_1^3\rho}{2k_2^2}; \qquad Z \;=\; \frac{k_1^2z}{2k_2}; \qquad D \;=\; \frac{k_1^2d}{2k_2}. \tag{A.57}
$$

And

$$
F(P) \;=\; \frac{1}{2}(1+j)-\int_0^P \frac{e^{jt}}{(2\pi t)^{1/2}}dt, \tag{A.58}
$$

where, the integral in the right hand side of Equation (A.58) is the Fresnel integral [A.4]. r_1 and r_2 are respectively the distance from the element of current and the perfect-image element to the point of observation; that is

$$
r_1 \;=\; [(x-x')^2+(y-y')^2+(z-z')^2]^{1/2}, \tag{A.59}
$$

$$
r_2 \;=\; [(x-x')^2+(y-y')^2+(z+z')^2]^{1/2}. \tag{A.60}
$$

The accuracy of representation increases as the value of $|k_2/k_1|$ grows larger. The derived equations give the complete electric and magnetic fields subject to the inequality $|k_2/k_1| \gg 1$ or $|k_2| \geq 3k_1$.

References

[A.1] R. W. P. King, M. Owens, and T.T. Wu, *Lateral Electromagnetic Waves*, Springer, New York, U.S.A., 1992.

[A.2] R. W. P. King, "The Electromagnetic Field of a Horizontal Electric Dipole in the Presence of a Three-Layered Region", *Journal of Applied Physics*, vol. 69, pp. 7987-7995, June 1991.

[A.3] R. W. P. King, "The Electromagnetic Field of a Horizontal Electric Dipole in the Presence of a Three-Layered Region: Supplement", *Journal of Applied Physics*, vol. 74, pp. 4845-4848, October 1993.

[A.4] S. Zhang and J. Jin, *Computation of Special Functions*, Wiley-Interscience, New York, USA, 1996.

Appendix B

Bannister's Formulation

This Appendix provides the mathematical calculations followed by Bannister to calculate the EM field expressions for a horizontal electric dipole, located above lossy ground [B.1]-[B.4].

For an HED source, when h and z are ≥ 0, the Sommerfeld integral expressions for the Hertz vector are

$$\Pi_x = \frac{IL}{4\pi j\omega\epsilon_0}\left[\frac{e^{-\gamma_1 R_0}}{R_0} - \frac{e^{-\gamma_1 R_1}}{R_1} + 2\int_0^\infty \frac{e^{-u_1(z+h)}}{u_1+u_2} J_0(\lambda\rho)\lambda d\lambda\right], \tag{B.1}$$

and,

$$\Pi_z = \left(\frac{IL\cos\phi}{4\pi j\omega\epsilon_0}\right)\frac{\partial}{\partial\rho}\int_0^\infty \frac{2(u_2-u_1)}{\gamma_2^2 u_1 + \gamma_1^2 u_2} e^{-u_1(z+h)} J_0(\lambda\rho)\lambda d\lambda, \tag{B.2}$$

where,

$$R_0 = [\rho^2 + (z-h)^2]^{1/2}, \tag{B.3}$$

$$R_1 = [\rho^2 + (z+h)^2]^{1/2}, \tag{B.4}$$

$$u_1 = (\lambda^2 + \gamma_1^2)^{1/2}, \tag{B.5}$$

$$u_2 = (\lambda^2 + \gamma_2^2)^{1/2}, \tag{B.6}$$

$$\gamma_1 = (-\omega^2\mu_0\epsilon_0)^{1/2}, \tag{B.7}$$

$$\gamma_2 = [j\omega\mu_0(\sigma_2 + j\omega\epsilon_2)]^{1/2}. \tag{B.8}$$

The real part of u_1, u_2, and γ_2 are all positive and a time harmonic dependence of $\exp(j\omega t)$ has been assumed.

From Equations (B.1) and (B.2) and utilizing the identity $(u_2 - u_1)(u_2 + u_1) = \gamma_2^2 - \gamma_1^2$, we have

$$\nabla.\boldsymbol{\Pi} = \left(\frac{IL\cos\phi}{4\pi j\omega\epsilon_0}\right)\frac{\partial}{\partial\rho}\left[\frac{e^{-\gamma_1 R_0}}{R_0} - \frac{e^{-\gamma_1 R_1}}{R_1} + \int_0^\infty \frac{2\gamma_1^2 e^{-u_1(z+h)}}{\gamma_2^2 u_1 + \gamma_1^2 u_2} J_0(\lambda\rho)\lambda d\lambda\right]. \tag{B.9}$$

For $|n|^2 \gg 1$, it has been shown that,

$$\frac{u_2 - u_1}{u_2 + u_1} \approx e^{-u_1 d}, \tag{B.10}$$

and,

$$1 - \left(\frac{u_2 - u_1}{u_2 + u_1}\right) = \frac{2u_1}{u_1 + u_2} \approx 1 - e^{-u_1 d}, \tag{B.11}$$

where,

$$d = {}^{2}/_{\gamma_2}. \tag{B.12}$$

Applying Equations (B.1) and (B.5) and Sommerfeld's integral,

$$S_1 = \int_0^\infty e^{-u_1(z+h)} J_0(\lambda\rho)\frac{\lambda}{u_1} d\lambda = \frac{e^{-\gamma_1 R_1}}{R_1}, \tag{B.13}$$

results in,

$$\Pi_x \approx \frac{IL}{4\pi j\omega\epsilon_0}\left(\frac{e^{-\gamma_1 R_0}}{R_0} - \frac{e^{-\gamma_1 R_2}}{R_2}\right), \tag{B.14}$$

where $R_2 = [\rho^2 + (d + z + h)^2]^{1/2}$. This equation is valid at any range from the source.

Since $\gamma_1^2/\gamma_2^2 = \Delta^2 = 1/n^2$, (B.9) can be rewritten as

$$\nabla.\mathbf{\Pi} \approx \left(\frac{IL\cos\phi}{4\pi j\omega\epsilon_0}\right)\frac{\partial}{\partial\rho}\left(\frac{e^{-\gamma_1 R_0}}{R_0} - \frac{e^{-\gamma_1 R_1}}{R_1} + I_{DIV}\right), \tag{B.15}$$

where,

$$I_{DIV} = \int_0^\infty \frac{2\gamma_1^2 e^{-u_1(z+h)}}{\gamma_2^2 u_1 + \gamma_1^2 u_2} J_0(\lambda\rho)\lambda d\lambda. \tag{B.16}$$

Since

$$\frac{1}{u_1 + \Delta^2 u_2} = \frac{1}{u_1} - \left(\frac{1}{u_1} - \frac{1}{u_1 + \Delta^2 u_2}\right) = \frac{1}{u_1} - \frac{\Delta^2 u_2}{u_1(u_1 + \Delta^2 u_2)}, \tag{B.17}$$

from Equations (B.13) and (B.17) we have,

$$I_{DIV} = 2\Delta^2\left[\frac{e^{-\gamma_1 R_1}}{R_1} - \int_0^\infty \frac{\Delta^2 u_2 e^{-u_1(z+h)}}{u_1(u_1 + \Delta^2 u_2)} J_0(\lambda\rho)\lambda d\lambda\right]. \tag{B.18}$$

Since $|n^2| \gg 1$ ($|\Delta^2| \ll 1$), we can set the function u_1 in the second term of the Equation (B.18) equal to γ_1, the propagation constant in the earth. Therefore,

$$\Delta^2 u_2 \approx \Delta^2\gamma_2 = \gamma_1\Delta, \tag{B.19}$$

and,

$$I_{DIV} \approx 2\Delta^2\left[\frac{e^{-\gamma_1 R_1}}{R_1} - \int_0^\infty \frac{\gamma_1\Delta e^{-u_1(z+h)}}{u_1(u_1 + \gamma_1\Delta)} J_0(\lambda\rho)\lambda d\lambda\right]. \tag{B.20}$$

For $|n^2| \gg 1$, the Fresnel reflection coefficient for vertical polarization is

$$\Gamma_{||} = \frac{\sin\psi_1 - \Delta}{\sin\psi_1 + \Delta}, \tag{B.21}$$

where $\sin\psi_1 = (z + h)/R_1$.

It has been shown that, when $|n^2| \gg 1$ and $|\gamma_0 R_1| \gg 1$,

$$P = \int_0^\infty \frac{\gamma_1 \Delta e^{-u_1(z+h)}}{u_1(u_1+\gamma_1\Delta)} J_0(\lambda\rho)\lambda d\lambda \approx \left(\frac{1-\Gamma_{||}}{2}\right)[1-F(w)]\frac{e^{-\gamma_1 R_1}}{R_1}, \tag{B.22}$$

where $F(w) = 1 - j(\pi w)^{1/2} e^{-w} \mathrm{erfc}\,(jw^{1/2})$, is the Sommerfeld surface-wave attenuation function, and $w = -\frac{\gamma_1 R_1}{2}(\sin\psi_1 + \Delta)^2$, is the Sommerfeld numerical distance [B.5]. Therefore, from Equations (B.20) and (B.22),

$$I_{DIV} \approx \frac{2\Delta^2 e^{-\gamma_1 R_1}}{R_1}\left\{1 - \left(\frac{1-\Gamma_{||}}{2}\right)[1-F(w)]\right\} = \frac{2\Delta^2 A e^{-\gamma_1 R_1}}{R_1}, \tag{B.23}$$

where,

$$A = 1 - \left(\frac{1-\Gamma_{||}}{2}\right)[1-F(w)] = \frac{\sin\psi_1 + \Delta\, F(w)}{\sin\psi_1 + \Delta}. \tag{B.24}$$

Thus, from Equations (B.15) and (B.23),

$$\nabla.\boldsymbol{\Pi} \approx \left(\frac{IL\cos\phi}{4\pi j\omega\epsilon_0}\right)\frac{\partial}{\partial\rho}\left(\frac{e^{-\gamma_1 R_0}}{R_0} - \frac{e^{-\gamma_1 R_1}}{R_1} + \frac{2\Delta^2 A e^{-\gamma_1 R_1}}{R_1}\right). \tag{B.25}$$

When $|n^2| \gg 1$ and $|\Delta \sin\psi_1| \ll 1$,

$$\begin{aligned}\frac{\partial}{\partial\rho}\left(\frac{Ae^{-\gamma_1 R_1}}{R_1}\right) &= -A(1+\gamma_1 R_1)\cos\psi_1 \frac{e^{-\gamma_1 R_1}}{R_1^2} + \left(\frac{e^{-\gamma_1 R_1}}{R_1}\right)\frac{\partial A}{\partial\rho} \\ &\approx -A(1+\gamma_1 R_1)\cos\psi_1 \frac{e^{-\gamma_1 R_1}}{R_1^2} \\ &\approx -(1+\gamma_1 R_1 A)\cos\psi_1 \frac{e^{-\gamma_1 R_1}}{R_1^2}.\end{aligned} \tag{B.26}$$

where $\cos\psi_1 = \rho/R_1$. Therefore, from Equations (B.25) and (B.26),

$$\begin{aligned}\nabla.\boldsymbol{\Pi} \approx -\frac{IL\cos\phi}{4\pi j\omega\epsilon_0}\Bigg[&(1+\gamma_1 R_0)\cos\psi_0 \frac{e^{-\gamma_1 R_0}}{R_0^2} - (1+\gamma_1 R_1)\cos\psi_1 \frac{e^{-\gamma_1 R_1}}{R_1^2} \\ &+ \frac{2\cos\psi_1\, e^{-\gamma_1 R_1}}{n^2 R_1^2}(1+\gamma_1 R_1 A)\Bigg],\end{aligned} \tag{B.27}$$

From Equation (B.17), utilizing the identity $(u_2 - u_1)(u_2 + u_1) = \gamma_2^2 - \gamma_1^2$, we have

$$\frac{u_2 - u_1}{\gamma_2^2 u_1 + \gamma_1^2 u_2} = \frac{1}{u_1(u_1 + u_2)} - \frac{\Delta^2}{u_1(u_1 + \Delta^2 u_2)}. \tag{B.28}$$

Therefore, (B.2) reduces to

$$\begin{aligned} \Pi_z &= \left(\frac{IL\cos\phi}{4\pi j\omega\epsilon_0}\right)\frac{\partial}{\partial\rho}\left[\int_0^\infty \frac{2e^{-u_1(z+h)}}{u_1(u_1+u_2)} J_0(\lambda\rho)\lambda d\lambda \right. \\ &\qquad \left. - 2\Delta^2 \int_0^\infty \frac{e^{-u_1(z+h)}}{u_1(u_1+\Delta^2 u_2)} J_0(\lambda\rho)\lambda d\lambda\right] \\ &= \left(\frac{Il\cos\phi}{4\pi j\omega\epsilon_0}\right)\frac{\partial}{\partial\rho}(I_{21} - I_{22}), \end{aligned} \tag{B.29}$$

where,

$$I_{21} = \int_0^\infty \left(\frac{2u_1}{u_1+u_2}\right) e^{-u_1(z+h)} J_0(\lambda\rho)\frac{\lambda}{u_1^2} d\lambda, \tag{B.30}$$

and,

$$\begin{aligned} I_{22} &= 2\Delta^2 \int_0^\infty \frac{e^{-u_1(z+h)}}{u_1(u_1+\Delta^2 u_2)} J_0(\lambda\rho)\lambda d\lambda \\ &\approx 2\Delta^2 \int_0^\infty \frac{e^{-u_1(z+h)}}{u_1(u_1+\gamma_1\Delta)} J_0(\lambda\rho)\lambda d\lambda = \frac{2P}{\gamma_2} = dP. \end{aligned} \tag{B.31}$$

After some manipulations, we have

$$\frac{\partial I_{21}}{\partial\rho} \approx \frac{\cos\psi_2\, e^{-\gamma_1 R_2}}{R_2 + d + z + h} - \frac{(1+\gamma_1 d)\cos\psi_1\, e^{-\gamma_1 R_1}}{R_1 + z + h}, \tag{B.32}$$

and,

$$\frac{\partial I_{21}}{\partial\rho} \approx \frac{\cos\psi_2\, e^{-\gamma_1 R_2}}{R_2 + d + z + h} - \frac{(1+\gamma_1 d)\cos\psi_1\, e^{-\gamma_1 R_1}}{R_1 + z + h}, \tag{B.33}$$

where $\sin\psi_2 = (d+z+h)/R_2$ and $\cos\psi_2 = \rho/R_2$.

Therefore, from Equations (B.24), (B.29), (B.32), and (B.33),

$$\Pi_z \approx -\frac{IL\cos\phi}{4\pi j\omega\epsilon_0\rho}\left[\sin\psi_2\, e^{-\gamma_1 R_2} - \sin\psi_1\, e^{-\gamma_1 R_1} + \gamma_1 d e^{-\gamma_1 R_1}(\sin^2\psi_1 + A\cos^2\psi_1)\right]. \tag{B.34}$$

After deriving the expressions for the HED Hertz vector, the electric and magnetic fields at any point in the air can be obtained from $\mathbf{E} = -\gamma_1^2\mathbf{\Pi} + \nabla(\nabla.\mathbf{\Pi})$ and $\mathbf{H} = j\omega\epsilon_0(\nabla\times\mathbf{\Pi})$. The components of electric and magnetic fields in the cylindrical coordinate system are given in the following equations:

$$\begin{aligned} E_\rho = \frac{IL\cos\phi}{4\pi j\omega\epsilon_0}\Bigg[&\{(3\cos^2\psi_0 - 1)(1+\gamma_0 R_0) - \gamma_1^2 R_0^2\sin^2\psi_0\}\frac{e^{-\gamma_1 R_0}}{R_0^3} \\ &- \{(3\cos^2\psi_1 - 1)(1+\gamma_1 R_1) - \Gamma_{||}\gamma_1^2 R_1^2\sin^2\psi_1\}\frac{e^{-\gamma_1 R_1}}{R_1^3} \\ &+ \frac{2e^{-\gamma_1 R_1}}{n^2 R_1^3}\Bigg\{[(3\cos^2\psi_1 - 1)(1+\gamma_1 R_1)] \\ &- \frac{2R_1^2}{d^2}\left[1 - \frac{R_1}{R_2}e^{-\gamma_1(R_2-R_1)}\right] \\ &+ n^2\gamma_1^2 R_1^2\left[\sin\psi_1 + \left(\frac{1-\Gamma_{||}}{2}\right)F(w)\Delta\right]\Bigg\}\Bigg], \end{aligned} \tag{B.35}$$

$$\begin{aligned} E_\phi = \frac{IL\sin\phi}{4\pi j\omega\epsilon_0}\Bigg[&(1+\gamma_1 R_0+\gamma_1^2 R_0^2)\frac{e^{-\gamma_1 R_0}}{R_0^3} - (1+\gamma_1 R_1+\gamma_1^2 R_1^2)\frac{e^{-\gamma_1 R_1}}{R_1^3} \\ &+ \frac{2e^{-\gamma_1 R_1}}{n^2 R_1^3}\left\{(1+\gamma_1 R_1 A) + \frac{2R_1^2}{d^2}\left[1 - \frac{R_1}{R_2}e^{-\gamma_1(R_2-R_1)}\right]\right\}\Bigg], \end{aligned} \tag{B.36}$$

$$E_z = \frac{IL\cos\phi}{4\pi j\omega\epsilon_0}\Big\{(3+3\gamma_1R_0+\gamma_1^2R_0^2)\sin\psi_0\cos\psi_0\frac{e^{-\gamma_1R_0}}{R_0^3}$$

$$-\left(3+3\gamma_1R_1+\Gamma_{||}\gamma_1^2R_1^2\right)\sin\psi_1\cos\psi_1\frac{e^{-\gamma_1R_1}}{R_1^3}$$

$$+\frac{2}{n^2}(3+3\gamma_1R_1+\gamma_1^2R_1^2)\sin\psi_1\cos\psi_1\frac{e^{-\gamma_1R_1}}{R_1^3} \qquad \text{(B.37)}$$

$$-\gamma_1^2\left[\frac{\cos\psi_2\,e^{-\gamma_1R_2}}{R_2+d+z+h}-\frac{\cos\psi_1\,e^{-\gamma_1R_1}}{R_1+z+h}(1+\gamma_1d)\right]$$

$$-2\Delta\left[1-\left(\frac{1-\Gamma_{||}}{2}\right)F(w)\right]\cos\psi_1\,(\gamma_1R_1)^2\frac{e^{-\gamma_1R_1}}{R_1^3}\Big\},$$

$$H_\rho = \frac{IL\sin\phi}{4\pi}\left[(1+\gamma_1R_2)\sin\psi_2\frac{e^{-\gamma_1R_2}}{R_2^2}-(1+\gamma_1R_0)\sin\psi_0\frac{e^{-\gamma_1R_0}}{R_0^2}\right. \qquad \text{(B.38)}$$

$$\left.-\frac{e^{-\gamma_1R_2}}{R_2(R_2+d+z+h)}+\frac{(1+\gamma_1dA)e^{-\gamma_1R_1}}{R_1(R_1+z+h)}\right],$$

$$H_\phi = -\frac{IL\cos\phi}{4\pi}\left[(1+\gamma_1R_0)\sin\psi_0\frac{e^{-\gamma_1R_0}}{R_0^2}\right.$$

$$-\left(1+\Gamma_{||}\,\gamma_1R_1\right)\sin\psi_1\frac{e^{-\gamma_1R_1}}{R_1^2}+\frac{\gamma_1^2d}{R_1}\left(\frac{1-\Gamma_{||}}{2}\right)F(w)e^{-\gamma_1R_1} \qquad \text{(B.39)}$$

$$\left.-\frac{e^{-\gamma_1R_2}}{R_2(R_2+d+z+h)}+\frac{(1+\gamma_1\,d)e^{-\gamma_1R_1}}{R_1(R_1+z+h)}\right],$$

$$H_z = \frac{IL\sin\phi}{4\pi}\left[(1+\gamma_1R_0)\cos\psi_0\frac{e^{-\gamma_1R_0}}{R_0^2}-(1+\gamma_1R_2)\cos\psi_2\frac{e^{-\gamma_1R_2}}{R_2^2}\right], \qquad \text{(B.40)}$$

where $\sin\psi_0 = (z-h)/R_0$ and $\cos\psi_0 = \rho/R_0$.

The obtained set of formulas can be used to determine the effect of the ground constants on the field intensity in the vicinity of a dipole. These formulas may also be used to show the influence of the location of the dipole on the attenuation of EM waves at different frequencies. These equations are valid for infinitesimal dipoles; however, they

are also true for finite dipoles if the length l is much less than both the free-space wavelength and the measurement distance.

References

[B.1] P. R. Bannister, "New Formulas for HED (Horizontal Electric Dipole), HMD (Horizontal Magnetic Dipole), VED (Vertical Electric Dipole), VMD (Vertical Magnetic Dipole) Subsurface to Subsurface Propagation", *NUSC Technical Report 6881*, Naval Underwater Systems Center, New London, CT, January 1984.

[B.2] P. R. Bannister, " Image-Theory Electromagnetic Fields of Horizontal Dipole Antennas in Presence of Conducting Half-Space", *NUSC Technical Report 6511*, Naval Underwater Systems Center, New London, CT, September 1981.

[B.3] P. R. Bannister, "Extension of Finitely Conducting Earth-Image Theory Results to Any Range", *NUSC Technical Report 6885*, Naval Underwater Systems Center, New London, CT, January 1984.

[B.4] P. R. Bannister, "Applications of Complex Image Theory", *Radio Science*, vol. 21, no. 4, pp. 605-616, August 1986.

[B.5] A. C. Wiedeman, "Computation of the Complex Error Function", *SIAM Journal on Numerical Analysis*, vol. 31, no. 5, pp. 1497-1518, October 1994.

Appendix C

Geometry of Transmission Line's Sag

C.1 Introduction

Traditional electromagnetic field computation techniques assume that the current carrying power transmission lines are straight horizontal wires. This assumption results in a model whose fields are distorted from those produced in reality [C.1].

Precise analytical modeling of electric and magnetic fields produced by overhead power lines is important in several research areas such as health effects of extremely low frequency (ELF) electromagnetic fields and design of power line proximity detectors and measurement equipment [C.1] and [C.2].

Whenever analysis of the power line is concentrated in close proximity to the conductors, the straight wire approximation must be critically reviewed. The effect of the catenary on the amplitude of the electric and magnetic fields may be significant in some cases [C.1] and [C.2].

In this appendix, an algorithm is proposed for modeling the electric and magnetic fields produced by the sagged power transmission lines.

C.2 Representation of the Conductor Sag

The exact shape of a conductor suspended between two poles of equal height can be described by parameters such as the distance between the points of suspension, L, the sag of the conductor, s, the height of the lowest point, h (normally in the mid-span), and the highest points above the ground, H, as shown in Figure C.1 [C.1].

A catenary symmetric with respect to the z-axis in the xz-plane is specified by the following equation

$$z = \frac{1}{a}\cosh(ax). \tag{C.1}$$

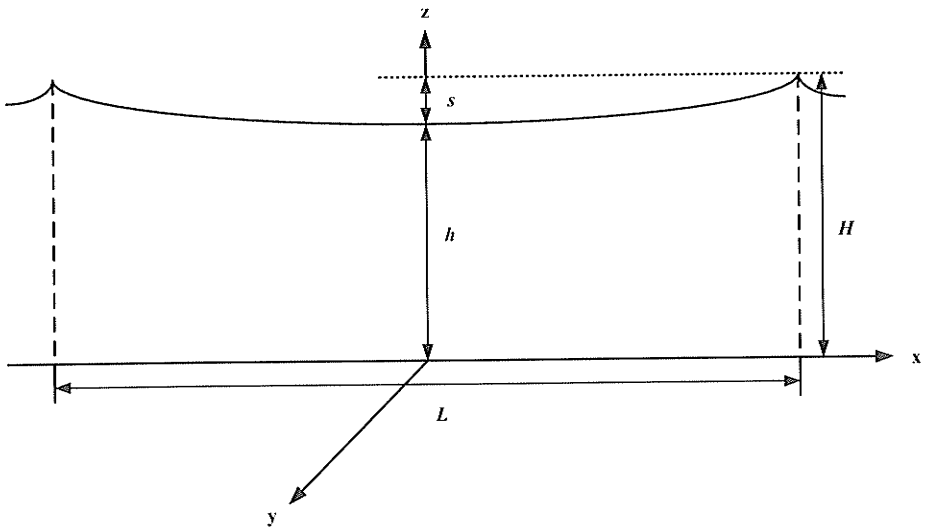

Figure C. 1. Geometry of a sagged transmission line.

The parameter a is given by

$$a = \frac{1}{h + z_d}, \tag{C.2}$$

and z_d is the distance between the catenary coordinate system origin and the ground level which can be found from [C.1],

$$\frac{H + z_d}{h + z_d} - \cosh\left(\frac{L}{2(h + z_d)}\right) = 0. \tag{C.3}$$

Although a precise representation of the catenary shape is given by (C.3), it may be not the most effective expression for practical applications. In order to reduce the computation time, alternative formulas approximating the true catenary are recommended [C.1]. Most often, several first terms of the series expansion of (C.1)

$$z = \frac{1}{a} + \frac{ax^2}{2!} + \frac{a^3x^4}{4!} + \cdots - z_d \tag{C.4}$$

are used. The first two terms of (C.4) represent a parabola. In this case, however, the points of suspension of the true catenary and those of the parabola will not coincide, although the difference is minor. Another approximate representation of the catenary is used in [C.2],

$$z = s\left(\frac{2x}{L}\right)^2 + h. \tag{C.5}$$

For the representation given by (C.5), the origin of the coordinate system is located at ground level. When the relative sag (s/L) of the power line conductor is small, the correlation between the parabola approximation and the catenary equation is very high and the error is well within practical level of precision [C.1].

C.3 Segmentation of the Line

In order to take the effect of sag into account, we decompose each segment of the transmission line into horizontal and vertical vectors. This will provide a more accurate approximation for the transient fields radiated from a transmission line. The schematic of the decomposed segment of wire is shown in Figure C.2. The fields due to each component can be calculated using the set of formulas given in Chapter 3.

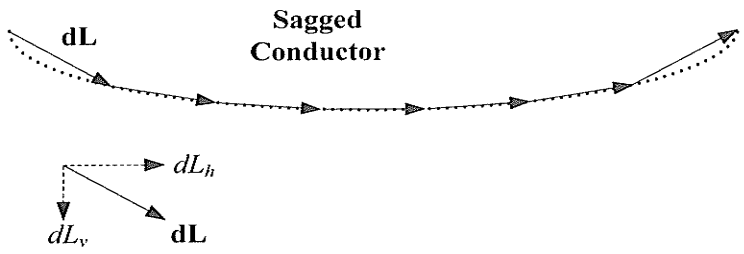

Figure C. 2. Configuration of an arbitrarily-oriented segment of a sagged conductor, decomposed into horizontal and vertical segments.

References

[C.1] A. V. Mamishev, R. D. Nevels, and B. D. Russel, "Effects of Conductor Sag on Spatial Distribution of Power Line Magnetic Field", *IEEE Transaction on Power Delivery*, vol. 11, no. 3, pp. 1571-1576, July 1996.

[C.2] R. Amiri, H. Hadi, and M. Marich, "The Influence of Sag in the Electric Field Calculation around High Voltage Overhead Transmission Lines", *Annual Report–Conference on Electrical Insulation and Dielectric Phenomena*, pp. 206-209, Kansas City, USA, October 2006.